Ring Laser Gain Media

A thesis submitted in partial fulfilment
of the requirements for the degree of
Master of Science

Richard Graham
2006

Department of Physics and Astronomy, University of Canterbury, Private Bag 4800, Christchurch, New Zealand

Abstract

This thesis details the design and construction of an experiment to measure the radial distribution of laser gain in a cylindrical Helium-Neon laser gain tube. This distribution is important as it can effect the transverse mode structure of a running ring laser. Earlier theoretical models of the distribution were not supported by high quality experimental data and fail to take into account some physical processes.

A resolution of 8 parts per million in gain and 50 μm in radial position has been achieved. Gain distributions have been measured and are shown to be well modeled by a 0^{th} order Bessel function with first roots at the tube walls and a central dip depending on excitation power; except for the region very near to the tube walls where a very rapid increase in gain has been observed. Hydrogen has been identified by spectroscopic analysis as the primary constituent of gas contamination and cause of the long term reduction in gain of large ring lasers.

Additional work has been done to detect a proposed non-classical Lense-Thirring field around a spinning lead superconductor. It was found that any effect is at least 20 times smaller than predicted.

Techniques and tools for data acquisition programming have been reviewed focusing on difficulties with coupling of user interface and application logic, monolithicity, difficulties with scripting and algorithm implementation.

Contents

Chapter 1

Introduction

1.1 Motivation

Since the beginning of the University of Canterbury ring laser project (1988), the helium-neon laser system has been used exclusively for the construction of five large ring laser gyroscopes. helium-neon was chosen mostly because of the maturity of this technology and ready availability of optical components designed to operate at the 633nm wavelength[1].

As the ring lasers have become successively larger, it has become necessary to move further away from the known territory of traditional helium-neon lasers. The laser gain tubes used in the current generation of ring laser gyroscopes are much larger[2] than those used in commercial helium-neon lasers, gas pressures are much higher[3], gas mix ratios differ and the pump mechanism is a VHF electric field, as opposed to the more traditional direct current excitation.

Throughout the history of the ring laser project, investigation into the more fundamental processes of laser gain in a helium-neon plasma have often been neglected. For example, we have no rigorous way of determining the optimal combination of gas mix, pressure, tube diameter and excitation power.

Following the construction of the very large ring laser UG2, it has become apparent that more gain is needed while the gain tube must remain relatively large due to the large beam waist that results from such a long cavity. We would like to ensure that the laser runs in TEM_{00} mode, and for this we need to ensure that the distribution of laser gain across the central portion of the tube diameter is smooth.

[1] While the broad composite gain curve of Ne^{20} and Ne^{22} also makes the helium-neon system a good candidate due to easy multidirectional operation, it is certainly not the only laser system with this property.

[2] This is to accommodate the much larger spot sizes that result from a much larger than typical laser cavity.

[3] Helium-neon lasers typically use a pressure of 'a few Torr' and 10:1 He:Ne ratio in a discharge tube of at most a few millimetres diameter [32].

Due to the large size of UG2, re-filling it with gas is a significant inconvenience. Choosing operating parameters such that a usable gain distribution prevails for as long as possible even as the gas becomes contaminated would be of significant practical usefulness.

While a theoretical model of the distribution of excited states in a helium-neon laser gain tube has previously been constructed by McLeod, the model fails to explain the distribution at low pump powers and fails to take into account many physical processes. This model has thus far been of little practical use in terms of optimising the running parameters of the large ring lasers. Without good, high resolution experimental data it is unlikely that significant theoretical progress could be made in terms of improving the model.

The **main aim** of this project is the development of an apparatus for automated, direct measurement of the single pass laser gain of a helium-neon plasma as a function of position (relative to the gain tube), gas pressure, gas composition and RF pump power. The gain must be measured to a resolution suitable for fitting to theoretical models. Based on earlier work [12] we expect this resolution to be better than than 100 ppm and preferably around 20 ppm.

1.2 Thesis Outline

With the distinction of being the first operational gas laser system, the basics of helium-neon operation are very well known and are detailed in countless textbooks. It is interesting however that this distinction also means that a concise overview of the helium-neon system, particularly including design decisions made during the early days of commercialisation of the laser are surprisingly difficult to obtain. Chapter 2 of this thesis begins with a concise overview of the helium neon laser and laser gain process. It goes into particular detail regarding the main topic of this thesis — radial gain distribution and its effect on transverse mode structure. Chapter 2 also includes a review of the model of radial gain distribution proposed by former PhD student Duncan McLeod.

Chapter 3 is the largest chapter and details all experimental work done in order to develop an apparatus capable of measuring radial gain distribution. The main problem which plagued the experimental work was unacceptably low signal to noise ratio, and this chapter goes in to some depth to rigoursly calculate the expected error from each piece of hardware and design consideration. The chapter concludes by summarising experimental observations of signal to noise for various parts of the system and theoretical predictions. Chapter 3 also details methodology used in secondary experiments such as measuring gas contamination and characterising absolute plasma power.

Chapter 4 includes all results from experiments to measure radial gain distribution and an analysis of these results with respect to existing models. It details the computational framework that was set up to accommodate development of a new model using the gathered experimental data, and also proposes other uses for the gathered data. This chapter also includes results of an analysis of a sample of old contaminated gas from the UG2 ring laser and a brief discussion

of gas contamination.

Chapters 5 and 6 are both secondary to the main topic and aims of the thesis as they detail additional research undertaken as an aside to the main topic. The reader interested only is ring laser physics may wish to skip these chapters.

Chapter 5 details an interesting experiment which was undertaken to validate a reported result in which another group detected an anomalous acceleration field in the region surrounding spinning lead and niobium superconductive disks. The extraordinary resolution of a large ring laser has potential to vastly improve the sensitivity of reported results.

During the completion of this thesis, considerable expertise was gained in the field of data acquisition technology and programming. Chapter 6 begins by identifying some of the shortcomings of the traditional approach to data acquisition programming which has been used throughout the ring laser project to date. An approach which encapsulates modern software engineering techniques, in particular object orientated programming is detailed as well as options for scripting and algorithm development which are presented with a focus on the LuaView toolkit. The majority of the material in the chapter is presented as a case study of a data acquisition system that was developed for an experiment in super frame dragging which was completed as an aside the the main topic of the thesis.

Chapter 7 summarises the entire thesis by illustrating progress made and key results. It also provides some direction for future work.

This thesis assumes a basic knowledge of laser physics. Throughout this thesis the LabView G, Lua, Python and Matlab languages are used. With the exception of LabView G, the syntax of all these languages is generally clear enough that the source code should be quite readable to those with a basic programming knowledge and without a specific knowledge of the language in question. In chapter 6 some use is made of the UML class diagram notation.

Chapter 2

Theory and Background

2.1 The ring laser

When used in this thesis, the term 'ring laser' refers to a self contained, active laser interferometer utilising the Sagnac effect to provide a measurement of inertial rotation.

Frenchman Georges Sagnac was the first to realise the potential of a circular interferometer to measure rotation. The original motivation was to detect relative motion of the ether. The original derivation of the Sagnac equation (equation 2.1) was ether-theoretic, though modern general relativistic derivations produce the same result. In a 1913 experiment, Sagnac became the first to (knowingly) make a measurement of rotation with a turntable mounted interferometer through what is now known as the Sagnac effect. [36]

The Sagnac effect arises when a beam of light is split, one half travelling clockwise around a circular or polygonal path, the other anticlockwise. If the interferometer is rotated a small angle while the beam is travelling then a relative phase shift will result between the two beams. By recombining the beams this phase shift can be measured.

In the case of a rotating active laser interferometer it is clear that we require a integer number of wavelengths around the cavity and consequently there must be a difference in optical frequency of each beam proportional to the rotation rate. This difference in frequency is easily measured by measuring the beat frequency of the combined beams. Typically this frequency is in the audio range.

The equation for the change in optical frequency δf of an interferometer with path length P and an area in the plane of rotation of $\mathbf{A}$ takes the following form:

$$\boxed{\delta f = \frac{4\mathbf{A}\omega}{\lambda P}} \tag{2.1}$$

Here ω is the rate of rotation in inertial space and λ is the wavelength of the source.

The interests of this group are in building very large ring lasers for research in various aspects of fundamental physics, geophysics and geodosy. Table 2.1 shows specifications of the current generation of ring lasers.

Laser	Perimeter P (m)	Single Pass Gain (ppm)
C2	4	222.4
G	16	48.5
UG-1	70	194.6
UG-2	121.4	1012.4
PR-1	6.4	210

Table 2.1: Ring laser gain statistics.

2.2 The helium-neon laser system

Figure 2.1 shows the basic atomic transitions which give rise to the 632.8nm emission. The pumping mechanism, (in our case, free electrons accelerated by the RF electric field) bring Helium atoms to a long lived metastable energy level of 20.6eV. The lifetime of this state is 2.04 ms, [19, 21] which for our purposes is essentially forever. By good fortune there is a close coincidence in energy levels between the He(2^1S) level and those of Ne(5s') and Ne(5s).

With the addition of around 0.085 eV of thermal energy (corresponds to an effective temperature of around 980 K[1]) we note that there is now a high probability that a collision between a ground state Neon atom will result in energy transfer leaving the Neon atom in either one of the 4s or 5s doublet states. In our case we are interested primarily in the 5s' state since it is the 5s' to 3p transition which provides laser action at the familiar 632.8 nm wavelength as the 5s' state is sufficiently long lived ($\approx$ 55 ns) to allow a population inversion to be established.

After stimulated emission occurs we note that the Neon remains in an excited 3p state. Transitions from the 3p level directly to the ground state (lifetime $\approx$ 19 ns) are effectively forbidden as the many transitions from the 3p state to lower energy excited states are each much more probable (lifetimes of 7—10 ns [17]). In practice collisions with the walls (which can be calculated to happen after time of the order of $\approx$ 10—100 ns depending on discharge conditions) are mostly responsible for the final transition to the ground state. It is for this reason that a typical helium-neon laser uses as narrow a tube diameter as possible with as high a pressure as possible when also considering that as pressure increases the population inversion is decreased as a result of excitation of the lower laser level by electron collisions with atoms in the 1s state [44]. It is this mechanism which fundamentally limits the maximum power of any realistic helium-neon

[1]Note that the mean gas temperature need not be this high due to the Maxwellian velocity distribution as only a small fraction of the atoms are involved in laser action.

laser. The most powerfull helium-neon laser ever made [22] (total output of 350 mW) used two flattened gain tubes to maximise wall area, at the expense of beam profile.

It has been found empirically [32] that the optimum *pd* (pressure-diameter) product is a few Torr-mm, and that the gain per unit length varies inversely with tube diameter. It is often assumed that to a first approximation the electron temperature in a cylindrical discharge tube (such that the electrons have a Maxwellian distribution) is a function of only the *pd* product and is independent of discharge power. Wright [44] and Gordon *et al.* [8] have quoted empirical results for the optimal *pd* product of 14.6 Torr mm and 6.6 Torr mm, the former using a RF discharge and the latter using a DC discharge.

Herziger, Holzapfel and Seelig [18] expand on the concept of *pd* product. Based on experimental measurements they give an expression for the maximum gain G_0 as a function of discharge tube length l and diameter D. This is given in equation 2.2 where l_0=1 m and D_0=1 mm. They note that the optimum value of total pressure and current increases with smaller tube diameters. Equation 2.2 is valid for optimal[2] values of total pressure.

$$G_0(l, D) \cong \left[1 + \frac{1}{2}\left(\frac{D_0}{D}\right)^{1.4}\right]^{l/l_0} \tag{2.2}$$

Typical helium-neon lasers use a He:Ne ratio of between 5:1 and 9:1. In ring lasers we use ratios of up to 15:1. Andrews and King [3] quote an optimal gas mix ratio of 9:1. Figure 2.2 shows the results of a theoretical treatment based on ambipolar diffusion by Young, Willett and Maupin [45] in which the electron temperature is plotted for various *pd* values as a function of helium-neon mix ratio.

Note that the vertical axis in figure 2.2 shows very high electron temperatures.

The electron temperature in a helium-neon plasma is much higher than the gas temperature, which is typically around 500 K [33]. The axial electric field results in high temperature electrons in the central part of the discharge which continually generate new charge carriers by impact ionisation. Because of their high temperature and thus mobility the electrons build up on the tube walls much more easily than ions. This results in the tube walls building up a negative charge which mostly reflects further incoming electrons from the central region. This process keeps the electron and ion currents from the central region to the tube wall equal, thus allowing for overall electrical neutrality of the system — a fundamental property of all plasmas.

From Maxwell-Boltzmann statistics it can be shown that the electron density decreases exponentially from the walls; this results in the buildup of a positive space charge of ions very near to the walls. The extension of this positive sheath of space charge has been studied by Schuöcker [30] for narrow diameter gain

[2]The word optimal here is relating to optimal laser power output, not necessarily the same conditions that would be considered optimal for a gyroscopic ring laser.

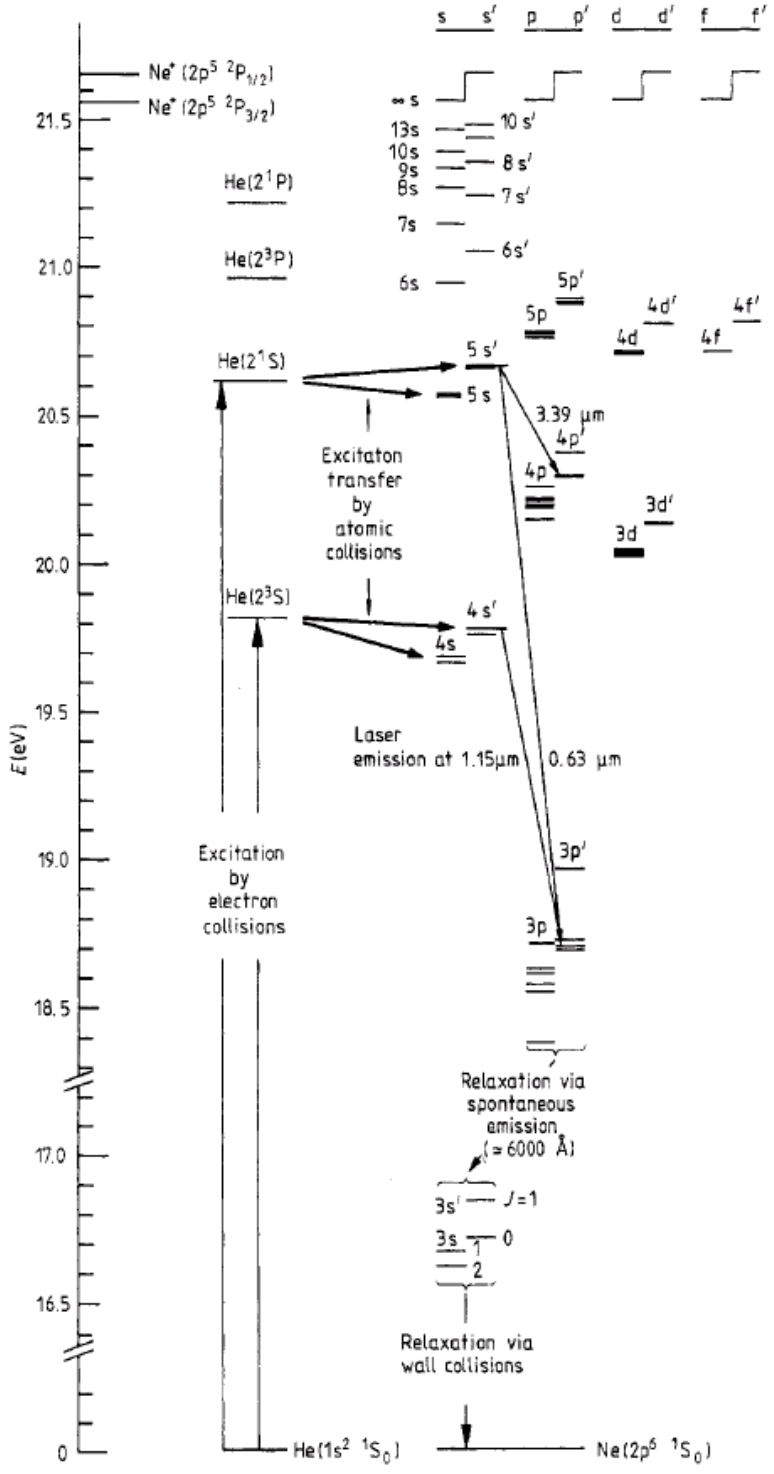

Figure 2.1: Helium-neon energy level transitions responsible for 632.8nm output [15]

tubes in waveguide lasers where the extension of the sheath is comparable to the tube diameter. In the case of larger diameter tubes, the sheath is considered negligible.

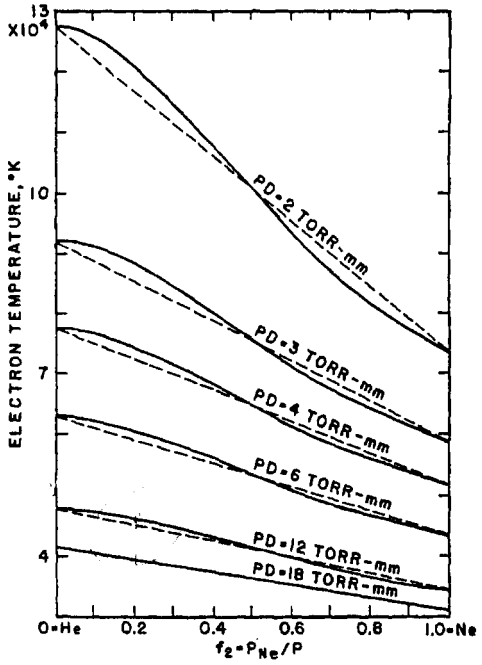

Figure 2.2: Electron temperature as a function of the ratio of He:Ne for various *pd* values as calculated theoretically by Young *et al.* [45]

2.3 Radial gain profile

2.3.1 Observations

Figures 2.3, 2.5 and 2.4 show experimentally measured radial gain distributions for a variety of discharge power levels in helium-neon discharges.

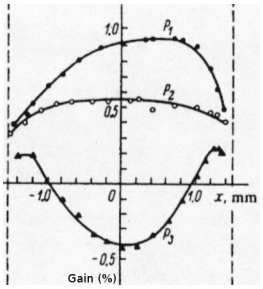

Figure 2.3: Radial distribution as reported by Tsarkov *et al.* for various arbitrary pumping powers. RF excitation was used here. [42]

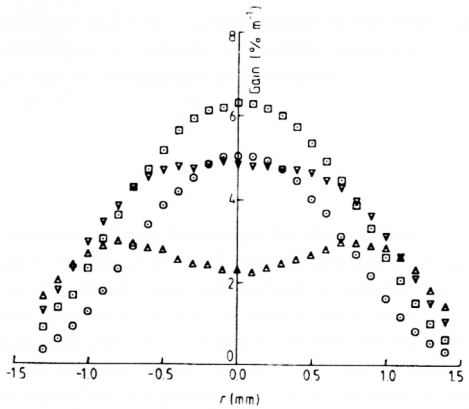

Figure 2.4: Radial distribution of gain with 0.2 Torr Ne and 4.8 Torr ^{3}He. Current 2.5mA (O), 6.0mA (□), 12mA (▽), 20mA (△). (Spoor and Latimer). DC discharge [35].

The basic shape of all the plots is modeled by a 0^{th} order Bessel function, normalised such that the first roots appear at the tube walls. This is a standard result in gas discharges and can be obtained reasonably straightforwardly by considering ambipolar diffusion of electrons in accordance with Fick's law.

One exception to this occurs in the case of the AC discharge measured by Tsarkov *et al.* as the gain in this case appears not to decrease to zero near the tube walls but remains finite within the measured radial resolution[3]. While this could also be argued to be the case for the results of Spoor *et al.* they mention

[3]We should also note that based on the asymmetry of the reported curves (reported to be caused by 'technical errors in the experiment') which is of similar order to the offset from zero we can not discount the possibility that the non-zero gain at the walls is not a real effect.

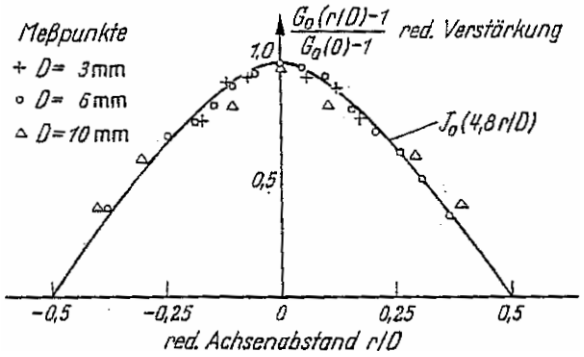

Figure 2.5: Normalised radial gain distribution as measured by Herziger [18] for various tube diameters. DC discharge.

that they think this is a consequence of either the finite spatial resolution of the measurement technique or that it indicates a non-zero population of the helium 2^1S metastable state at the walls due to incomplete de-excitation of these states on collision with the walls.

Another deviation from this profile arises near the centre of the tube at high pump powers. As the pumping rate is increased from zero, the population inversion between the laser levels at any particular point increases, goes through a maximum and then begins to decrease — in some cases the transition becomes absorptive. As the pump power is increased from zero power the gain distribution is first well modeled by a Bessel function then above some threshold pump power a local minima appears at the centre of the distribution (middle of the gain tube). It has also been noted that the value of this threshold power decreases as the helium partial pressure is increased [25].

2.3.2 Effect on transverse mode structure

The distribution of light in a laser beam is given by transverse electromagnetic modes. These are defined by Hermite-Gaussian functions. The lowest order mode, TEM_{00} is represented by a pure Gaussian. Evidence from running ring lasers suggests that high order transverse modes (which arise at high laser power) are responsible for large shifts in Sagnac frequency through an as-yet unknown mechanism. For practical reasons it is highly desirable to ensure that ring lasers run in the TEM_{00} mode.

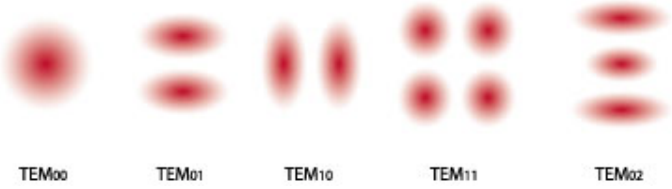

Figure 2.6: Laser light patterns for various low order TEM modes

Together the Hermite-Gaussian functions form a complete basis set for representation of the light distribution in any laser beam; i.e. any pattern of light can be represented as a sum of TEM modes. This is anagalous to how sinusoids form a complete basis set for describing any waveform in Fourier analysis.

Calculation of the dominant transverse mode or combination of modes can be done by computer iteration using the procedure of Fox and Lee [5] or one of many more sophisticated techniques such as that of Atlmann *et al.* [1]. Such procedures generally rely on repeated integration of the propagation equation and methods of determining gain or loss, such as Huygens' integration kernels for plane mirror resonators. Without recourse into a detailed description of these methods we can say in general that in a CW laser given sufficient time to stabilise, the dominant mode will be the one for which the net gain is the highest.

It is possible that two modes will have very similar net gain and oscillation will result, however we assume here that in a real laser there will always be some small non-symmetry which will cause a steady state solution to eventually emerge. Occasionally we observe two transverse modes running simultaneously, however when this happens it is always taken as indicating unsatisfactory operation and the situation is avoided usually by reducing the RF excitation.

Determining the mode which will run in the steady state solution is now simply a matter of analysing the radial distribution of light for each mode and checking how well it matches up to the radial distribution of laser gain. This is done in the same way that we determine the residuals in least-squares fitting — simply integrating the difference between the functions. We then simply find the mode with the largest integral α.

$$\alpha = w \int \int |U_{mn}(x,y) - G(x,y)| dxdy \tag{2.3}$$

At a first guess it is natural to think that the best case would thus be to have a gain tube of similar size to the laser spot, since the best case for the gain distribution (a Bessel function normalised to have the first roots at the tube wall) and the best case for the laser light distribution (a pure Gaussian) are both centrally peaked functions that decay to zero at the tube walls. We have to be carefull with such an analysis though; figure 2.7 shows the best fit of a Gaussian function ($2.13e^{-x^2/1.60^2}$) to a normalised Bessel function. It is unrealistic because the intensity remains finite outside the tube where there is an (absorbing) glass wall.

If we simply say that no beam can exist outside the tube (i.e. by setting the residuals outside the tube to infinity when fitting) then the Gaussian will never converge. A simple solution is to raise the residuals outside the tube to a high-order power. This way the fit will converge while near zero intensity at the tube walls will be retained. The power 4 was used for illustration to make the more realistic 'best case' plot shown in figure 2.8. The resulting best-fitting function was multiplied appropriately so that it is bounded by the Bessel function. The function being optimised is represented by equation 2.4 where $B(x)$ is a Bessel function, $G(x)$ a Gaussian.

$$f(x) = \begin{cases} B(x) - G(x) & \textbf{if } x > -1 \textbf{ and } x < 1 \\ (B(x) - G(x))^n & \textbf{if } x \geq 1 \textbf{ or } x \leq -1 \end{cases} \tag{2.4}$$

We can gain some insight into the difficulty of running in TEM_{00} mode by applying the same analysis to higher order modes. Full equations of the light distribution for given transverse modes are available in Siegman [32]. These are quite lengthy if written in full and deal with variables we are not interested in such as propagation distance, waist size and wavelength. For the purposes of this analysis we are only interested in the general shape of the curve. Figure 2.9 was made assuming a TEM_{10} mode observed along the horizontal axis, computed by simply multiplying the previous Gaussian expression by the first order Hermite polynomial which has the form $H_1(x) = 2x$.

The mean error indicated on each plot is simply the average distance between the lines over the diameter of the tube. We can see that in the best case, the difference in error between the TEM_{00} and TEM_{10} modes is around 40%. In a more realistic situation the beam will be much narrower than the tube and the problem accentuated.

Figure 2.10 shows the same beam profile as in figure 2.9 but fitted to equation 2.5, essentially a simplified version of equation 2.6 used by McLeod [25] (section 4.5). A value of 0.40 was used for the degree of saturation k. Note the decrease in error for a TEM_{10} mode when compared to figure 2.9.

$$N_{inv} = \cos\left(\frac{\pi x}{2}\right) - k\cos\left(\frac{3\pi x}{2}\right) \tag{2.5}$$

Effect of transverse mode frequencies

In the previous analysis we have assumed that the gain of each transverse mode can be entirely determined by matching the pattern of laser gain and the pattern of light which forms the transverse mode. This is not entirely true as each transverse mode has a slightly different optical frequency and the gain varies with optical frequency. This means that it is possible to have different transverse modes having different optical frequency but the same longitudinal mode number.

The difference in optical frequency is typically of the same order as the FSR[4]. The mechanism by which different transverse modes have different optical frequencies was discovered experimentally by Gouy in 1890 [9,10]. He found that any beam with a simple profile will be phase shifted by half a cycle as it passes through a focal point.

A total Gouy phase shift ϕ summed around the optical path causes an optical frequency shift of $\frac{\phi}{2\pi}\times$FSR, so the k$^{\text{th}}$ mode has optical frequency $(k+\frac{\phi}{2\pi})\times$FSR. In linear cavities there are simple closed-form expressions for ϕ [25], but for more

[4]FSR stands for free spectral range. The term 'longitudinal mode spacing' is sometimes also used for this.

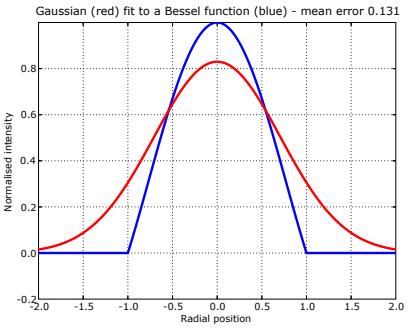

Figure 2.7: Gauss-Bessel best fit with no constraints.

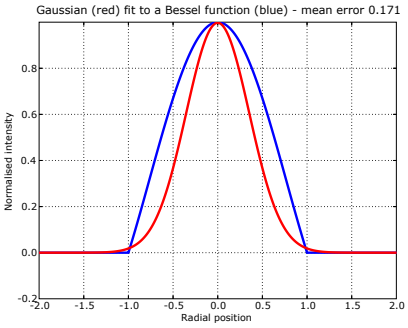

Figure 2.8: Gauss-Bessel best fit with absorbing walls.

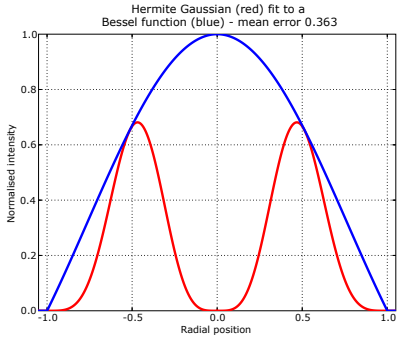

Figure 2.9: High order mode fit to a Gaussian gain profile.

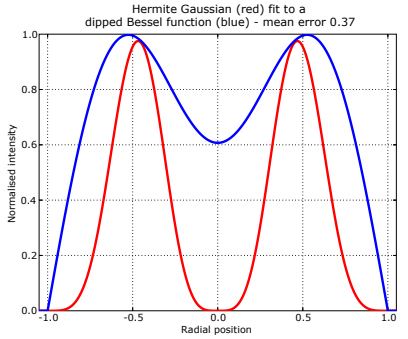

Figure 2.10: High order mode with centrally dipped gain profile.

complex cavities numerical calculations are necessary. For example it turns out that for the UG2 laser in TEM_{00} mode $\phi = 6.09$ radians and the resulting optical frequency change is $0.97 \times \text{FSR} = 2.40$ MHz. Higher order transverse modes have larger Gouy phases. For a transverse mode with indices m and n, $\phi_{mn} \approx \phi_{00}(1 + m + n)$.

The variation in gain with optical frequency and laser parameters has been well studied by this group. In general it is described by a Voight function[5]. Figure 2.11 shows an example gain curve made using typical figures for the various laser parameters.

This gain curve was made using a program by Velikoseltsev based on work by Hurst. The horizontal axis shows optical frequency in MHz where the zero on this scale is ^{20}Ne line frequency. The gain units on the vertical axis are arbitrary but a zero on this scale does represent a zero gain situation. Using the single pass gain of UG2 shown in table 2.1 and taking the FSR of 2.5 MHz we find the change in gain over one FSR at the top of the gain curve is just 1.8 parts per **billion** which is entirely negligible.

[5]A Voight function is a convolution of a Lorentz function and a Gaussian function.

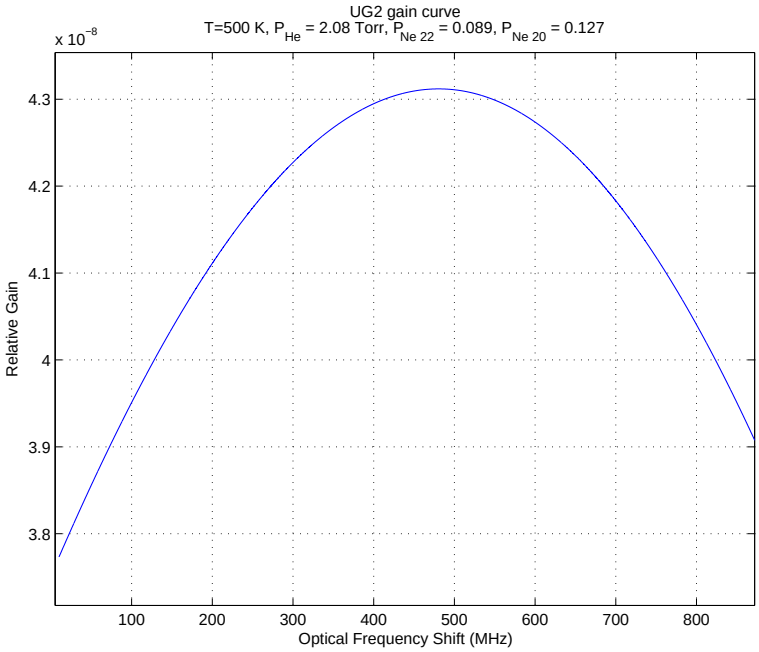

Figure 2.11: Representative composite gain curve of ^{20}Ne and ^{22}Ne in the UG2 laser. Pressures measured in Torr.

2.3.3 The McLeod model

McLeod has detailed a model of the gain distribution [25].

He begins by describing the rate equations for the helium-neon system. Collision cross sections are found for the electron—helium and helium—neon collision processes for various energy levels[6]. Since the decay rates for all levels are known a system of differential equations can be set up. Naturally these rates depend on the rate of electron collisions and hence the electron density.

Fick's law is then employed to find the rate of electron diffusion across the tube and hence the density at a given point. This is a reasonably standard problem in plasma physics and gives a Bessel function solution. Note that the diffusion rate of ions must of course be balanced by an equal and opposite electron diffusion. While full treatment would require the use of Fick's law for all eight species of atomic states (and would hence be very involved) McLeod found that the simple approximation of diffusion of 'population inversion' was sufficient.

Finally time derivatives of all the differential equations are set to zero (since we want the steady state solution) and the system solved. The result gives the expected Bessel function solution at low pump rates with a central reduction in

[6]Direct electron excitation of neon is not considered in the main model but a substantially more complicated model which includes this mechanism is presented separately. The difference in calculated gain distributions are found to be negligible.

gain developing as the pump rate is increased.

The resulting expression for population inversion N_{inv} as a function of radius is given in equation 2.6. For the remainder of this thesis this equation is referred to as the McLeod equation.

$$N_{inv} = \left[\frac{c_1}{c_2 + c_3/J_0(\rho)} - \frac{c_4}{c_5 + c_3/J_0(\rho)}\right] c_6 J_0(\rho) \tag{2.6}$$

Here $J_0(\rho)$ is a 0^{th} order Bessel function and $\rho = 2.405\frac{r}{R}$ where R is the tube radius and r is the normalised radial position from -1 to 1.

The parameters c_1 to c_6 are defined by:

$$\begin{aligned}
c_1 &= \tilde{\alpha}_{02}\tilde{N}_0 \\
c_2 &= \frac{\tilde{\alpha}_{20}}{N_0}\left(\frac{K\tilde{N}_0}{a_5} + \frac{1}{r_2}\right) \\
c_3 &= N_{\text{e0}}^{-1} \\
c_4 &= \frac{\tilde{\alpha}_{01}\tilde{N}_0}{A} \\
c_5 &= \frac{\tilde{\alpha}_{10}}{N_0}\left(\frac{K\tilde{N}_0}{a_{32}} + r_1^{-1}\right) \\
c_6 &= a_5^{-1}\left(1 - \frac{g_5 a_{52}}{g_2 a_2}\right) \approx 5.1 \times 10^{-8}
\end{aligned} \tag{2.7}$$

The quantities $\tilde{N}_0$, N_0 and N_{e0} are the number densities of ground state Helium atoms, Neon atoms and electrons respectively.

In c_4, the parameter A is defined as:

$$A = \frac{g_2 a_2 a_3}{g_5 a_{32} a_5}\left(1 - \frac{g_5 a_{52}}{g_2 a_2}\right) \approx 13.3 \tag{2.8}$$

The spontaneous decay rates of neon from the various energy levels chosen are denoted a and are known to have the values:

$$\begin{aligned}
a_2 &= 51 \times 10^6 \text{s}^{-1} \\
a_3 &= 20 \times 10^6 \text{s}^{-1} \\
a_5 &= 18 \times 10^6 \text{s}^{-1} \\
a_{32} &= 6.54 \times 10^6 \text{s}^{-1} \\
a_{52} &= 6.56 \times 10^6 \text{s}^{-1}
\end{aligned} \tag{2.9}$$

The laser level degeneracies are denoted g_5 and g_2 and it is known that $\frac{g_5}{g_2} = 0.6$.

The velocity averaged cross sections for the de-excitation processes of Helium 2^1S and 2^3S are denoted r_1 and r_2 respectively. Effectively these constants are the collision rates for Helium and Neon. Note that McLeod assumes constant cross section.

$$\begin{aligned} r_1 &\approx 3.6 \times 10^{-20} \mathrm{m}^3 \mathrm{s}^{-1} \\ r_2 &\approx 5.3 \times 10^{-19} \mathrm{m}^3 \mathrm{s}^{-1} \end{aligned} \tag{2.10}$$

The constant K is a factor to account for the reverse process modelled by the constants r; effectively the fraction of helium-neon collisions that result in an excitation of Helium due to energy taken from the colliding Neon atom. No numerical value is given for this constant.

The constants $\tilde{\alpha}_{ij}$ are defined as $\langle \tilde{\sigma}_{ij} v_e \rangle$ where $\tilde{\sigma}$ is the cross sections for excitation of Helium states by electron collision and v_e is the electron velocity. Values of the cross sections are given below:

$$\begin{aligned} \tilde{\alpha}_{01} &= 3 \times 10^{-18} \mathrm{m}^2 \\ \tilde{\alpha}_{02} &= 2 \times 10^{-18} \mathrm{m}^2 \\ \tilde{\alpha}_{10} &= 2 \times 10^{-18} \mathrm{m}^2 \\ \tilde{\alpha}_{20} &= 3 \times 10^{-18} \mathrm{m}^2 \end{aligned} \tag{2.11}$$

McLeod then fitted experimental data from Tsarkov *et al.* to the analytical model using the least squares technique. Figure 2.12 shows an example of this fit to experimental data in a situation of high pump power. The model is unfortunately not as good when it comes to fitting profiles measured at lower pump power. This is illustrated in figure 2.13. Unfortunately the quantity of data from Tsarkov *et al.* is somewhat limited and the data is poor in terms of gain and position resolution.

During the review of this model, a number of points have been raised which incorporate additional physics not yet taken into account that may resolve discrepancies in the calculated gain profiles.

Variations in collision cross section

McLeod assumes a constant collision cross section for helium-neon interactions. In reality the collision cross section is not constant, but varies with collision energy (hence electron temperature). Figures 2.15 and 2.14 show experimental measurements of the collisional cross section for helium—electron collisions plotted against electron energy.

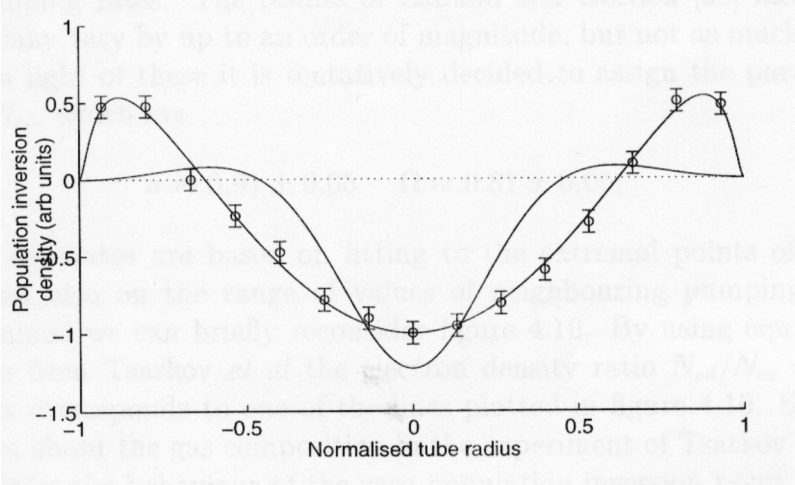

Figure 2.12: The McLeod model, used to fit some experimental data from Tsarkov *et al.* at high pump power.

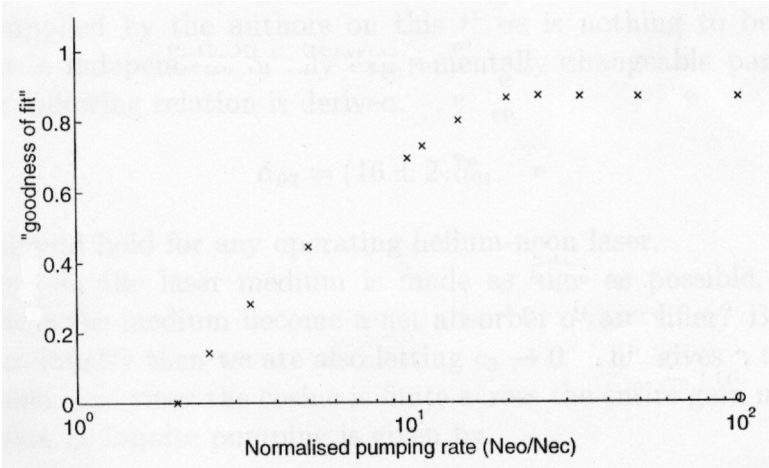

Figure 2.13: Evaluation of the quality of fit for the McLeod model to experimental data at varying pump power as presented by McLeod. Here a value of 1 on the vertical axis represents no error between the fitted profile and data.

While electron energy is not known in our situation, if we look at figure 2.2 and recognise that the *pd* product in our case is near 12 Torr-mm we see (after converting to eV) that the electron temperature is around 5 eV. From figure 2.15 we see that at this energy the cross section is changing rapidly. While 5 eV corresponds to the mean energy we are also interested in the higher energies as shown in figure 2.14 which correspond to the energy levels which excite the laser levels in neon.

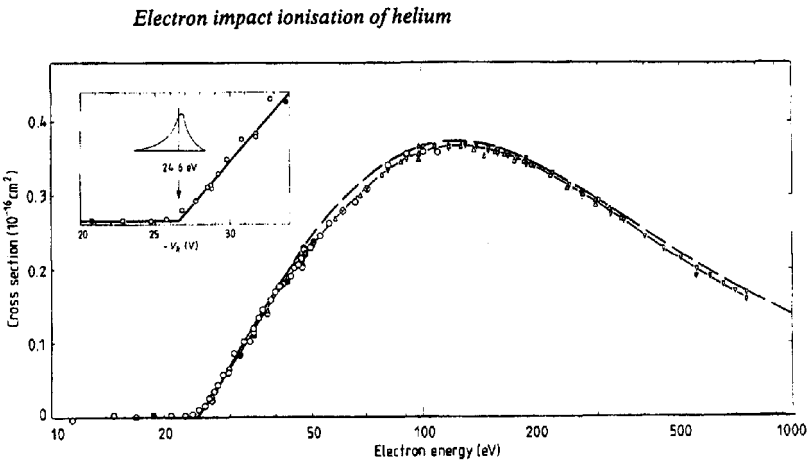

Figure 2.14: Change in collision cross sections of Helium with collision energy, high energies as measured by Monteague *et al.* [26].

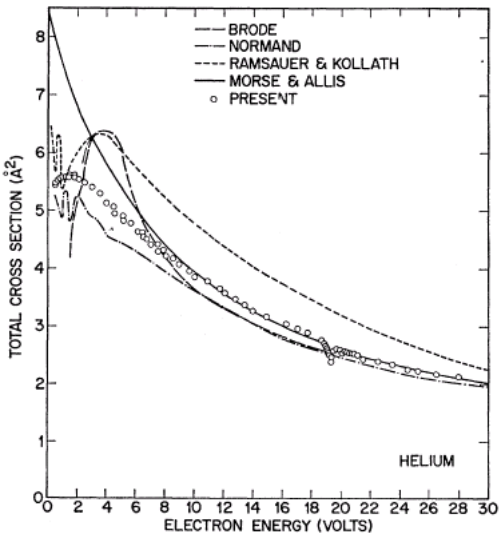

Figure 2.15: Change in collision cross sections of Helium with collision energy. Low energies measured by various authors and presented by Golden *et al.* [7].

RF pumping

McLeod does not take into consideration the RF pumping mechanism and any effect this will have on the diffusion properties of the plasma and hence the gain distribution.

Tsarkov and Molchanov [42], who measured the radial gain distribution in a RF excited (150MHz) helium-neon plasma note that the radial gain distribution differs between the case of RF and DC excitation. Their observations show that the gain does not smoothly drop of to zero at the tube walls like in the DC case, instead it remains finite at the tube edges, at least to the maximum radial resolution of their measurement technique. This can be clearly seen in figure 2.3.

Andrews and King [2] have developed a theoretical model for an RF excited helium-neon plasma and made a number of experimental measurements of gain in a RF pumped helium-neon laser [3]. They find that the laser gain for RF pumped lasers is up to 50% greater than optimum DC excitation. They note that an optimum pump frequency can be determined and this is found to be around 1 GHz. A plot of their experimental laser output power measurements for a variety of pump powers is shown in figure 2.16.

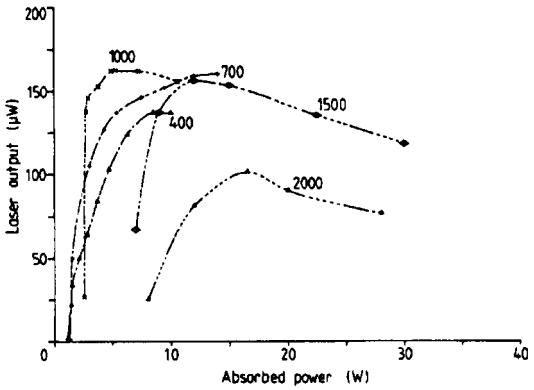

Figure 2.16: Laser output power measured at a variety of pump frequencies (MHz) by Andrews and King [3].

Energy absorption by wall collisions

McLeod assumes that when energised neon species collide with the tube walls, they are simply de-energised back to the ground state. This is a common assumption, for example used by Siegman [32] when detailing the helium-neon laser.

Results presented by Martinez [24] show that the surface of a fused silica gain tube can be decomposed as a result of bombardment by neon ions produced in an RF pumped helium-neon plasma. The byproducts of this interaction are oxygen and a reduced form of silica.

This observation has implications both for McLeod's above assumption and the lifetime of the the laser, as they note that just 0.5% oxygen reduces the gain to zero [24].

Laser gain in the plasma sheath

The existence of a sheath of excited ions near the tube wall has not been considered. Such a sheath would be expected to result in a high laser gain near the tube walls. Including this process in the model may help to resolve discrepancies in the calculated gain profiles near the tube walls.

Other corrections

One improvement that could be made to the McLeod model would be correctly describing the electron distribution by a Bessel function. For reasons of convenience McLeod approximates the 0^{th} order Bessel function with a cosine approximation. While this is a reasonable approximation near the centre of the gain tube, the cosine function differs by from the Bessel function by about 25% at the tube walls. If the model is to produce best results over the entire gain tube then the correct function will need to be used.

Chapter 3

Experimental Work

3.1 Measurement schemes

Two basic approaches to measuring the radial distribution of gain across a gain tube have been used in the past.

Both use some method to measure the change in intensity of a probe laser beam passing through the gain tube. The spot size of the probe beam is generally much smaller than the gain tube. Either the gain tube or the probe beam is moved across the diameter of the tube to build up a radial gain profile. Typically the beam makes just a single pass of the gain tube and in all cases the intensity of the probe beam is much to small to cause saturation of the gain medium.

In general the measurements that need to be made are very small and much care is needed in the design of the experiment .

3.1.1 The direct ratio method

This method involves splitting the beam from a small probe laser operating at the wavelength of interest. The average intensity of the probe laser is measured before and after it has travelled through the gain medium and the single pass laser gain is determined from the ratio of these measurements.

The gain tube can be moved relative to the probe beam to build up the complete radial profile. This method was employed in earlier work [12].

In theory this method gives the most pure result as the conditions under which the plasma and probe beam are operating are essentially identical to that of a running laser.

In practice the main difficulties with this method have been found to be:

1. Maintaining stability of both photodiode modules for the duration of the

experiment.

2. Maintaining stable plasma conditions throughout the duration of the experiment if long measurement times are necessary.

3. Cancellation of background light.

4. Susceptibility to low frequency noise sources.

In earlier work [12] these difficulties have been identified as the primary reason why previous experiments have achieved only relatively poor gain resolution (insufficient for comparison with theoretical models) over a relatively long measurement time.

The first difficulty can be circumvented through the design of high quality photodiode modules and/or software that can take into account the long term drifts of these modules.

The second difficulty can in principle be circumvented through good design of the impedance matching unit used to drive the plasma or by using the light from the discharge as the input to a servo loop used to control plasma intensity. Earlier experiments have found both approaches difficult to implement.

The third difficulty can be circumvented to some extent by placing laser line filters in front of the photodiode modules, though this does not completely eliminate all background light, especially some incoherent light from the plasma which will be within the passband of the optical filter.

A better solution involves simply subtracting the background light and for this some kind of optical shutter is necessary. The approach used previously was to modulate the probe beam using a spinning toothed wheel and then use a digital bandpass filter on the resulting signal to eliminate background light. Alternatively this could be taken a step further and a lock-in amplifier could be used. This also circumvents the last problem.

The method of modulating the probe beam does however have its share of problems. These include maintaining a sufficiently stable modulation frequency, the difficulties in filtering a square wave signal and the time required for signal processing.

3.1.2 Plasma modulation method

Here a continuous probe laser beam is directed through a gain tube containing plasma which is modulated at relatively low frequency, typically a few hundred Hertz. The beam is monitored with a suitable photodetector, the signal from which is passed to a lock-in amplifier set to the same reference signal that is used to drive the plasma. The average voltage from the lock-in amplifier is measured as is the average signal voltage and from this the laser gain can be calculated.

Spoor and Latimer [35] successfully used the second method to measure radial gain profiles in small diameter helium-neon discharges.

This method has an advantage over the first method in that only one photodetector is required and the stability of this detector is not as critical. Also as we will see in section 3.5.3, the lock-in amplifier is very good at picking a small modulated signal out of a very noisy signal.

The main disadvantage of this method when compared to the direct ratio method is that it is not as 'pure' a measurement. A discharge modulated at a few hundred Hertz is fundamentally different from a continuous discharge. While Spoor *et al.* [35] have found that a modulated plasma has an average gain approximately the same as a DC discharge energised with the same average power this is only an approximation.

Another disadvantage which is specific to our situation of RF excited discharges is that the plasma cannot be 100% modulated at low power because otherwise the discharge will stop. In order to keep the discharge running we have to use a modulation with a DC offset of approximately 20%. This means that we will always slightly underestimate the gain because we can't measure the contribution of this lower level.

3.2 Optical Setup

The apparatus was designed the be ammeniable to both the direct ratio and plasma modulation methods. Figure 3.1 shows the optical setup for the experiment. Figure 3.2 shows a photograph of the apparatus.

The probe beam is generated by a small helium-neon laser, to which a beam expander is attached and adjusted such that a waist occurs at the gain tube under test. Double polarisers both allow easy adjustment of the probe beam intensity and ensure that the polarisation of the probe beam remains constant since the splitting ratio of the beam splitter changes with polarisation.

The purpose of the small converging lens in front of each photodiode module is to ensure that the same area of the photodiode is used for measurement even if the beam moves slightly relative to the optical table due to vibration.

The polariser, laser line filter and aperture in front of the window W1 work together to ensure that any incoherent light from the plasma is not reflected backwards through the beam splitter and into the first photodiode module. This arrangement has been shown to block all but 0.25 ppm of the incoherent light that would otherwise be reflected.

Alignment of this optical system is critical and has been fully documented in earlier work [12].

A stepper motor drive system is used to move the laser gain tube across the probe beam, which has been focused to a waist at the position of the gain tube. This system provides a resolution of 1.25 μm.

Computer controlled solenoid beam shutters are placed before the beam splitter and after the gain tube.

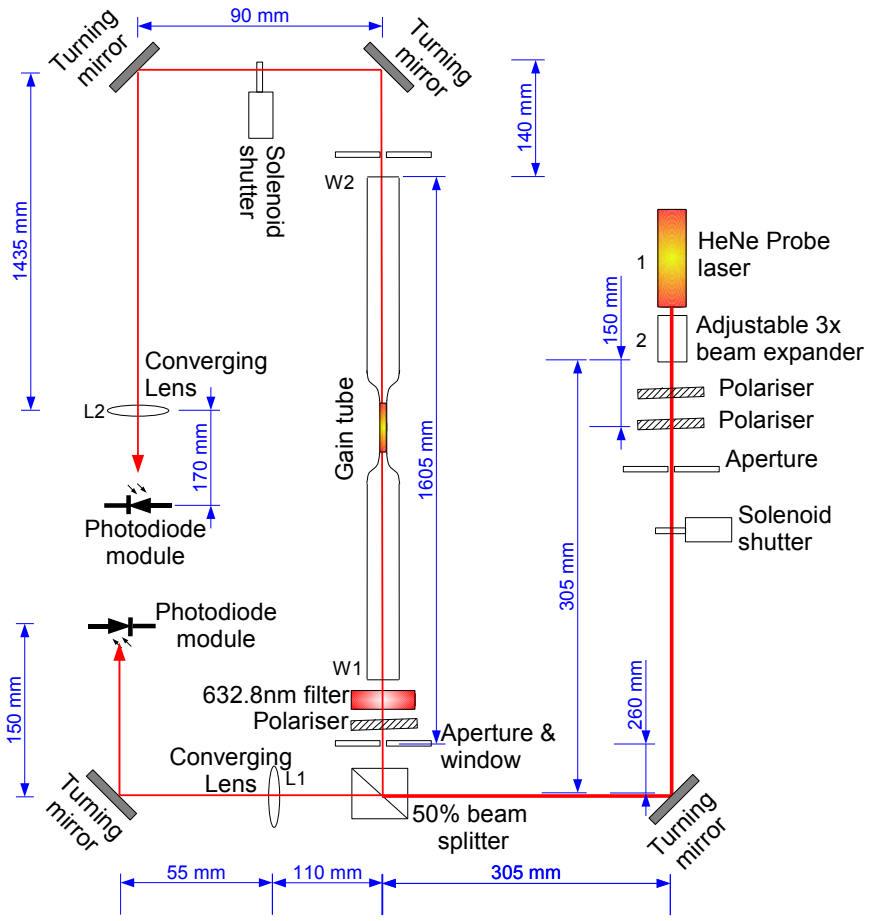

Figure 3.1: Diagram of optical setup.

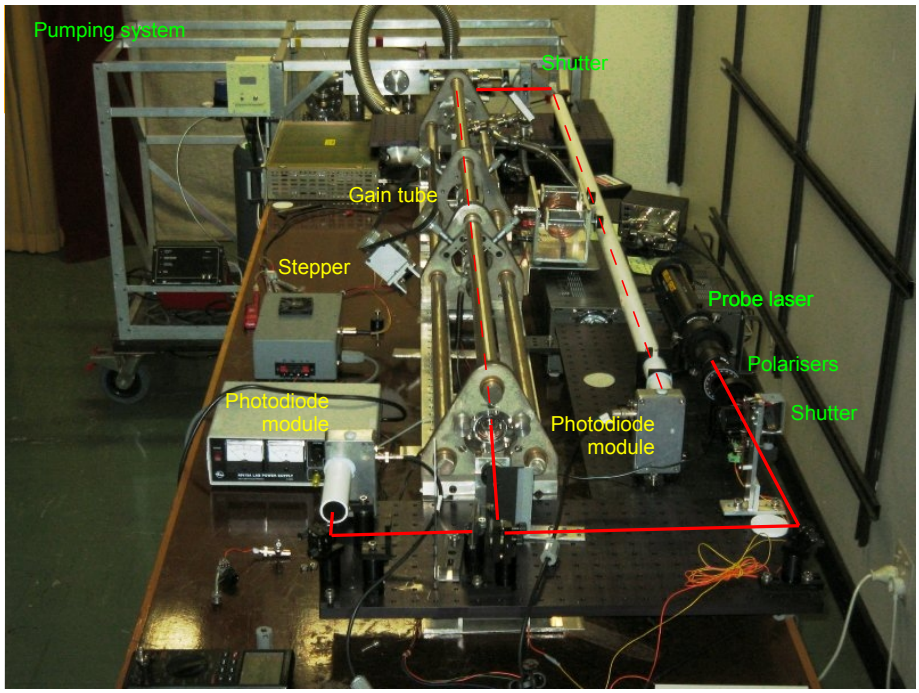

Figure 3.2: Photograph showing apparatus.

3.2.1 Probe laser

The probe laser is a small 5 mW helium-neon laser (Melles Griot 05-LHP-111). Unfortunately the gas mix and neon isotope ratio are not known.

The original power supply for this laser was found to be problematic as it was responsible for mains ripple on the laser light of around 0.4%. This made differentiating between sources of 50Hz interference difficult.

A solution was to upgrade to a more stable high voltage power supply. The Thorn EMI PM218R supply was chosen. This supply has an output adjustable from 1.0 to 3.2 kV to an accuracy of 100 mV and ripple of 0.002% [41]. While sufficient for running the laser tube, it cannot provide the ≈10 kV needed to cause the discharge to strike so it was necessary to construct a starter circuit capable of generating this voltage.

Figure 3.3 shows the circuit that was built for this purpose. The approach is quite novel — a piezoelectric element from a gas lighter was used to generate the necessary high voltage. When the trigger on the lighter is pressed the resulting high voltage spike is rectified by a high voltage diode D1 (actually 15 1N4007 1kV diodes in series) and essentially drives a charge pump formed with another similar diode D2 and 12 pF capacitor Cf. Rb is the ballast resistor which is 75 kΩ (as recommended by the manufacturer for this laser) and made with 8 1/4 W resistors in order that it can safely dissipate 2 W. D3 and D4 are basically provided simply for safety to isolate the high voltage power supply and are

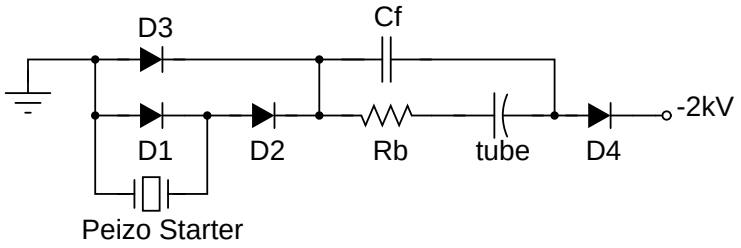

Figure 3.3: Piezo laser starter circuit

probably not strictly necessary.

The starter has been found to work reliably when the power supply is set to deliver 2.6 kV. Typically 5-10 presses are needed to build up enough charge to strike the discharge, after which the supply is adjusted to 2.4 kV.

3.2.2 Beam movement

Throughout this work, unsatisfactory measurement resolution has been a constant problem. While all of the optical components have been securely attached to an optical table, some vibration is inevitable. This section details the derivation of a general formula which can be used to calculate the error due to vibration of an optical surface. Measurements of vibration are made and the resulting error calculated.

Angular variation measurement

The vibration angle has been measured by looking at the variation in photodiode signal when 50% of the beam was blocked by an obstruction.

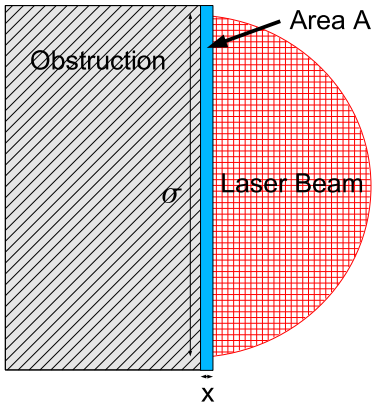

Figure 3.4: Arrangement for measuring beam vibration

If $dV_{50\%}$ and $dV_{0\%}$ are the variations in voltage when the beam is 0% occluded

and 50% occluded then the change in total area A of the beam is:

$$\frac{dA}{A} = \frac{dV_{50\%} - dV_{0\%}}{\mid V_{0\%} \mid} \tag{3.1}$$

If the beam has width σ then from geometry:

$$\frac{dA}{A} A = \pi \left(\frac{1}{2}\sigma\right)^2 \left[\frac{dV_{50\%} - dV_{0\%}}{\mid V_{0\%} \mid}\right] \tag{3.2}$$

If we consider figure 3.4 we see that for small changes in transverse position we can approximate the change in area as a rectangle of area $dA = \sigma x$. Therefore:

$$x = \frac{\sigma\pi}{4} \left[\frac{dV_{50\%} - dV_{0\%}}{\mid V_{0\%} \mid}\right] \tag{3.3}$$

So if the obstruction is a distance L away from the optical surface which is vibrating then the change in angle $d\alpha$ due to vibration is thus:

$$\begin{aligned} d\alpha &= \sin^{-1}\left(\frac{x}{L}\right) \\ &= \sin^{-1}\left(\frac{\sigma\pi}{4L}\left[\frac{dV_{50\%} - dV_{0\%}}{\mid V_{0\%} \mid}\right]\right) \end{aligned} \tag{3.4}$$

From experiment it was found that the net variation in recorded intensity due to the obstruction was 775 ± 117 ppm at a distance of 40 ± 2 mm with a beam diameter of $1 \pm .2$ mm. This yields a vibration angle of:

$$d\alpha = (15 \pm 2) \times 10^{-6} \text{ rad} \tag{3.5}$$

Derivation of lens transmission with respect to incident angle

A beam normally shining through the centre of a lens, then perturbed by a small angle α will suffer additional losses since the reflected intensity from a dielectric barrier varies with incident angle and the path length through the (absorbing) glass will be different.

It is useful to derive a general equation for these losses as a function of angle. Consider the ray diagram shown in figure 3.5. We assume that the radius of curvature of the lens is sufficiently large compared to the diameter of the laser beam that we can consider the point of contact to be flat.

We begin by noting from the sine rule applied to triangle OI_1O_2 that:

$$\frac{\sin\alpha}{R_2} = \frac{\sin\beta}{d + R_2} \tag{3.6}$$

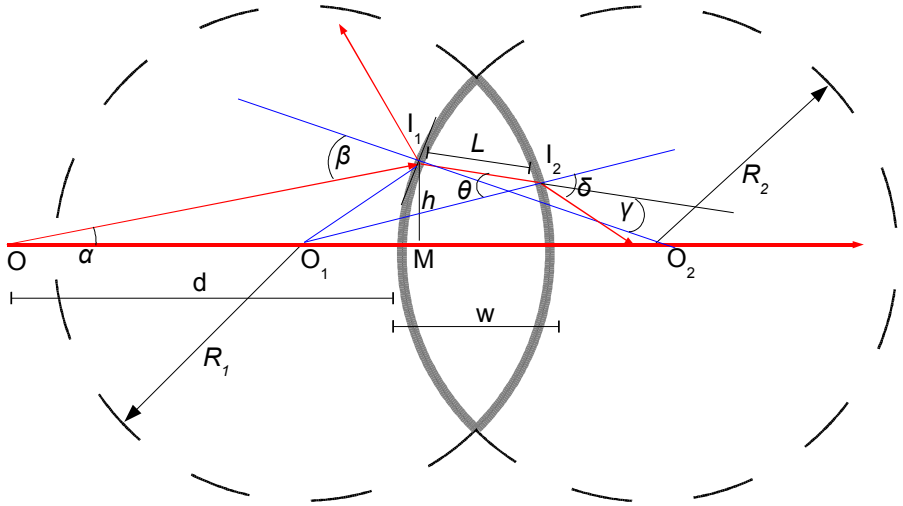

Figure 3.5: Ray diagram of a beam travelling though a lens when the ray is perturbed by an angle α.

So by the small angle approximation:

$$\beta = \alpha \frac{d + R_2}{R_2} \tag{3.7}$$

The angle γ can be found by employing Snell's law. We denote the refractive index of the lens by n and assume the refractive index of air to be 1.

$$1 \sin \beta = n \sin \gamma \tag{3.8}$$

$$\sin \gamma = \frac{\sin \beta}{n} = \sin \alpha \frac{d + R_2}{R_2} \frac{1}{n} \tag{3.9}$$

Therefore:

$$\boxed{\gamma \simeq \alpha \frac{d + R_2}{R_2} \frac{1}{n} \simeq \frac{\beta}{n}} \tag{3.10}$$

We need to find the path length through the (absorbing) lens and the angle θ to determine the loss due to reflection from the inside surface of the lens.

In order to do this we first need to find h. We do this by first finding the distance $\| \overline{OI_1} \|$ and $\| \overline{OM} \|$ using the sine rule:

$$\frac{\sin(\beta-\alpha)}{\parallel \overline{OI_1} \parallel} = \frac{\sin\alpha}{R_2} \tag{3.11}$$

$$\parallel \overline{OI_1} \parallel = \frac{\sin(\beta-\alpha)}{\sin\alpha} R_2 \tag{3.12}$$

$$\parallel \overline{OM} \parallel = OI_1 \cos\alpha = R_2 \frac{\sin(\beta-\alpha)}{\sin\alpha}\cos\alpha \simeq R_2 \frac{\beta-\alpha}{\alpha} \tag{3.13}$$

$$h = \parallel \overline{OI_1} \parallel \sin\alpha = R_2 \sin(\beta-\alpha) \simeq R_2(\beta-\alpha) \tag{3.14}$$

We can now go ahead and find the angle θ, also donated by $\widehat{O_1I_2I_1}$. We first need the distances $\parallel \overline{OO_1} \parallel$, $\parallel \overline{O_1M} \parallel$ and $\parallel \overline{O_1I_1} \parallel$.

$$\begin{aligned}
\parallel \overline{OO_1} \parallel &= d - R_1 + w && (3.15)\\
\parallel \overline{O_1M} \parallel &= \parallel \overline{OM} \parallel - \parallel \overline{OO_1} \parallel \\
&= \frac{\sin(\beta-\alpha)\cos\alpha}{\sin\alpha} R_2 - d + R_1 - w \\
&\simeq \frac{\beta-\alpha}{\alpha} R_1 - d + R_1 - w && (3.16)\\
\parallel \overline{O_1I_1} \parallel &= \sqrt{\parallel \overline{O_1M} \parallel^2 + h^2} && (3.17)
\end{aligned}$$

We now employ the sine rule to calculate the associated angles from which we can find θ.

$$\begin{aligned}
\sin\widehat{OI_1O_1} &= \frac{\parallel \overline{OO_1} \parallel}{\parallel \overline{O_1I_1} \parallel}\sin\alpha \\
&\simeq \alpha \frac{d - R_1 + w}{\parallel \overline{O_1I_1} \parallel} && (3.18)
\end{aligned}$$

$$\widehat{O_1I_1O_2} = \pi - \beta - \widehat{OI_1O_1} \tag{3.19}$$

$$\widehat{O_1I_1I_2} = \widehat{O_1I_1O_2} + \gamma \tag{3.20}$$

$$\sin\widehat{O_1I_1I_2} = R_1 \frac{\sin\theta}{O_1I_1} \tag{3.21}$$

$$\boxed{\theta = \sin^{-1}\left(\frac{\parallel \overline{O_1I_1} \parallel}{R_1}\sin\widehat{O_1I_1I_2}\right)} \tag{3.22}$$

From θ we simply employ Snell's law to calculate δ :

$$\boxed{\delta = \sin^{-1}\left(n\frac{\parallel \overline{O_1I_1} \parallel}{R_1}\sin\widehat{O_1I_1I_2}\right)} \tag{3.23}$$

The only remaining information we we need to find L is dependent on $\widehat{I_1O_1I_2}$:

$$\widehat{I_2O_1O_2} = \gamma + \theta - \beta + \alpha \tag{3.24}$$

$$\widehat{I_1O_1O_2} = \tan^{-1}\left(\frac{h}{\parallel \overline{O_1M} \parallel}\right) \tag{3.25}$$

$$\begin{aligned}\widehat{I_1O_1I_2} &= \widehat{I_1O_1O_2} - \widehat{I_2O_1O_2} \\ &= \widehat{I_1O_1O_2} - (\gamma + \theta - \beta + \alpha)\end{aligned} \tag{3.26}$$

Finally we now find the distance L using the sine rule.

$$\boxed{\parallel \overline{I_1I_2} \parallel = \parallel \overline{O_1I_1} \parallel \frac{\sin\widehat{I_1O_1I_2}}{\sin\theta} = L} \tag{3.27}$$

We have now established all the geometry necessary to determine the intensity transmission coefficient as a function of incident angle.

The transmission coefficient τ for polarisation perpendicular to the plane of incidence is given by the Fresnel equation 3.28 [14]. n_1 and n_2 are the refractive indices of the first and second media. The angles of the incident and transmitted beams to the normal of the interface are denoted ϕ_i and ϕ_t respectively. We assume that both media are non magnetic.

$$\tau = 1 - \left[\frac{n_1\cos\phi_i - n_2\cos\phi_t}{n_1\cos\phi_i + n_2\cos\phi_t}\right]^2 \tag{3.28}$$

We now express the intensity transmission coefficients as a result of reflection from the first and second interface τ_1 and τ_2. n is the refractive index of the glass.

$$\tau_1 = 1 - \left[\frac{\cos\beta - n\cos\gamma}{\cos\beta + n\cos\gamma}\right]^2 \tag{3.29}$$

$$\tau_2 = 1 - \left[\frac{n\cos\theta - \cos\delta}{n\cos\theta + \cos\delta}\right]^2 \tag{3.30}$$

The beam also suffers attenuation as it travels the distance L due to scattering and absorption in the glass. The transmitted irradiance T_i as a function of distance x is given by the absorption coefficient μ.

$$T_i = e^{-\mu x} \tag{3.31}$$

Typically the internal transmittance T_i is tabulated as a function of wavelength for two distinct thicknesses x_1 and x_2 and μ must be found from these. Following the recommendation of Melles Griot [13] we find μ as follows in equation 3.32.

$$\mu = -\frac{1}{2}\left[\frac{\log(T_i(x_1))}{x_1} + \frac{\log(T_i(x_2))}{x_2}\right] \tag{3.32}$$

With this knowledge we can finally give an expression for the total light intensity after transmission through a lens.

$$\boxed{I_t = I_0\tau_1\tau_2 e^{-2\mu L}} \tag{3.33}$$

Evaluation of losses due to vibration

The following table shows results of calculations to find the uncertainty in the intensity transmission coefficient for each optical component and the necessary data used in the calculation. In each case the previously measured value of $d\alpha$ ($d\alpha = (15\pm2)\times10^{-6}$ rad) has been used to find $\tau_1\tau_2 e^{-2\mu L}$ and the corresponding value found when $\alpha = 0$ subtracted to find $\Delta\tau$.

Unfortunately data pertaining to the internal transmittance of the Corning 7056 glass, an alkali borosilicate glass was not available from the manufacturer. In the following calculations we want to know maximum uncertainty for the worst case. For this reason we use the worst transmittance of any borosilicate glass tabulated in the Melles Griot catalogue [13].

	L1	W1	W2	L3
Component	convex lens	flat window	flat window	PCX lens
Glass	BK7	7056	7056	BK7
n	1.515	1.487	1.487	1.515
μ	.1201	.4810	.4810	.1201
d	110 mm	260 mm	1865 mm	2175 mm
R_1	200 mm	∞	∞	∞
R_2	200 mm	∞	∞	100 mm
w	5 mm	3.11 mm	3.11 mm	5 mm
$\Delta\tau$	2.7×10^{-11}	9.3×10^{-10}	7.1×10^{-7}	6.6×10^{-9}

3.2.3 Photon counting

The only other fundamental limitation in the optical setup arises from photon counting statistics. We need to take into account the quantum efficiency η of the diode (typically around 0.8), the relative spectral sensitivity $S(\lambda)_{rel}$ at the laser wavelength (0.6 in this case). If the measurement time is 1 second and the incident laser power p is 1 mW then the uncertainty due to photon counting is given by equation 3.34. c and h are the speed of light and Plank constant respectively.

$$\frac{\lambda \ p \ \eta \ S(\lambda)_{rel}}{c \ h} = \mathbf{3.3{\times}10^{-7}} \ \mathbf{ppm} \tag{3.34}$$

3.3 Mechanical Setup

3.3.1 Shutters

As the measurement procedure requires measurements under different conditions of light incident on the photodiodes (see section 3.5), it was necessary to design mechanical shutters to block a laser beam under software control.

Such a shutter is required to be reliable, have both reasonably rapid (<100 ms) and consistant opening and closing times, not exhibit bounce or excessive vibration when it opens or closes and operate from a TTL signal.

Several designs were experimented with, and the best design was found to be a solenoid based system, as shown in figure 3.6. A solenoid is mounted vertically on an aluminium bracket which can be easily attached to an optical bench. A small piece of card is attached to the core and a bolt which passes through the end of the core is arranged to move in a slit cut in the aluminium bracket which limits the motion of the core and prevents it from falling out of the solenoid. An o-ring placed over the solenoid core provides some vibration damping, as do a series of o-rings used as washers to isolate the assembly when bolting it to the optical table.

Figure 3.7 shows the circuit used to drive the solenoid. The circuit is constructed on a strip of prototype board and mounted on the aluminium bracket. The basic principle behind this design is that more current is required to close the shutter than to keep it closed, and the higher the voltage the faster the switching occurs. It is undesirable to have an unnecessarily high current flowing through the solenoid coil at all times as it produces significant heating of the solenoid, bracket and thus optical bench. Also, the core will eventually become magnetised.

The operation of the circuit is as follows: When the input TTL signal is low, the potential difference between the gate and drain of the 2N7000 N-channel MOSFET will be zero and so the transistor will be off. The gate of the IRF9540N P-channel MOSFET will be held at a high potential by R2 and thus current cannot flow through the solenoid and the solenoid will be closed. Meanwhile,

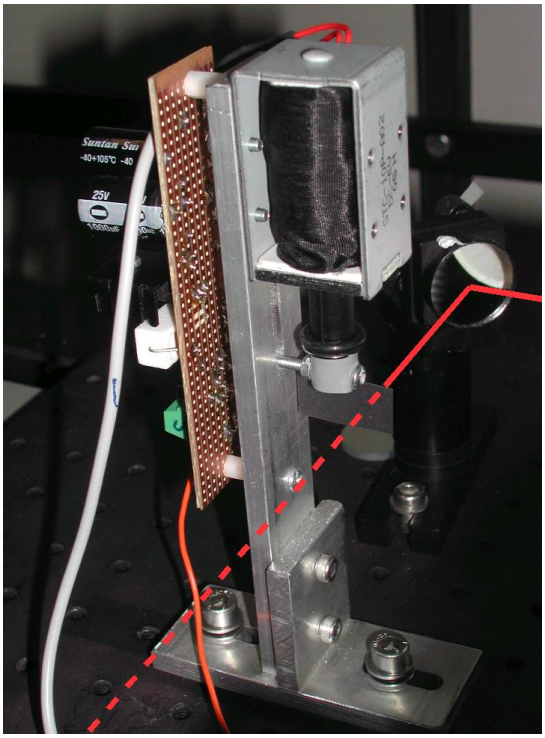

Figure 3.6: Solenoid beam shutter with beam line superimposed

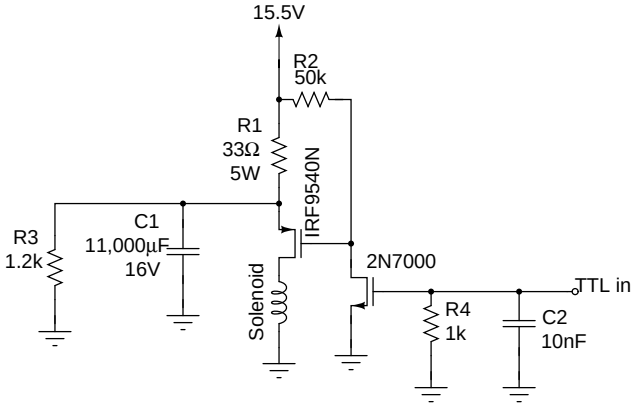

Figure 3.7: Solenoid beam shutter driver circuit

Capacitor C1 will have charged to the supply voltage via R1.

When the TTL signal goes high, the N-channel MOSFET will switch on causing current to flow through R2 to ground and thus a potential will develop between source and gate of the P-channel MOSFET resulting in it switching on and allowing C1 to rapidly discharge via the resistance of the solenoid coil providing sufficient current to close the solenoid. The solenoid will then remain closed as long as the TTL signal remains high, via current flow which is limited by R1.

Capacitor C2 is required to bypass RF frequencies and prevent RF fields from triggering the shutter. R4 sets the input impedance while R3 is provided for safety to ensure that charge built up on C1 is discharged shortly after the power supply is disconnected. The value of these components is not critical.

The particular solenoids used had a coil resistance R_{coil} of 7Ω and when operating from a 12V supply required a current I_0 of 1.7A initially to close and 0.3A to remain closed (I_c). The resistance and power of R1 are thus trivially calculated by equations 3.35 and 3.36 to be 33Ω and 3.6 W respectively.

$$R_2 = \frac{V}{I_c} - R_{coil} \tag{3.35}$$

$$P_{R_2} = I_c^2 R_2 \tag{3.36}$$

The solenoid was measured to take at most 33 ms (t_c) to close, so by equating the electrical energy required over this time with the energy stored in a capacitor we find the capacitance of capacitor C1 to be:

$$\begin{aligned} C_1 &= \frac{2t_c I_0}{V} \\ &\approx 10,000\mu F \end{aligned} \tag{3.37}$$

One disadvantage of this design is that since R1 limits the charging time of C1, the maximum switching frequency of the shutter will be limited. This could be circumvented by adding another MOSFET in parallel with R1, at the expense of additional complexity.

3.3.2 Vacuum setup

Figure 3.8 shows the setup for all the vacuum equipment used to evacuate the laser cavity and fill it with various Helium and Neon gas mixtures at various pressures. The gas supplies used are all instrument quality and the Neon supply is 90.48% Ne^{20}, 0.27% Ne^{21} and 9.25% Ne^{22}.

A backed turbomolecular pump is used to evacuate the system. It is connected through a normally closed pneumatic valve which is held open with pressure from a nitrogen cylinder. A solenoid valve is used so that in the event of power failure to the backing pump the pneumatic valve closes automatically to avoid damaging the turbomolecular pump.

The procedure for filling with gas is to first close the pneumatic valve and then shuffle some gas through the pipework from a cylinder by alternately opening then closing the helium cylinder valve and then the two valves following it. The three series valves are opened to the cavity and the regulable valve to the manifold is opened slightly while the pressure is monitored on the pressure gauges. The procedure is repeated for the neon. It is important to wait for about 5 minutes after filling for the gas in the cavity to mix before closing the three series valves to the cavity since the volume of the cavity is smaller than that of the plumbing in the pumping system.

The volume of the cavity was measured as 0.80±0.05 L and the volume of the plumbing and pumping system, as measured by the pressure change when the cavity is opened is 4.86±0.05 L

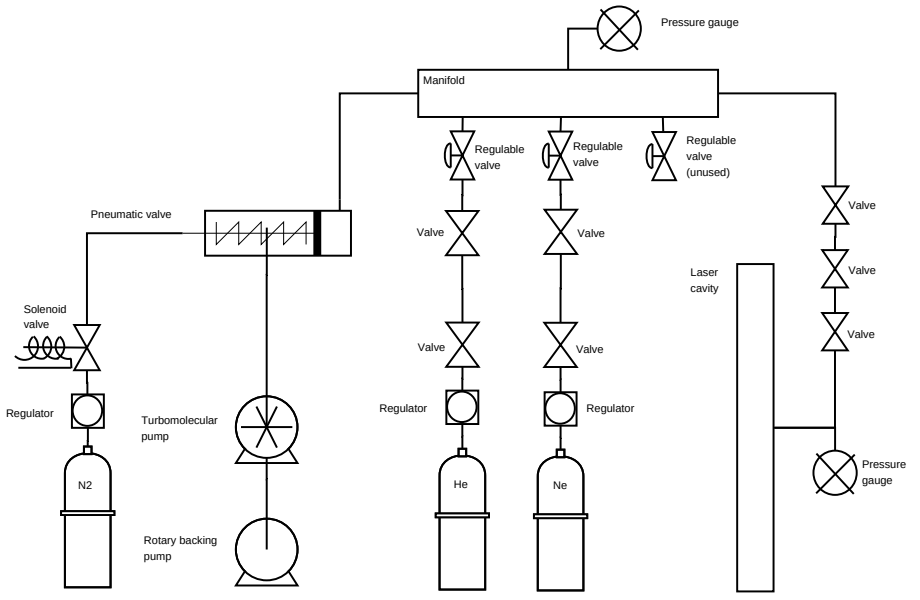

Figure 3.8: Vacuum setup

3.3.3 Gain tube position controller

The gain tube is connected to the pipework by flexable bellows. A pair of springs apply an upward force on the tube, the position of which can be adjusted both horizontally and vertically by adjusting four micrometers. Two of the micrometers are kept fixed so that when the other two are adjusted the gain tube is displaced horizontally while staying in the same vertical position.

The micrometers requiring adjustment each have 40mm diameter metal cogs attached. A toothed rubber belt passes over these cogs and another which is mounted on a large 400 step/revolution stepper motor as shown in figure 3.9. This arrangement allows measurement to a resolution of 1.25 μm.

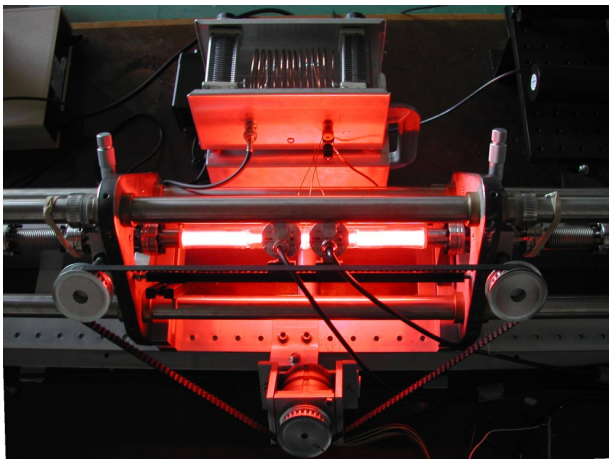

Figure 3.9: Arrangement for automated movement of the gain tube. Also shown is the impedance matching unit.

The circuit used to drive the stepper motor from under software control is based on a original circuit by Ross Ritchie (University of Canterbury) but has been extensively modified to provide more power (necessary for the stepper motor to supply the required torque) and provide an 'enable' control which allows the current going to the motor coils to be switched off when the motor is not moving. This is to keep the motor and control circuit cool and prolong its life.

The heart of the circuit is the L297 stepper motor controller chip. This responds to TTL signals which allow the direction to be set and the stepping to be controlled. This drives a 40109 level converter chip which steps up the TTL outputs to 12V which is necessary to drive the FETs used to drive the motor coils. In addition a 2N7000 MOSFET operates as a switch which disables the L297 chip and thus the stepper motor when the gate is low. This part of the circuit is shown in figure 3.10.

Figure 3.11 shows the circuitry which drives the individual motor coils. This is duplicated in order to control all four motor coils.

Figure 3.12 shows the power supply for the circuit which is a standard linear

design.

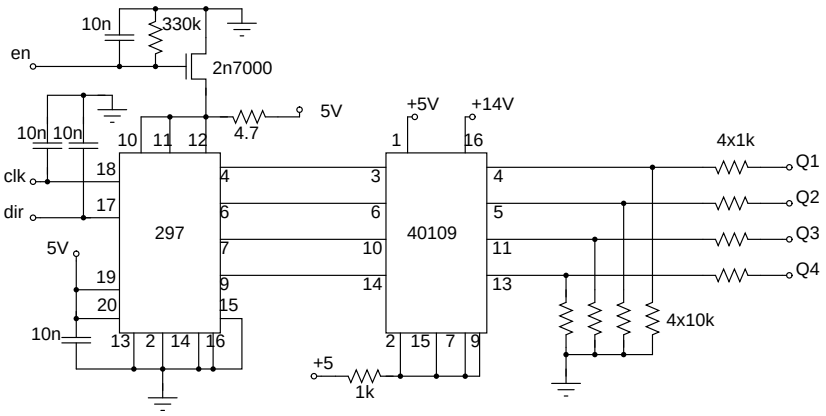

Figure 3.10: All logic circuitry for the stepper motor controller

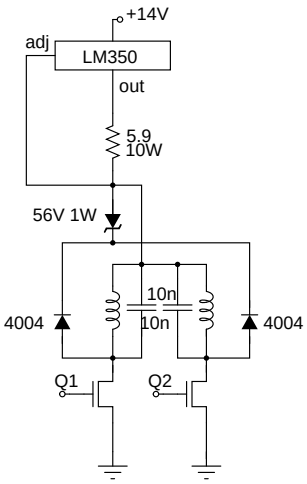

Figure 3.11: Motor driver circuitry for the stepper motor controller

3.4 Electrical Setup

Previous experiments [12] have identified poor performance of the photodiode amplifier modules — DC drifts, noise and susceptibility to RF interference as a primary reason for poor gain resolution and the very long measurement times that were necessary.

The general approach here was to design the best photodiode amplifier module to eliminate these problems.

3.4.1 Photodiodes

How they work

A photodiode is essentially a semiconductor diode that functions as a photodetector. Photodiodes are generally created by forming a either a P-N junction or P-I-N structure (see figure 3.13).

When photons with sufficient energy strike a semiconductor they are absorbed, resulting in the generation of mobile electrons and holes. If the absorption occurs in the junction's depletion region then these carriers will be swept away from the junction by the field in the depletion region. This results in a *photocurrent* [4].

This mechanism gives the photodiode an inherently linear response with respect to input light intensity — essential for this experiment. Figure 3.14 illustrates this for the BPW34 photodiode chosen for this experiment.

The efficiency of a photodiode does of course depend on the wavelength of the incoming photon. This dependence for the BPW34 is illustrated in figure 3.15. From this we note that the gradient at 633 nm $\frac{dS}{d\lambda} = 0.00217$ nm^{-1}. A typical helium-neon gas laser has a gain bandwidth of approximately 1.5 GHz (0.002 nm), the total error in intensity measurement ΔI due to variation in optical frequency of the probe laser is thus:

$$\Delta I = \frac{dS}{d\lambda} d\lambda \approx \mathbf{4.34\ ppm} \tag{3.38}$$

However it should be noted that when taking a ratio of two beams there will be no change in the output with respect to optical frequency as the light incident on both photodiodes has the same optical frequency.

Amplifier circuit details

Photodiodes are generally used in one of two different modes. In the *photovoltaic* mode, no bias is supplied. Light falling on the diode will cause a voltage to develop across the junction which leads to a current flow in the forward bias direction.

In the *photoconductive* mode, the device is reverse biased in which case the diode will have very high resistance unless light is shining on it. A diode used

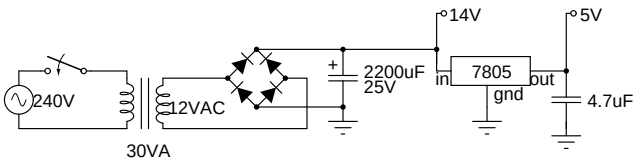

Figure 3.12: Power supply for the stepper motor controller

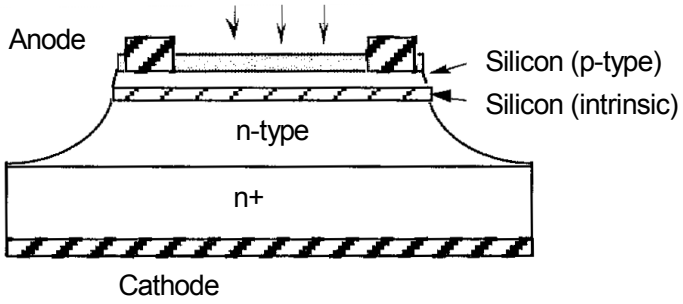

Figure 3.13: Structure of a P-I-N photodiode [4]

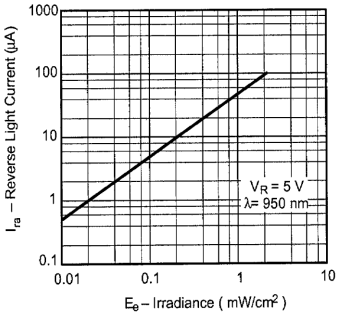

Figure 3.14: BPW34 linearity from data sheet measured over a small range [31].

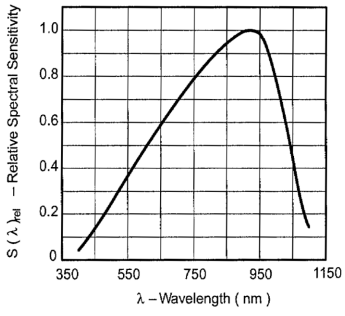

Figure 3.15: BPW34 spectral sensitivity [31].

in this mode can be used as a photodetector by monitoring the current running through it. This mode of operation generally results in a circuit which is the most sensitive. It is the recommended mode for high resolution, highly linear measurements [11, 29].

The circuit shown in figure 3.16 is a basic *transimpedance amplifier*. It converts the photocurrent produced by the photodiode into a voltage. Since no current flows into the op-amp itself, the photo-current has nowhere to go but through the feedback resistor R_f. Since the non-inverting input is held at ground potential the output of the op-amp is such that the inverting input, along with the feedback resistor must be held at 0V. The output voltage can thus be described as the voltage across the feedback resistor R_f.

The purpose of the capacitor C_f is to balance the capacitance inherent in the photodiode. If this is not done then oscillation will result. The capacitance of the BPW34 photodiode selected for this experiment is about 17 pF at reverse voltage of 9 V hence we require $C_f > 17$ pF.

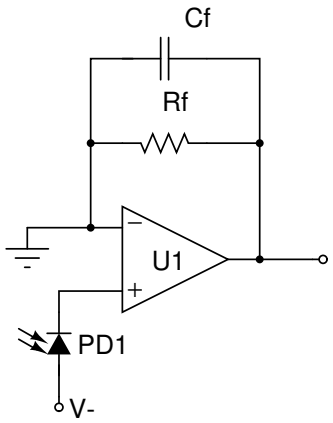

Figure 3.16: The basic transimpedance photodiode amplifier

3.4.2 Aside: The chopper stabilised / auto zero amplifier

The operational amplifier selected for this experiment is the LTC 1050 from Linear Technology. This device is a *chopper stabilised* or *auto-zero* amplifier.

The main advantage of using an amplifier of this design is the incredible DC performance; they essentially eliminate offset, drift and 1/f noise. This particular device is quoted to have a input offset thermal drift of 10nV/℃, long term offset drift of $50\text{nV}/\sqrt{\text{Month}}$ and input noise voltage from DC to 1 Hz of $0.6\mu V_{pp}$ or $1.6\mu V_{pp}$ from DC to 10 Hz [40]. These specifications are unmatched by any other op-amp design.

Based on these specifications (assuming the difference in temperature of the two photodetectors located in the same room is at most 1℃) and the recommendation of linear technology [40] for a near DC signal when samples are taken

over a period of $\approx$ 1 s (1μV peak to peak noise), we can quote the maximum uncertainty in a 8 V signal to be:

$$\Delta V = \frac{1.001 \times 10^{-6}\ \text{V}}{8\text{V}} \approx \mathbf{0.13\ ppm} \tag{3.39}$$

How they work

Figure 3.17 shows a simplified diagram (drawn with mechanical switches for clarity) of the internals of a chopper stabilised amplifier.

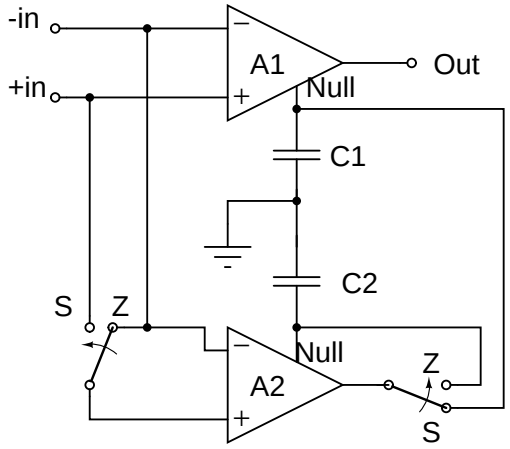

Figure 3.17: Simplified chopper stabilised / auto zero amplifier

The circuit consists of two operational amplifiers. A1 is the main amplifier, and A2 is the *nulling amplifier*.

The switches change from the sample (S) position to the zero (Z) position at a rate typically around 2kHz. When in the sample position the nulling amplifier monitors the input offset voltage of the main amplifier and its output voltage is applied to the 'offset null' control of the main amplifier.

The nulling amplifier also of course has its own input offset voltage. This offset must also be corrected before it is used to null the main amplifier. This is effectively what happens then the switch is in the zero (Z) position — now the nulling amplifier is disconnected from the main amplifier and its inputs are effectively shorted together with the output connected back to the amplifiers own offset null control. This correction voltage is stored by the capacitor C1. C2 similarly holds the correction voltage for the main amplifier during sample mode.

Unlike a conventional bipolar op-amp in which the noise bandwidth increases

towards a limit of 1/f as the frequency is decreased towards DC, a chopper stabilised amplifier's noise decreases with frequency and at frequencies below about 1Hz it essentially remains constant. This is because low frequency noise looks like a offset error to the auto-correction circuitry and this autocorrection becomes more efficient as the frequency approaches DC [28]. This makes this design ideal for precise DC voltage measurements.

Disadvantages: Switching transients

One disadvantage often overlooked with chopper stabilised amplifiers results from the small switching transients which are produced at the chopping frequency.

These transients are a result of capacitive coupling of the switching transistor base voltage into the storage capacitors as the 'switches' open and close [28]. This results in short transient peaks occurring at the chopping frequency. Though short, when integrated these transients result in an equivalent noise voltage very large compared to the wideband noise floor of the amplifier quoted by the manufacturer. They can be a significant problem if they fall within the frequency band of interest.

In addition, small differences between the gain bandwidth of the main and nulling amplifiers cause the closed loop gain to alternate slightly with the clock frequency.

At first inspection one may think that the general approach to removing this kind of high frequency noise is to reduce the bandwidth of the circuit by increasing C_f or attaching a low pass filter to the output. However this approach does not work.

When a transient occurs on the output (say, 1 μs long), the capacitor C_f will briefly have much smaller reactance than the feedback resistor and this will result in charge injection to the input of the amplifier. As the circuit has high gain the effect of increasing C_f is to **increase** the duration and peak voltage of the transient!

The same effect often occurs if a low pass filter is attached to the output as generally this will consist of a capacitor to 'ground'. Care must be taken to avoid any ground loop that might inject charge into the grounded non inverting input.

Generally the best approach to this problem would be to minimise any capacitance between the input and output terminals, however as was noted in section 3.4.1, we require at least 17 pF. When a 27 pF capacitor was used here the resulting transient lasted about 1 μs and had a peak-to-peak voltage of around 100 mV.

3.4.3 Photodiode amplifier construction

Circuit details

Figure 3.18 shows the complete circuit for the photodiode amplifier. Figure 3.20 shows the printed circuit board that was designed to accommodate the circuit.

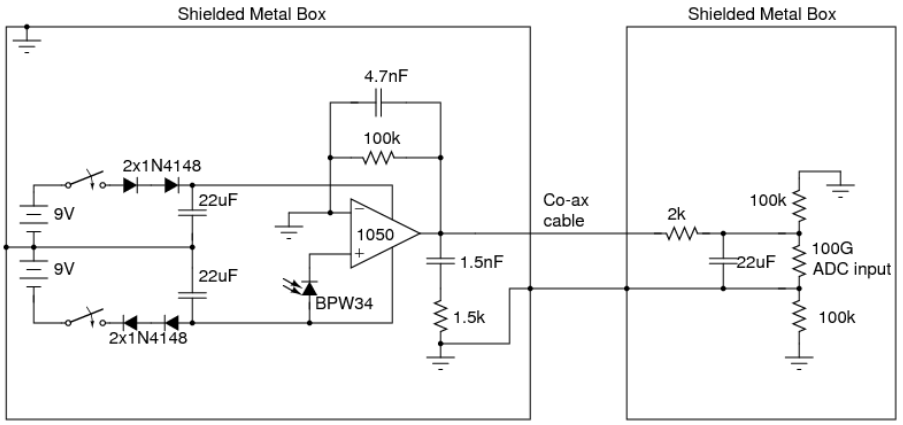

Figure 3.18: Complete photodiode amplifier circuit

The purpose of the dual 1N4148 diodes on the supply rails is to provide a constant voltage drop of about 1.2 V so that the maximum supply voltage (±8 V) of the op-amp is not exceeded. The 22μF supply filtering capacitors are connected off-board with point to point connections.

Initially a LTC1050 precision chopper stabilised op-amp was used. While in theory the best choice, the LTC1050 eventually proved inconvenient to work with due to the limitations of switching transients and difficulty avoiding oscillations that result from this device having a much higher gain at higher frequency than a typical op-amp. These are especially a problem since the feedback capacitor needs to be changed occasionally. For the final experiment, high precision LM308 op-amps were used which have a standard design but have noise specification very similar to the LTC1050 (typically a factor 10 better than standard FET input devices).

The 1.5nF output capacitor blocks any radio frequency interference that may inadvertently be present on the output cable and the 1.5kΩ resistor is necessary to critically damp any oscillations that may result due to the ground loop between the op-amp input terminals.

The low pass filter inside the ADC interface box is required only when operating the apparatus using the direct ratio method. In this case it is mounted very close to the ADC inputs and eliminates any high frequency electromagnetic interference.

When operating the apparatus using the plasma modulation method the feedback capacitor must be changed to a value around 27 pF since we are measuring an AC signal in this case.

All components are standard types except for the 100kΩ feedback resistor. It is fundamentally important that this component be stable as it controls the gain. The component chosen was a NeOhm UPW series ultra precision wirewound resistor. This resistor has a maximum variation of 5 ppm/℃, long term stability of < 50 ppm over 10,000 hours and a maximum thermal EMF of 0.2 μV/℃. Using the assumptions of section 3.4.1 we can give the maximum error due to this resistor as:

$$\Delta I = 5 \text{ ppm} + \frac{50 \text{ ppm}}{10,000} \times 24 + \frac{0.2 \times 10^{-6} \text{ V}}{8 \text{ V}} \times 10^6 \approx \mathbf{5.12 \text{ ppm}} \qquad (3.40)$$

Johnson noise in this resistor is not considered as it will be reduced to a negligible level by averaging due to the feedback capacitor when using the direct ratio method and eliminated by the signal processing when using the plasma modulation method.

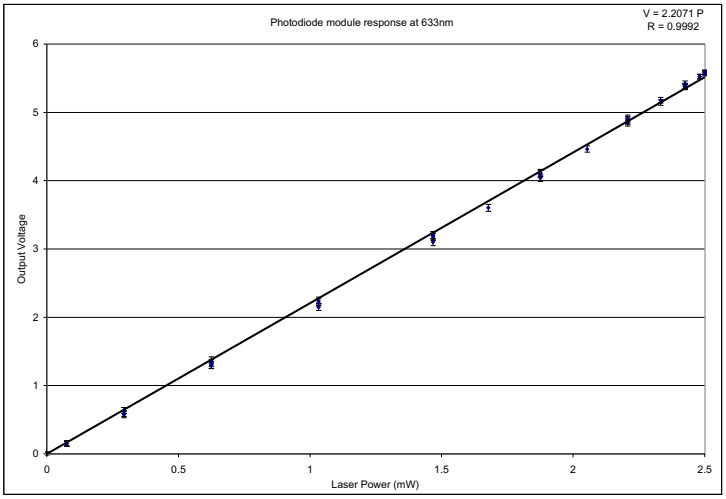

Figure 3.19: Experimentally observed response of the photodiode module detailed in section 3.4.3 measured over a wide range. Laser power calculated from angle of crossed polarisers and a laser of known output power.

PCB design considerations

In order to realise the rated performance of the op-amp it is necessary to minimise any circuit board leakage current.

This can be done by using a high quality fibreglass PCB (printed circuit board) material and encircling the input connections with a *guard ring* operating

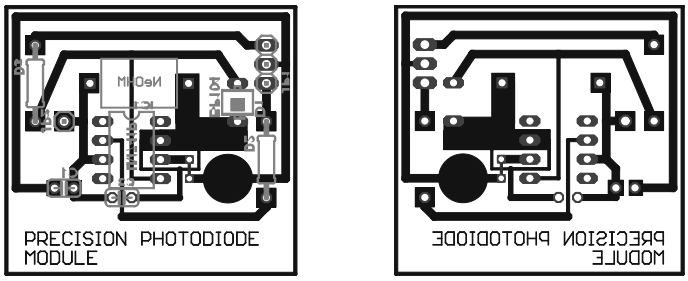

Figure 3.20: PCB overlay pattern and mirrored etching pattern. Shown to scale.

at a potential close to that of the inputs. This guard ring can be clearly seen around pins 2 and 3 in the PCB design shown in figure 3.20.

Thermocouple effects (the Seebeck effect) must also be considered if the low drift of the op-amp is to be fully realised. Any junction between two dissimilar metals is a candidate for generation of thermal EMF. A soldered Copper-Lead/Tin connection typically introduces a thermal EMF of 2μV/℃ [27].

The general approach taken to minimise thermal EMF is to balance the number of junctions connected to each input in order to cancel the thermal EMF. It is also useful to ensure that all components are in close physical proximity and maintained at the same temperature. If the two leads connecting a resistor are at the same temperature then the thermal EMF's will cancel since a resistor has constant reactance across the the whole spectrum of thermal EMF noise.

Unfortunately is was not possible to design the PCB such that all junctions were balanced. If we count the number of junctions between the non inverting input and the point of stable supply (the 22μF capacitors) we find that there are 6 junctions, none of which are mutually balanced. The inverting input has 5 junctions though 2 are mutually balanced as they connect a wire link. Thus the total error following the assumptions of section 3.4.1 and after calibrating to remove the constant EMF at lab temperature is found to be:

$$\Delta I = \frac{(6-3) \times 2\mu\text{V/℃} \times 1\text{℃}}{8\text{V (typical output)}} = \frac{6\mu\text{V}}{8\text{V}} \approx \mathbf{0.75ppm} \tag{3.41}$$

3.4.4 Analog to Digital conversion

Measurement Scheme

The photodiode amplifiers are essentially floating sources. It would be undesirable to reference them to the same ground as the computer and data acquisition system as this may result in ground loops. Following the recommendation of National Instruments [27], it is best to use a differential measurement system in this case.

Under this system the two inputs channels (which are internally connected

to an instrumentation amplifier) are used to make a measurement. Each channel has a negative and a positive lead, none of which is directly connected to the measurement system ground. This system is preferable because it rejects ground loop-induced errors and also electromagnetic interference induced on the signal cables and connectors by the environment.

Care should be taken to ensure that the common-mode voltage level of the signal with respect to the measurement system ground remains within the input range of the measurement device.

It is possible for the instrumentation amplifier input bias currents to move the voltage level of the floating source out of the valid range of the input stage of the data acquisition card. To anchor this voltage level to some reference, *bias resistors* are used. These provide a DC path from the instrumentation amplifier inputs to the instrumentation amplifier ground. They should be of large enough value to allow the source to float with respect to the measurement reference and yet not load the signal source. A value of 100 kΩ was found to work well. These bias resistors are connected between each input lead and the measurement system ground [27].

Quantisation Effects

The data acquisition card used is a National Instruments E series PCI6013. The ADC in this card is capable of 16 bit resolution and has a 0 V — 10 V range. We can set the upper limit on measurement uncertainty due to the measurement resolution as:

$$\Delta I = \frac{10V}{8V \times 2^{16}} \approx \mathbf{19\ ppm} \tag{3.42}$$

However it should be noted that this upper limit is only really valid in the case of a perfectly constant DC source. In reality the signals from the photodiode modules have noise in excess of one least-significant-bit and with time averaging this effectively increases the measurement resolution, a technique normally referred to as *dither*. Essentially, each doubling of the number of measurements n that are averaged adds one bit of resolution by cutting the effective step size in half. The effective increase in resolution is thus $log_2(n)$.

For the 50 kHz sample rate per channel used in this experiments the effective error due to measurement resolution over 1 second is thus:

$$\Delta I = \frac{V_{max}}{V_{sample} \times 2^{16+\frac{ln(n)}{ln(2)}}} \approx \mathbf{3.8 \times 10^{-4}\ ppm} \tag{3.43}$$

3.4.5 Transmitter setup

Radio frequency (RF) excitation is used to energise the discharge in this experiment. RF excitation has always been used in the ring laser project as it

allows capacitive coupling of power into the discharge and does not require any electrodes inside the tube.

The transmitter is an exciter - PA type, it consists of a separate 80 MHz exciter stage followed by a power amplifier stage. In total it can deliver up to 80 W of forward power. The exciter circuit has been modified to allow the amplitude to be modulated by an external voltage. In our case this voltage comes from the analog output of a National Instruments card. Care must be taken to ensure that the line carrying this voltage be well shielded against RF fields. Several ferrite cores and low pass RC filters must be used along this line otherwise oscillation can occur.

As the output impedance of the transmitter (50Ω) differs from that of the plasma, an impedance matching circuit is necessary to ensure that maximum power is delivered to the plasma. Such a circuit must satisfy the following criteria:

1. **The output impedance must be adjustable over a wide range.** The impedance of the plasma is a complicated function of density and distribution of the plasma, itself a function of the power being absorbed by the plasma. The unit must be suitably adjustable to allow good matching for a wide range of gas pressure and absorbed power.

2. The voltage developed across the output when the transmitter is operating at some reasonably high power **must be sufficient to cause breakdown** of the gas in the discharge tube, and thus start the plasma.

3. Where variable capacitors are used for output impedance adjustment, **the potential difference between the capacitor plates must be less than the breakdown voltage of air**.

Because of these complications and a lack of knowledge of actual values for the impedance of a helium-neon plasma, design of an impedance matching unit is difficult. Generally a design known to work is modified on a 'trial-and-error' basis until best matching is obtained.

Figure 3.21 shows the best circuit created to date. The coil has a diameter of 17 mm and is wound with 1 mm wire. The variable capacitors used are adjustable from 10.2 pF to 26.4 pF. When gas pressure is changed it is sometimes necessary to adjust the location of the taps on the coil for best matching. Matching is optimised using a directional RF power meter between the transmitter and matching unit. It is unusual for a 1:1 matching to be obtained.

The electrodes consist of copper wire wrapped around the gain tube. A centre live electrode is used and two grounded electrodes are placed 15 mm on either side of the central electrode. Grounded aluminium foil is wrapped around the out end of the gain tube and provides some RF shielding.

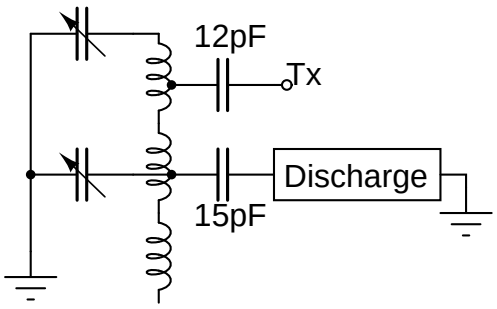

Figure 3.21: Impedance matching circuit

3.5 Measurement procedure and software setup

When either the direct ratio or plasma modulation methods are used we need to carry out a scripted sequence of tasks in order to make a measurements. This is achieved using LabView VIs to do the acquisition and data analysis and using the Lua language (via the LuaView toolkit) to script all the tasks.

Measurement scripts for both the direct ratio and plasma modulation method can be found in appendix A along with all the LabView VIs that are used by these scripts.

3.5.1 Accounting for erroneous signals

Despite every effort to reduce the effects of RF interference on the signals this could not be completely cancelled. Similarly we always observe some background light and some incoherent light from the plasma.

It is necessary to design a measurement sequence that cancels these unwanted effects.

Table 3.1 shows the effects we observe on both photodetectors for all different combinations of shutter and plasma settings. Here all the b variables are background light incident on photodiodes designated by the subscript. Similarly r designates the signals due to RF interference and p the designates signals due to plasma light. L designates laser beam light (unamplified) which must be considered to be different at each time interval (the alphabetic subscripts) due to drift in the probe laser output power. k is a calibration constant which when multiplied by the voltage detected on the second photodiode gives the equivalent voltage on the first photodiode. g is the signal due to laser gain.

The linear system formed by the last two columns of table 3.1 can be solved to give the gain in parts per million:

$$g_{ppm} = 10^6 \times \left(\frac{k(L_{H2}g)}{L_{H1}} - 1 \right) \tag{3.44}$$

	P	S_1	S_2	D_1	D_2
A	0	0	0	b_1	b_2
B	0	0	1	$b_1 + L_{1C}$	b_2
C	0	1	0	$b_1 + L_{1D}$	b_2
D	0	1	1	$b_1 + r_1$	$b_2 + L_{1D}k$
E	1	0	0	$b_1 + r_1$	$b_2 + r_2$
F	1	0	1	$b_1 + r_1$	$b_2 + r_2 + p_2$
G	1	1	0	$b_1 + r_1 + L_{1G}$	$b_2 + r_2$
H	1	1	1	$b_1 + r_1 + L_{1H}$	$b_2 + r_2 + p_2 + (L_{H2}gk)$

Table 3.1: Truth table for the direct ratio method showing measured effects on the photodiodes before (D_1) and after (D_2) the gain tube as a function of plasma (P) excitation state (1 for on, 0 for off) and near S_1 and far S_2 shutters state (1 for open, 0 for closed).

The measurement sequence we choose has the order ADHFE which minimises time spent opening and closing shutters. This procedures is detailed the Lua program in appendix A.

We can go about a similar procedure for the plasma modulation method. This is shown in table 3.2. This method only requires the second photodiode. Background light is not modulated so will not have an effect on the mesurement.

	P	S_1	S_2	D_2
A	0	0	0	
B	0	0	1	r
C	0	1	0	
D	0	1	1	$r + p$
E	1	0	0	
F	1	0	1	r
G	1	1	0	
H	1	1	1	$r + p + g$

Table 3.2: Truth table for the plasma modulation method.

3.5.2 Computing individual signals when using the direct ratio method

After recording the two simultaneous waveforms when using the direct ratio method (one for each of the signal S and reference R detectors, typically 1 second each), there are two approaches that can be used to compute the laser gain.

We can either compute the gain individually from each measurement and average them (equation 3.45) or we can use the average of individual waveforms to compute the gain (equation 3.46).

$$g_1 = \left(\frac{\sum_{i=1}^{n} S}{\sum_{i=1}^{n} R} \right) - 1 \tag{3.45}$$

$$g_2 = \frac{1}{n} \sum_{i=1}^{n} \left(\frac{S_n}{R_n} - 1 \right) \tag{3.46}$$

Due to the inherent linearity of the setup we assume that in the absence of noise $R{=}kS$, from which we can show that mathematically that $g_1 \equiv g_2$.

$$\begin{aligned} \frac{nS}{nkS} - 1 &= \frac{1}{n} \left[n \frac{S}{kS} - n \right] \\ \frac{1}{k} - 1 &= \frac{1}{k} - 1 \\ g_1 &\equiv g_2 \end{aligned} \tag{3.47}$$

Experimentally we find that this is indeed the case if exactly the same data (i.e. from just one ADC channel) is passed in as both R and S. The computed gain is exactly zero. This observation also eliminates any errors introduced by the software.

Experimentally it is found that for a 1 second sample, the noise measured when the signal from one photodiode module is connected to both ADC inputs is 25.7 ppm when determined by 3.45 and 25.8 ppm when determined by 3.46. It should also be noted method 3.45 is preferred as it is much less computationally expensive.

3.5.3 The lock-in amplifier

A software lock-in amplifier is used to make measurements when using the plasma modulation method.

When making any measurement under noisy conditions it is generally a good idea to move the frequency range of measurement well away from that of any noise source. This is essentially the rationale behind the plasma modulation method.

The simplest method of recovering a signal from a modulated source is to simply pass the noisy signal through a narrowband filter centred at the frequency of modulation. This is the method that has been used in earlier work [12].

The lock-in amplifier (also known as the *phase sensitive detector*) takes this approach one step further by making use of the known phase of the modulation.

The basic approach is diagramed in figure 3.22. It consists of four stages:

1. **Input filter:** The input signal is first scaled appropriately and passed through a bandpass filter centred around the frequency of measurement.

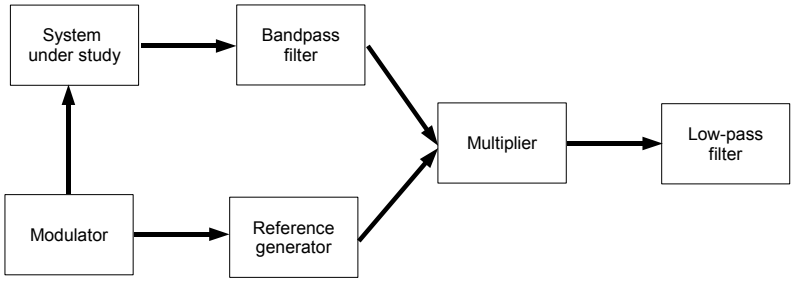

Figure 3.22: Block diagram of the lock-in amplifier

This results in a signal which is relatively free from out-of-band noise and (regardless of the shape of the original modulation waveform) will be essentially sinusoidal.

2. **Reference generator:** This takes the reference signal used to modulate the effect being measured and transforms it to a normalised, zero-mean square wave. If the phase is likely to drift, or if phase information is not available then this stage may also shift the reference phase to correspond with that of the measured signal.

3. **Multiplier:** This stage is also known as the *demodulator*. Here the reference signal and filtered input signal are multiplied resulting in a signal which resembles a half-wave rectified sinusoid.

   When the two waveforms are multiplied the result is a signal with the sum and difference frequencies as the result. Since the filtered input signal and reference signal are of the same frequency the difference frequency is zero and the mean is proportional to the amplitude of the input signal. If the input and reference have a slight phase difference the result will also be proportional to the cosine of the phase difference between the signals. Often the output of this stage can be used to optimise the phase of the reference. The output of this stage will still contain noise which may have peaks much larger than the mean.

4. **Low pass filter:** The resulting signal from the multiplier is passed to this stage. Since the noise components of the input signal are at different frequencies to the reference signal, the sum and difference frequencies will be non zero and will not contribute to the mean level and thus the output of this stage represents only the amplitude of the modulated signal and is free from noise.

In general lock-in amplifiers are able to extract signals from incredibly noisy sources and the output noise is generally independent of the magnitude of noise on the input signal. The noise on the output is constant and arises in the lock-in amplifier. The magnitude of this noise depends on the design.

Lock in amplifiers can be implemented either in hardware or software.

The main disadvantage of a software approach that operates on batches of samples stems from the phase response inherent in digital filters. A signal passed into a digital filter will generally have the same frequency at any point but the amplitude will initially vary before stabilising to a constant. A trade-off must be reached between the number of samples initially thrown away and the desired accuracy of the resulting amplitude measurement. As a result there will inevitably be some noise introduced due to the software lock-in amplifier and this noise will increase as measurement time decreases.

As hardware amplifiers operate continuously phase response is not as much of a concern however designing the necessary low noise circuit is not a trivial task and pre built devices are expensive. In earlier work [12] a high order active bandpass filter was designed, essentially the first part of a lock-in amplifier. The additional noise introduced by just this first stage was already unacceptable.

For the plasma modulation method used in this research a software lock-in amplifier, implemented in LabView was used. This is shown in figure 3.23, the various SubVIs can be found in appendix A. The input filter is a 10^{th} order Bessel filter with a pass band of 20 Hz. The modulation frequency is 210 Hz. It is desirable to chose as high a frequency as possible (i.e. as fast as the transmitter can be amplitude modulated, which is not very fast since it is designed to be a FM transmitter) in order that the signal passed by the bandpass filter stabilises as quickly as possible. It is also desirable to choose a frequency well away from any noise source.

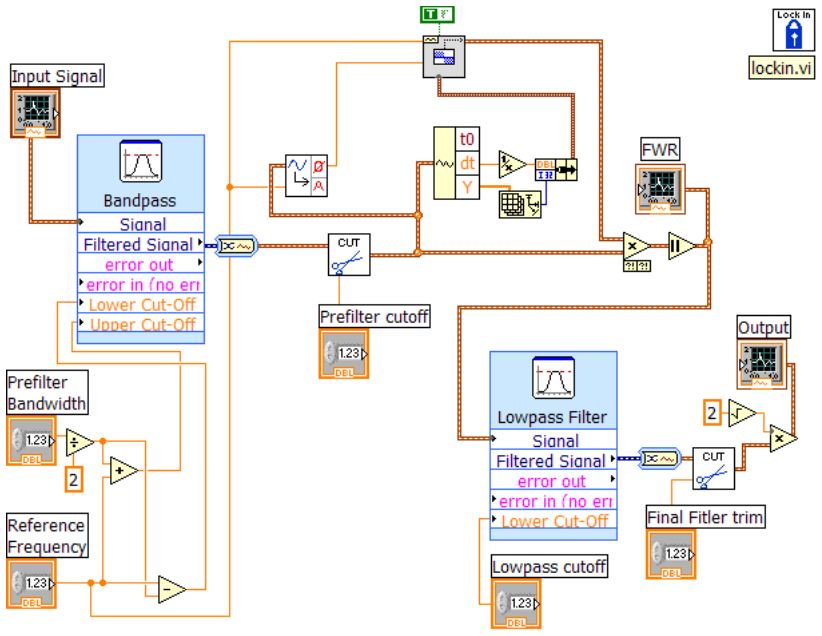

Figure 3.23: Lock in amplifier implemented in LabView.

While every attempt was made to synchronise the phase of the modulation

with the acquisition timing this proved insufficient so it was necessary to recover the phase from the original signal. Since we are operating on a block of data this reasonably straightforward. Equation 3.48 recovers the phase angle ϕ from a time series $y(t)$ of known angular frequency ω. While relatively computationally expensive this gives a much better estimate of phase than the built in LabView function.

$$\phi = \tan^{-1} \frac{y(t)\sin(\omega t)}{y(t)\cos(\omega t)} \tag{3.48}$$

3.6 Error analysis for the direct ratio method

The following table summarises all of the theoretically calculated sources of error in the previous sections. From this it can be seen that the total error for the experiment should be at most 6.00 ppm.

The ratio error Δg is computed from the noise of the individual channel noise according to equation 3.49. In some cases taking a ratio eliminates the error. In all other cases the increase in error due to ratioing the two measurements is below the accuracy of the error.

$$\Delta g = \frac{1}{2}\left(\frac{I_0 + \Delta I}{I_0 - \Delta I} - 1\right) = \frac{V + V\Delta I}{2(V - V\Delta I)} - \frac{1}{2} = -\frac{\Delta I}{\Delta I - 1} \tag{3.49}$$

Error Source	Magnitude (ppm)	Ratio Error (ppm)
Optics vibration	7.1×10^{-7}	0
Photon counting	3.3×10^{-7}	3.3×10^{-7}
Photodiodes $\Delta I/\Delta\lambda$	4.34	0
Op-amp noise	0.13	0.13
TIA Circuit noise	5.12	5.12
Seebeck voltage noise	0.75	0.75
ADC Quantisation error	3.8×10^{-4}	3.8×10^{-4}
TOTAL	**10.34**	**6.00**

When using the direct ratio method, the observed errors are much higher than predicted. An error of 500 ppm was found to be typical.

In order to identify the source of error we can isolate sections of the hardware and measure the uncertainty in the resulting laser gain measurement with the discharge off. In section 3.5 we have eliminated any systematic error in the software and found the uncertainty due to the ADC process to be 24.7 ppm.

We can also measure the uncertainty due to the trans-impedance amplifier by temporally modifying the photodiode modules by bridging the photodiodes with a 150 kΩ resistor under dark conditions to provide a constant reference current sufficient to give a 6 V output.

We can measure the uncertainty for all hardware up to the photodiodes by

using two identical high brightness LEDs (connected in series so that each LED has equal current) incident on the photodiodes under dark conditions.

The following table summarises the experimentally measured uncertainties compared to what has been theoretically predicted.

Error Source	Experimental (ppm)	Theoretical (ppm)
Software	0	0
ADC	24.7	3.8×10^{-4}
TIA circuit	≈ 10	5.883
Photodiodes	< 1	0
Optics + other	≈ 464	0
TOTAL	$\approx$ **500**	**5.883**

Unfortunately the unknown source of error was not specifically identified. This was the main motivation for switching to the plasma modulation method, despite its shortcomings.

The plasma modulation method was used for all measurements of gain that have been reported in chapter 4.

3.7 Measuring plasma power

For experimentally observed radial gain profiles to be of any real use for modelling the gain distribution or of use to others with lasers that employ a different arrangement for excitation it is clearly necessary to be able to report the true power being absorbed by the plasma.

Using a RF power meter capable of measuring forward and reverse power, it is possible to measure the output power of the transmitter, however how much of this power is actually coupled into the plasma compared with how much is transmitted around the surrounding region is very difficult to ascertain. It certainly depends on electrode geometry and plasma impedance, which in turn is likely to vary with plasma parameters such as pressure and gas mix, and dynamically with absorbed power.

A simpler way of determining the plasma power is to measure the power of the incoherent light from the plasma. This can be done simply using the existing photodiodes used to measure laser gain. The difficulty is in making an absolute measurement. Since we know the output of the spectral sensitivity of the photodiode used and the geometry of the setup it is possible to calculate the plasma power.

This is a relatively involved process as the spectral response of the diode and source must be taken into account. As a check of the validity of this measurement a high intensity LED (which has known absolute output and spectral distribution) was used. This also allows us to discover which photodiode we were supplied with as spectral response of BPW34 photodiodes manufactured by Vishay Siemens/Osram differ. Figure 3.24 shows these curves together.

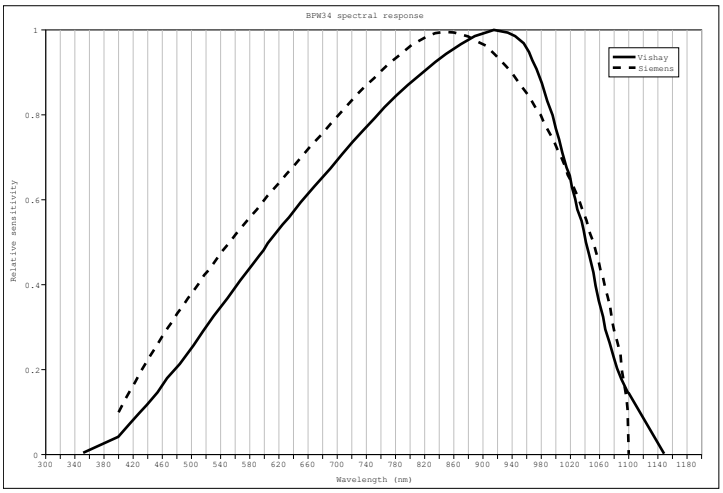

Figure 3.24: Spectral response of the BPW34 photodiodes from different manufacturers

3.7.1 Method validity check

A high intensity LED, the Luxeon MD1C Red LED from Lumenids was chosen for this purpose. It has a physical diameter of 5mm and thus when placed at a similar distance from the lens and photodiode as the plasma so that a similar geometry can be emulated. The radiation pattern of the LED is shown in figure 3.25 — it is interesting to note that given the small angular diameter subtended by the lens if the lens-LED distance is reasonably large then there is essentially no change in light intensity with angle and thus the LED is effectively an isotropic radiator. This property also reduces the requirement for accurate alignment. Similarly the angular sensitivity of the BPW34 photodiode (figure 3.26) exhibits essentially no deviation in sensitivity over small angles.

Firstly we need to calculate the absolute light output of the LED in radiometric units. The LED luminous flux L is given in Lumen. The Lumen is defined as the candela steradian, so the total LED luminous intensity (in candela) I_t is:

$$I_t = I_r(0)\frac{L}{s} \tag{3.50}$$

Where I_r is the relative intensity as a function of angle (figure 3.25). Since the angle subtended by the lens is small and the relative intensity essentially constant for small angles displaced from zero for both the LED (figure 3.25) and photodiode (figure 3.26) it is sufficient to evaluate the relative output at zero. Here s is the solid angle over which light from the LED falls and is given by equation 3.51. We define the beam angle[1] as θ_b.

$$s = 2\pi \int_0^{\theta_b} I_r(\theta)\sin(\theta)d\theta \tag{3.51}$$

[1] Angle over which more than 99% of the light output falls

The necessary luminous flux intercepted by the lens (of diameter r_l at a distance from the LED of d) is then simply:

$$L_i = I_t \frac{\pi r_l^2}{d^2} \tag{3.52}$$

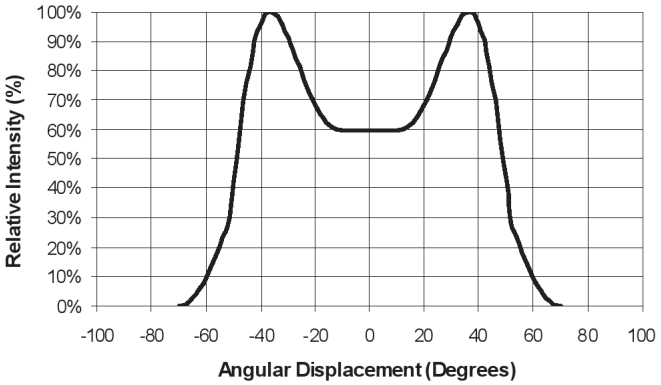

Figure 3.25: Radiation pattern of the Luxeon MD1C LED

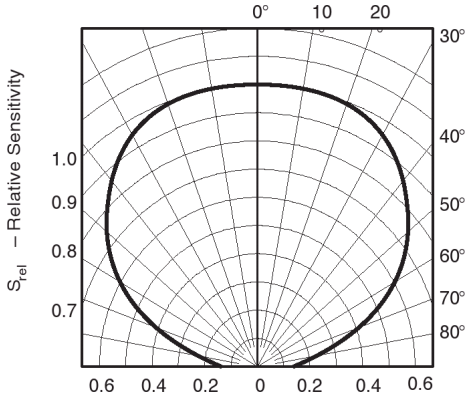

Figure 3.26: Angular sensitive of the BPW34 photodiode

The candela is a unit of luminous intensity normalised to the *standard luminosity function*, which emulates the spectral responsivity of the human eye, as determined by the CIE1931 response curves $\overline{y}(\lambda)$. By definition the luminous intensity in candela $I_v = 683.002 \int_0^\infty I(\lambda)\overline{y}(\lambda)d\lambda$ where λ is wavelength in nm and $I(\lambda)$ is the intensity of the source in watts per nm. As we only know the relative spectral output of the LED we define w to be the maximum intensity of the source in watts with respect to wavelength.

$$w = \frac{I_t \pi r_l^2}{683.002 \int_0^\infty I_r(\lambda)\overline{y}(\lambda)d\lambda} \tag{3.53}$$

The total power p_t received by the lens is now simply:

$$p_t = w \int_0^\infty I_r(\lambda) d\lambda \tag{3.54}$$

However this will not be the power observed by the photodiode as it has its own spectral response which must be taken into account. This is shown in figure 3.15 and denoted $r_{pd}(\lambda)$. The power observed by the photodiode, denoted p_{pd} is thus:

$$p_{pd} = w \int_0^\infty r_{pd}(\lambda) I_r(\lambda) d\lambda \tag{3.55}$$

The python program shown in listing B.3 performs this calculation. This program requires the module `DataInt` which was written for this research to facilitate integration of curves from irregularly spaced data. The source code for this module is available in appendix B. The photodiode spectral response curves and LED and photodiode temperature sensitivity data was extracted from the devices respective data sheets using the GNU G4Data program.

An example output is shown below:

```
Total solid angle = 2.01754334733 Sr
Candela total = 6.63785808195 Cd
Lumens on photodiode = 0.000963942010853 lm
Peak power on photodiode = 1.46438898288e-05 W
Effective power=1.61834773393e-06 W
Voltage = 101.053019308 mV
```

Four separate LEDs were used in the calibration experiment, each mounted on a rotating stand at a distance of 1765mm from the lens and carefully aligned to be directly facing the photodiode. The spectral output of each LED was measured using an Ocean Optics USB2000 CCD spectrometer. The relative transmission of the lens was measured using a laser beam and a general purpose large area photodiode. A thermocouple was attached to the heatsink of each LED and the temperature noted. The photodiode was assumed to be at thermal equilibrium with the laboratory, the temperature of which was also noted.

Table 3.3 shows the measured photodiode signal for each of the four diodes and the predicted output as computed with the program shown in listing B.3 using photodiode spectral response curves from Siemens and Vishay.

The manufacturer of the LEDs gives a typical output of 27 Lumen with an uncertainty of 10% and a minimum possible output of 13.9 Lumen. Since all the LEDs (with the possible exception of LED 1) have very similar measured output (within 2%) we assume that these represent the typical output. We can conclude that the LEDs have an output that is typically 35% brighter than the advertised typical output. We can also conclude that the photodiodes used have spectral response characteristics most similar to those manufactured by

Siemens and that the method of determining absolute plasma power using the photodiode output, response curves and spectra of the source is valid.

3.7.2 Calculating total plasma light

Using spectra taken of the plasma light we can now procede to calculate the total power radiated by the plasma given the measured photodiode output.

The light output of the plasma tube is highly anisotropic so we first need a method of calculating the fraction of light received by the photodiode compared with the total visable light emitted by the discharge. We assume that the plasma is optically thin (i.e no re-absorption takes place, a valid assumption given the very low pressure). Because the photodiode is 'looking' down the longest axis of the discharge we expect the light received to be significantly greater than would be expected from an isotropic radiator.

Although the gain tube is not a point source, we can represent it by infinitely many point sources arranged over the volume of the plasma. The first problem is to find the light received by the photodiode by each of these point sources as a function of position of the point source.

To solve this problem we begin by noting that due to symmetry we can solve the analogous 2-dimensional problem. This is depicted in figure 3.27. The nearest set of black lines to the origin represent the edges of the 5mm aperture (this is placed directly before the beam shutter) and the furthest pair of black lines represents the edges of the lens in front of the photodiode which is the collecting area of the photodiode.

Referring to figure 3.27 we see that the photodiode acceptance angle a is simply $\widehat{ASD}$. If the vertical position of the point source is y then using simple trigonometry we find $\widehat{ASD}$:

$$\widehat{ASD} = \tan^{-1}\left(\frac{|R2 - y|}{D2}\right) - \tan^{-1}\left(\frac{|R1 + y|}{D1}\right) \tag{3.56}$$

So the fraction of intercepted light from the point source is simply $\widehat{ASD}/2\pi$. By symmetry we see that the intercepted fraction for a point source with negative vertical position is the same as the equivalent positive position. A python function to calculate this is shown in listing 3.1.

LED	**Measured**	**Predicted** (Siemens)	**Error**	**Predicted** (Vishay)	**Error**
1	176 mV	121.0 mV	31%	101 mV	42.5%
2	138 mV	99.8 mV	27.7%	82 mV	40.6%
3	139 mV	56.7 mV	59.2%	45.7 mV	67.1%
4	135 mV	63.8 mV	52.7%	51.4 mV	61.9%

Table 3.3: LED calibration data

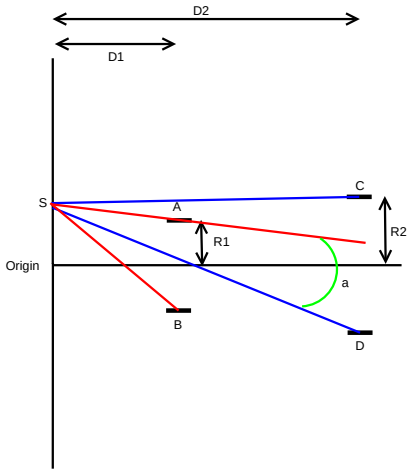

Figure 3.27: Geometry of rays intercepted from a point source.

Listing 3.1: Fraction of light intercepted from a point source

```
1  def pointsource(x,y):
2    D1=1172.5 #Distance to aperture
3    R1=2.5    #Radius of aperature
4    D2=2937.5 #Distance to lens
5    R2=12     #Radius of lens
6
7    D1=D1+x
8    D2=D2+x
9    y=abs(y)
10   ASD = atan(abs(R2-y)/D2) - atan(abs(R1+y)/D1)
11   if (ASD<0): return 0
12   return ASD/(2*pi)
```

When plotted (figure 3.28) this shows a maximum along the centre of the gain tube decreasing linearly as the radial position is increased to 1.64 mm, after which no light is intercepted by the photodiode. We note from this that it is important to use the plasma light measurement only when the gain tube is centred for measuring plasma power.

Now by computer iteration over the area of the plasma we can find the fraction of power intercepted. The gain tube consists of a narrow central section, in which the majority of the plasma is contained as well as wider end sections which are filled with plasma when operating at high power. We assume that the intensity of the plasma is uniform across these regions. The region of plasma is measured by a simple ruler measurement. If we consider figure 3.29 we see that this is a reasonably good assumption. For most accurate measurement a plot such as shown in figure 3.29 would be used to weight each individual point source.

A python function to carry out this integration is shown in listing B.5. A typical output from this program shows that around 0.015% of the light gener-

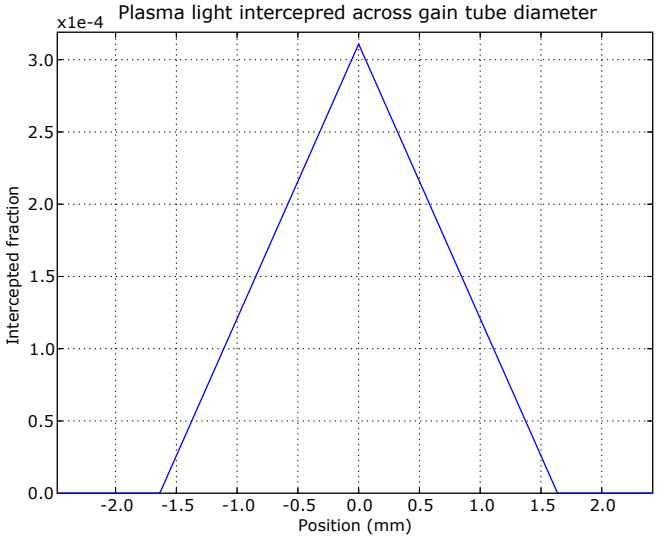

Figure 3.28

ated by the discharge is intercepted by the photodiode.

Lastly we need to solve the familiar problem of determining the effective power received by the photodiode using the spectrum of the emitter and spectral response of the photodiode. This is done in the same way as was shown in section 3.7. A typical value of the relative responsivity is 1×10^{-2}.

To calculate the total power output of the plasma P_{total} we simply multiply the observed power, relative responsivity and intercepted fraction. In this example a 15:1 helium-neon plasma at a pressure of 2.253 Torr was used with a 7.5 mm gain tube. The RF power, photodiode output and plasma geometry were measured for several RF power settings. This is shown in figure 3.30. We see that the response is linear and from the gradient of the trendline find the efficiency of turning RF energy into visable light to be 0.38%. It is interesting to compare this with the laser power observed by Andrews and King [2]. From figure 2.16 we can find efficiencies for this process between 0.03% and 0.15%.

From the point of view of developing a physical theory it is more useful to express this power in terms of photon energy per atom. Using the measurements of the plasma geometry and the perfect gas law we can write the optical power output per atom P_{at} as given in equation 3.57. Here l_c and l_e are the lengths of the plasma in the central region and each tube end respectively. r_c and r_e the radii of the central and end regions of the gain tube respectively. R is the gas constant, p the fill pressure and T is the gas temperature during filling, i.e. room temperature. N_A is Avogadro's number.

$$P_{at} = \frac{P_{total} RT}{N_A p \pi (r_c^2 l_c + r_e^2 l_e)} \tag{3.57}$$

Figure 3.31 shows a plot of this (made using the same data as in figure 3.30). The parameters of the best fit line are shown in equation 3.58. We see that a typical value of the optical power output per atom is of the order 10^{-4} eV atom^{-1} sec^{-1}. We also note that the curve is non-linear — while the total power output of the discharge increases with input power the discharge also grows in volume. This process appears to limit the optical power output of each atom, and thus presumably the laser power due to the finite length of the narrow region of the gain tube, where the majority of the gain takes place.

$$P_{at} = 4.66 \times 10^{-5} \log(P_{RF}) + 3.31 \times 10^{-5} \tag{3.58}$$

Another useful parameter is the gas temperature. Silfvast [33] quotes a typical gas temperature of 500 K. We expect the gas temperature to rise with RF power. The gas temperature is an important parameter as it comes in to the gain curve calculations due to Doppler broadening.

We can measure the temperature T by measuring the change in pressure dp when the plasma is switched on. We assume that the temperature increases only in the region of plasma, the volume of which is denoted V_p. The total volume of the system is denoted V. Using the perfect gas law we find the change in temperature:

$$\begin{aligned} dT &= dp \left(\frac{VT_0}{nR}\right)\left(\frac{V}{V_p}\right) \\ &= dp \frac{V^2 T_0}{nRV_p} \\ &= dp \frac{VT_0}{p_0 V_p} \\ &= dp \frac{VT_0}{p_0 \pi (r_c^2 l_c + r_e^2 l_e)} \end{aligned} \tag{3.59}$$

$$\begin{aligned} T &= T_0 + dT \\ &= T_0 + dp \frac{VT_0}{p_0 \pi (r_c^2 l_c + r_e^2 l_e)} \end{aligned} \tag{3.60}$$

Figure 3.32 shows a plot of the temperature measured using this method against RF power. The discharge conditions are the same as used earlier in this section. The fitted line is a logarithmic function with parameters shown in equation 3.61. Figure 3.33 shows the same temperature data but plotted against mean atomic optical power output using the curve shown in figure 3.31 as a reference. Note that we recover a linear relationship, as expected. The gradient of the fitted line is 3.43 $\times 10^6$ K sec eV^{-1} atom^{-1} and the intercept is 9.09 K which is close to the expected 0 K.

$$T = 160.1 \log(P_{RF}) + 123.6 \tag{3.61}$$

3.8 Spectroscopic measurements

Measurements of the discharge spectra can be made very easily using a Ocean Optics USB 2000 CCD spectrometer. This device has an optical fibre input which can simply be placed nearby the discharge. The spectra is then recorded by computer over a range of 300-1200 nm to a resolution of 0.3 nm.

Figure 3.34 shows an example spectra taken of the gas in the UG2 laser. Note the relative complexity of the spectra with very many spectral lines. The Matlab program *FindPeaks v1.3* by Tom O'Haver was found to be useful for extracting the peak heights and wavelengths for later analysis.

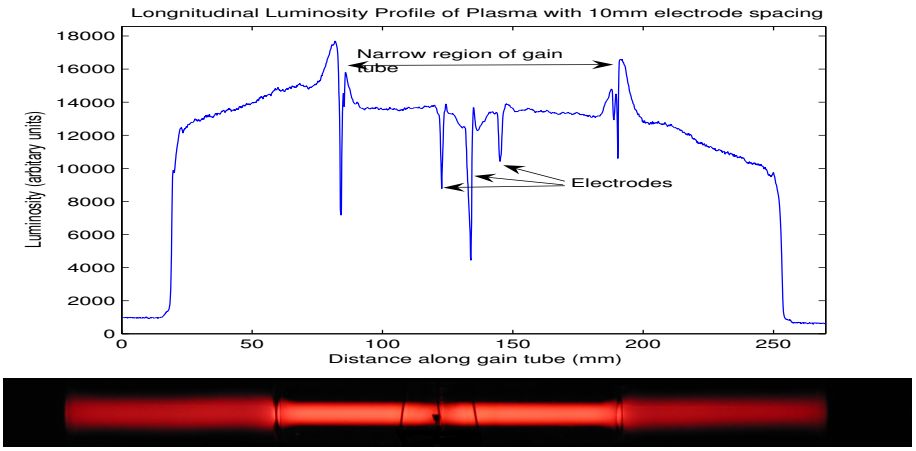

Figure 3.29: Photograph of longitudinal distribution of plasma intensity when running at high power shown with a plot of plasma intensity, as measured from the photograph. Earlier work [12]

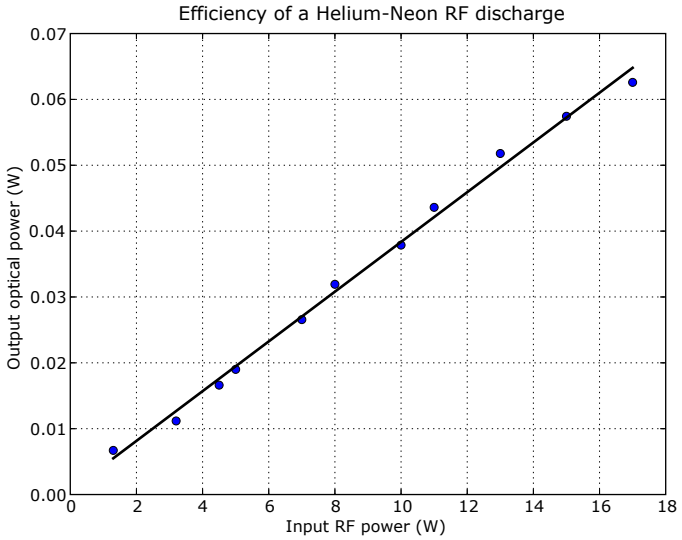

Figure 3.30

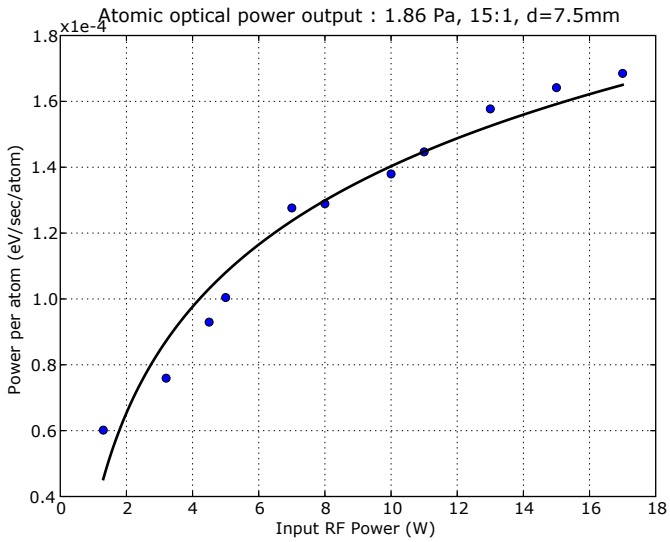

Figure 3.31

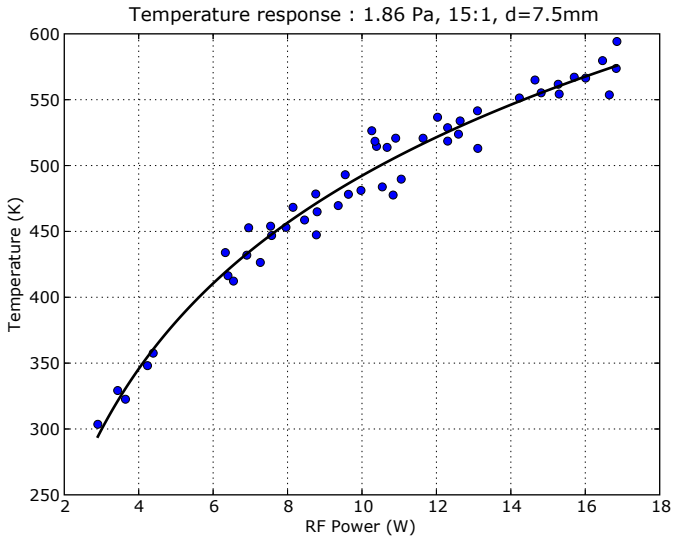

Figure 3.32

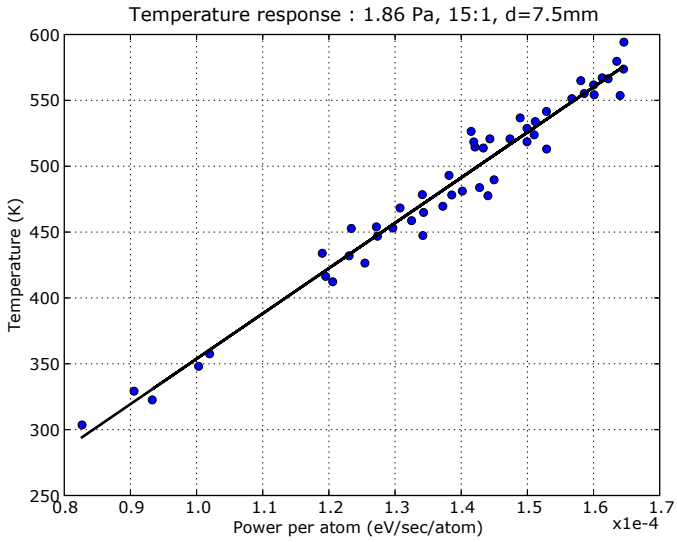

Figure 3.33

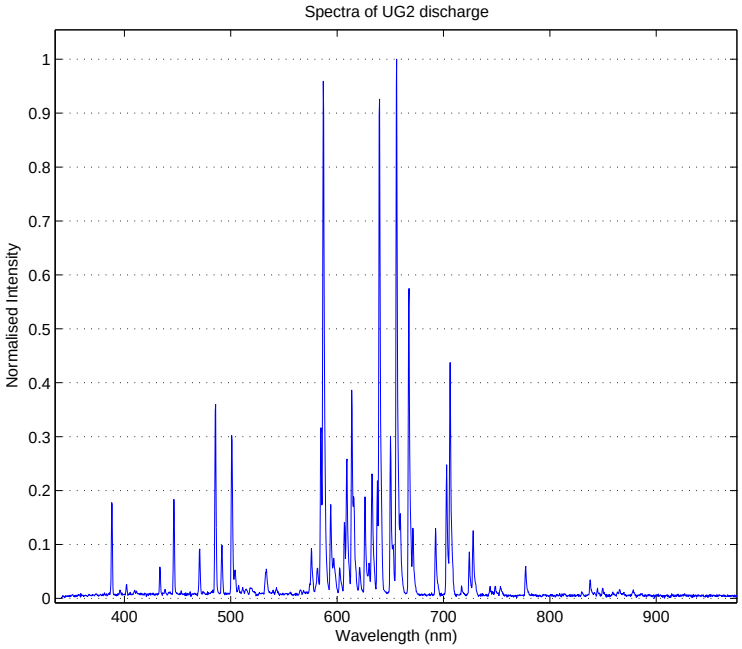

Figure 3.34: Spectra from UG2 discharge.

Chapter 4

Results and Analysis

4.1 Fitting a high resolution profile

When comparing theoretical models of gain distribution to experiment it is necessary to obtain data with high radial resolution and gain resolution. For this purpose a sets of 40 measurements were taken at 160 points across the diameter of an 8 mm gain tube (50 μm resolution) over a period of 21 hours. A power level was chosen so that the resulting curve exhibited both the beginnings of a central reduction in gain and general Bessel shape. A gas mix was chosen to give high gain and thus smaller fractional uncertainty. The raw data for this is shown in figure 4.1.

As can be seen this data contains occasional outliers (around 5% of measurements, probably caused by plasma instability). For curve fitting these outliers (which were identified as the points in each set of measurements more than two standard deviations from the mean) were removed. Remaining measurements were averaged and an uncertainty calculated from the standard deviation / $\sqrt{\mathrm{N}}$. The average gain uncertainty was just **8 parts per million**. The asymmetry in the measurements is probably due to plasma composition changes or transmitter power drift over the duration of the measurement.

Figure 4.2 shows a portion of this data (black). Least-squares fits of the data to a modified version of the McLeod function (red), a 0^{th} order Bessel function (blue) and (for comparison) a simple cubic (green) are shown. It was necessary to restrict the fitting to the central 6 mm of the tube in order for the McLeod function to converge. This is due to a sharp increase in gain that was observed near the tube walls.

When using the original McLeod function (equation 2.6) either directly with all of the parameters free, or with the parameter $c_6 = 5.1 \times 10^{-8}$ s the fit could not be made to converge. A simple modification was made — a constant offset parameter was included and this allowed the fit to converge. The modified McLeod equation takes the following form:

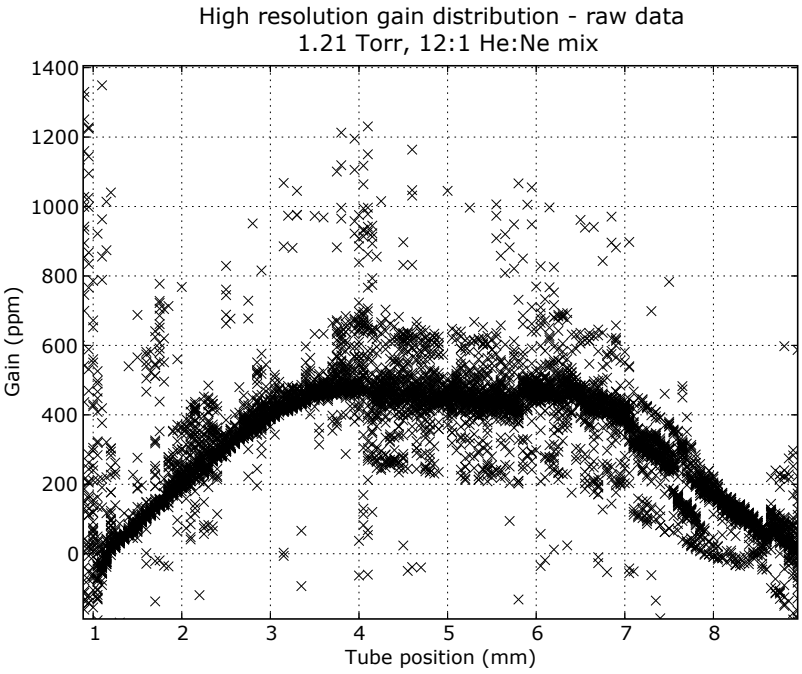

Figure 4.1: High resolution gain profile raw data.

$$N_{inv} = \left[\frac{c_1}{c_2 + c_3/J_0(\rho)} - \frac{c_4}{c_5 + c_3/J_0(\rho)}\right] c_6 J_0(\rho) + c_7 \tag{4.1}$$

The numerical values for the fitted parameters are shown below. Note that these are not directly comparable to those presented in equation 2.7 since the units are fractional laser gain rather than an arbitrary 'population inversion density' used by McLeod.

$$\begin{aligned} c_1 &= -415.3 \\ c_2 &= -462.0 \\ c_3 &= 744.9 \\ c_4 &= -16151 \\ c_5 &= 5498 \\ c_6 &= 2158 \\ c_7 &= 203.38 \end{aligned} \tag{4.2}$$

The average errors between the data and fitted curves shown in figure 4.2 is shown in table 4.1.

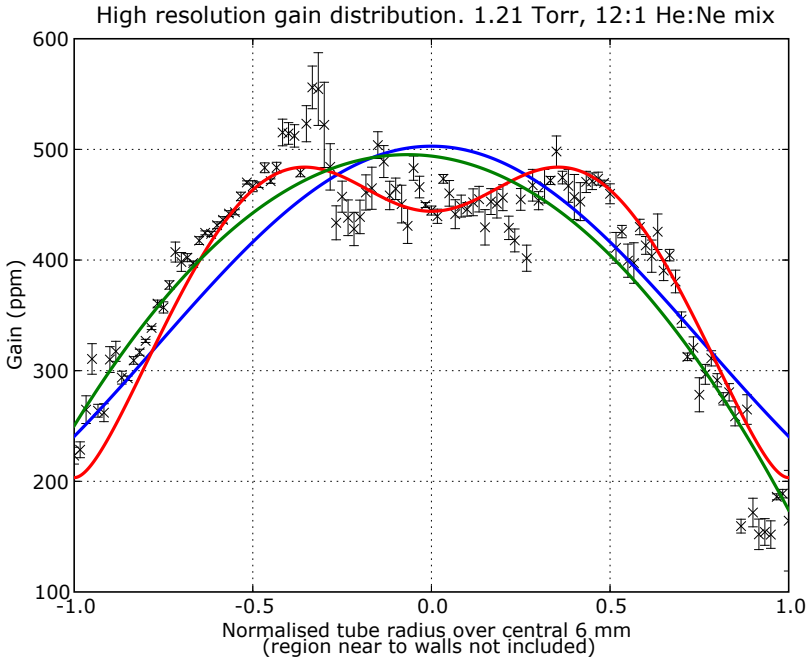

Figure 4.2: High resolution gain profile fitted with offset-McLeod (red), Bessel (blue) and cubic (green) functions.

Function	Mean error (ppm)
Bessel	39.2
McLeod (offset)	27.4
Cubic	30.5

Table 4.1: Errors for fitted functions. The modified McLeod function provides the best fit to the data.

4.2 Gain near the tube edges

In order to further investigate the observed increase in gain near the tube walls a series of measurements were made at a radial resolution of just 20 μm. The same gas fill and power level was used as in section 4.1.

Figure 4.3 shows this data, which has been processed in the same way as in section 4.1. Note how the uncertainty increases with measurements nearer to the tube wall. In these measurement the majority of the probe laser beam is being clipped by the gain tube wall. As a result the light intensity measured during the calibration procedure is very sensitive to vibration of the apparatus, increasing the overall uncertainty.

The results show a remarkable increase in gain. The gain increases toward the tube edges and then appears to decrease slightly just beyond the minimum

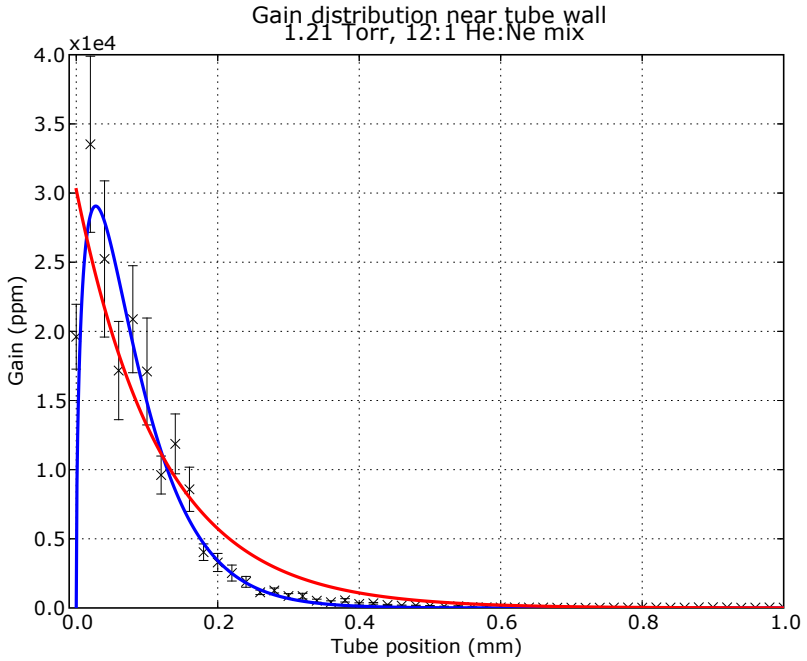

Figure 4.3: High resolution gain profile measured near to the tube wall. The blue line is a fit to an equation of the form $k_1 \exp(-k_2 x)\sqrt{x}$. The red fitted line takes the form $k_1 \exp(-k_2 x)$.

Function	Mean error (ppm)
$k_1 \exp(-k_2 x)\sqrt{x}$	352.4
$k_1 \exp(-k_2 x)$	556.7

Table 4.2: Errors for fitted functions modelling the increase in gain near the tube wall.

measurement resolution. At maximum the gain is 60 times greater than the maximum gain in the central region of the tube.

An increase in gain near the tube walls is consistant with the description of the laser process described in section 2.2 due to the sheath of ions that develops to balance the build up of electrons in the tube wall. We now refer to the work of Schuöcker *et al.* [30] who described the ion-sheath when investigating very narrow capillary gain tubes in helium-neon waveguide lasers.

A plot of their theoretically calculated dependence of output intensity on tube radius is shown in figure 4.4. Unfortunately the analytical form of the plotted function is not readily attainable as it appears to be the result of numerically solving a system of differential equations. However without appealing to any of the physics involved we note the close resemblance of this plot to the function $y = k_1 \exp(-k_2 x)\sqrt{x}$ where k_1 and k_2 are arbitrary constants, x the distance from the wall and y the laser power. This function has been fitted

to the experimental measurements in figure 4.3. The fit was found to be very accurate, significantly more so than a reference exponential fit as shown in table 4.2.

The parameters k_1 and k_2 were found to be 2.88 $\times 10^5$ and 18.1 respectively.

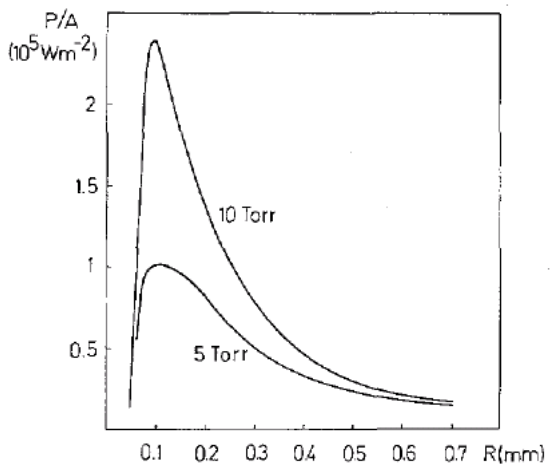

Figure 4.4: Calculated dependence of output intensity on tube radius for small diameter helium-neon waveguide lasers as a function of tube radius [30].

4.3 Electrode geometry

Experiments thus far have used a live electrode one half the distance along the length of the gain tube with two grounded electrodes spaced 15 mm on either side. The remainder of the tube was wrapped in aluminium foil and grounded.

At low power this arrangement results in two distinct lobes of plasma forming on either side of the live electrode.

We presently have no good way of determining the optimal electrode arrangement. An experiment was undertaken to test if different electrode geometries can change the gain distribution. Of particular interest are asymmetric geometries. If such geometries can introduce an asymmetry to the gain profile then the transverse mode behaviour and multimode threshold may be affected.

Figure 4.5 shows a gain profile measured with exactly the same gas fill and power level as the high resolution profile measured in figure 4.2. The only difference between the profiles is that the central live electrode was displaced approximately 5 mm toward one of the grounded electrodes. This results in a dramatic decrease in gain though the gain profile remains symmetrical. The cause of the decrease in gain is probably not the asymmetry as such but rather the result of a higher power density causing a decrease in gain through a pronounced central dip. When the power level was reduced a more usual profile showing positive gain was restored.

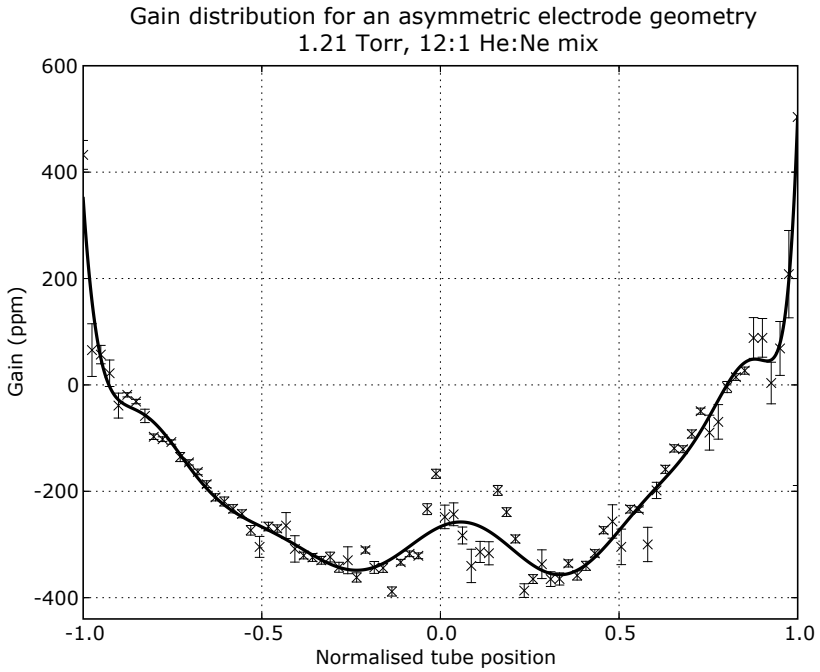

Figure 4.5: Gain profile with an asymmetric electrode arrangement. The trend-line is a 15^{th} order polynomial.

4.4 Gas contamination

In the UG2 laser we observe an increase in gas pressure of 0.02 mbar over a period of 8 weeks. Over this time the gain decreases by an estimator factor of $\sim$2 until it drops below 800 ppm (at the maximum available RF power) after which lasing can no longer be maintained.

Hochuli *et al.* [43] have studied the effects of various contaminants on laser power. A plot of the effect of hydrogen, oxygen and water on laser power is shown in figure 4.6.

4.4.1 Possible contaminants

1. **Hydrogen** is considered the most likely contaminant. Hydrogen arises from outgassing from stainless steel. Typical outgassing rates for stainless steel are of the order $260 \times 10^{-10} Ls^{-1}cm^{-2}$ [16]. With a surface area of 40 m^3 and volume of 980 L the increase in pressure of 0.01 mbar / month is entirely consistant with outgassing. Furthermore this is supported by indirect evidence from G ring laser. The tubes of G were recently replaced with a low outgassing stainless steel and as a result laser lifetime and stability has shown a marked improvement.

2. **Oxygen** In an experiment conducted by King [20], oxygen was concluded

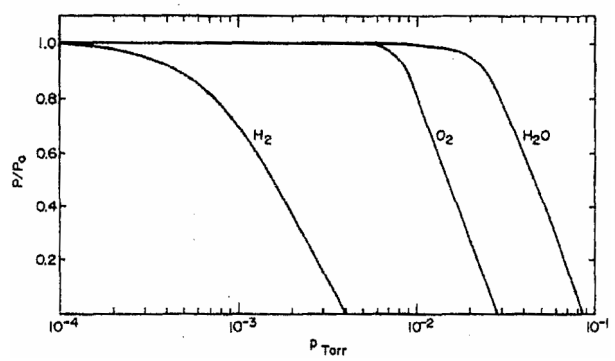

Figure 4.6: Decrease in laser power due to various contaminants

to be the contaminant responsible for the decrease in laser power over time. Experimental measurements were made using a mass spectrometer and oxygen detected though no absolute concentration was given.

The mechanism by which oxygen accumulates in the discharge has been investigated by Martinez [24]. It is stated that the energy lost by a Neon atom in the lower laser level is more than twice that required to break the Si-O bond in the fused silica which forms the gain tube. This results in a release of ionic oxygen and the formation of a brown layer of a reduced form of silica. King observed this layer in the gain tube of the C1 ring laser. This has not been observed on any other ring lasers.

It should be noted that the RF power levels used by Martinez were of the order 250 W whereas C1 and also later lasers use a power level of the order of a few watts.

3. **Air** is an obvious possible candidate for contamination by a slow leak to the atmosphere.

4. **Water** is also a possible candidate for contamination especially when operating and constructing the laser in a damp environment. Water can be removed by baking the tubes while pumping. We would expect water to be broken into hydrogen and oxygen in the discharge.

4.4.2 Spectral analysis

A spectrum of the discharge from the UG2 ring laser was taken after the laser had been operating for 77 days, over which time a partial pressure of 0.025 mbar contaminant had accumulated. The discharge was operating at 10 W of RF power and the spectra was taken in the central narrow region of the gain tube. The initial fill was to a total pressure of 3 mbar with helium-neon mix ratio of 15:1 and natural neon used.

Table 4.4.2 shows the result of the analysis method detailed in section 3.8. The **Line** column shows the measured wavelength of the spectral line (nm) and **Mes.Int** shows the measured spectral line intensity in units normalised between 0 and 1. The **Atom** column shows the atomic species which was identified as the source of the spectral line and the **Transition** column shows the respective transition. Rel.Int is the relative intensity of the spectral line as found in the NIST atomic spectra database[1].

The relative intensities figures are dependent on the excitation mechanism and are really only intended as guidelines for low density sources. We can however use these figures to estimate the relative concentration of atoms with the specified emission line by simply $\frac{\text{Mes.Int}}{\text{Rel.Int}}$.

By summing these estimates of quantity for each species and expressing this as a fraction of all species it is possible to make an estimate of absolute quantities. This is valid only when we can assume a consistant excitation mechanism for the species we are comparing. This is obviously not the case for the helium and neon.

If we assume that the hydrogen, oxygen and nitrogen all have a consistant excitation mechanism then we can determine the makeup of the contaminant. This is shown in table 4.4.

What is remarkable about this is that the ratio of Nitrogen to Oxygen is 77:23, very close to that of air which is 78.8:21.2.

We can thus conclude that the contamination is composed almost entirely of hydrogen as a result of outgassing from the stainless steel tubes. Oxygen is also one of the contaminants but this comes entirely from air and not from breakdown of the gain tube walls by the discharge. The air is most likely the result of a small leak.

Given the volume of UG2 of 980 L and gas lifetime of 77 days this represents a leak with a flow rate of 2.46×10^{-5} cm^3 s^{-1}. This is within the range of our leak detector so if the air is the result of a leak it should be possible to detect it with the leak detector. Alternatively the source of air may be somehow internal to the cavity.

4.4.3 Effect of hydrogen

As we now know that the primary source of contamination is hydrogen, it is interesting to see what effect this has on the gain medium.

Gain profile

Figures 4.7, 4.8 and 4.9 show radial gain profiles measured for a gas mix with 1% hydrogen introduced compared with the same mix without hydrogen. Each figure represents a different transmitter output power. Output power was the

[1] http://physics.nist.gov/PhysRefData/ASD/index.html

Line	Mes.Int	Atom	Rel.Int	Transition
388.19	0.15484	Ne	20	2s2.2p5.2P$^{1/2}$.3s - 2s2.2p5.2P$^{3/2}$.3d
446.65	0.15849	Ne	500	2s2.2p5.2P$^{3/2}$.3p - 2s2.2p5.2P$^{3/2}$.8d
485.69	0.36748	Ne	150	2s2.2p5.2P$^{3/2}$.3p - 2s2.2p5.2P$^{3/2}$.8s
501.17	0.30753	Ne	250	2s2.2p5.2P$^{3/2}$.3p - 2s2.2p5.2P$^{3/2}$.6d
594.21	0.16115	Ne	5000	2s2.2p5.2P$^{3/2}$.3s - 2s2.2p5.2P$^{1/2}$.3p
614.14	0.29513	Ne	10000	2s2.2p5.2P$^{3/2}$.3s - 2s2.2p5.2P$^{3/2}$.3p
626.45	0.17165	Ne	10000	2s2.2p5.2P$^{1/2}$.3s - 2s2.2p5.2P$^{1/2}$.3p
632.99	0.22415	Ne	3000	2s2.2p5.2P$^{1/2}$.3p - 2s2.2p5.2P$^{1/2}$.5s
639.93	0.87764	Ne	20000	2s2.2p5.2P$^{3/2}$.3s - 2s2.2p5.2P$^{3/2}$.3p
650.52	0.28661	Ne	15000	2s2.2p5.2P$^{3/2}$.3s - 2s2.2p5.2P$^{3/2}$.3p
692.85	0.12610	Ne	100000	2s2.2p5.2P$^{1/2}$.3s - 2s2.2p5.2P$^{3/2}$.3p
703.08	0.24234	Ne	85000	2s2.2p5.2P$^{3/2}$.3s - 2s2.2p5.2P$^{3/2}$.3p
667.71	0.49815	Ne	5000	2s2.2p5.2P$^{1/2}$.3s - 2s2.2p5.2P$^{1/2}$.3p
587.26	0.92354	Ne	5000	2s2.2p5.2P$^{1/2}$.3p - 2s2.2p5.2P$^{1/2}$.4d
656.14	0.87994	H	180	2p - 3d
859.5	0.01049	N	570	2s2.2p2.(3P).3s - 2s2.2p2.(3P).3p
647.08	0.01038	N	300	
664.64	0.00938	N	420	2s2.2p2.(3P).3p - 2s2.2p2.(3P).5s
				2s2.2p2.(3P).3p - 2s2.2p2.(3P).5s
777.45	0.05341	O	2430	2s2.2p3.(4S*).3s - 2s2.2p3.(4S*).3p
				2s2.2p3.(4S*).3s - 2s2.2p3.(4S*).3p
				2s2.2p3.(4S*).3s - 2s2.2p3.(4S*).3p
706.41	0.37223	He	200	1s.2p - 1s.3s
728.07	0.11277	He	50	1s.2p - 1s.3s

Table 4.3: Spectral lines of contaminated gas

Species	Concentration
Hydrogen	98.05 %
Nitrogen	1.51 %
Oxygen	0.44 %

Table 4.4: Make up of the contaminant.

same for the fill with and without hydrogen. The gas fill used essentially emulates that of UG2. Total pressure is 2.04 Torr and helium-neon mix ratio is 15:1.

In each plot the fitted lines are of the form given in equation 4.3 where J_0 is the 0^{th} order Bessel function and r is the normalised tube radius. The coefficients a and b are determined by the least-squares method. In each plot the green line is the measurement without hydrogen (and consequently is always the highest) and the blue line shows the measurement with hydrogen.

$$g = aJ_0(2.405r) + b \tag{4.3}$$

We note the beginning of a central dip in the hydrogen free profiles of figure 4.8 and 4.9. Unfortunately there was not sufficient RF power available to clearly see this effect with hydrogen contaminated gas, however there is a hint of a central dip in figure 4.9.

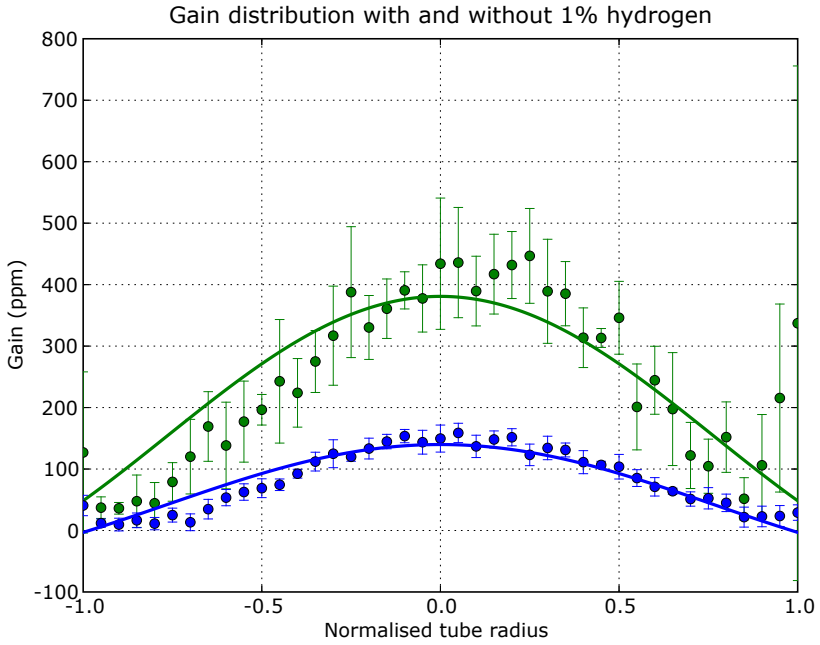

Figure 4.7

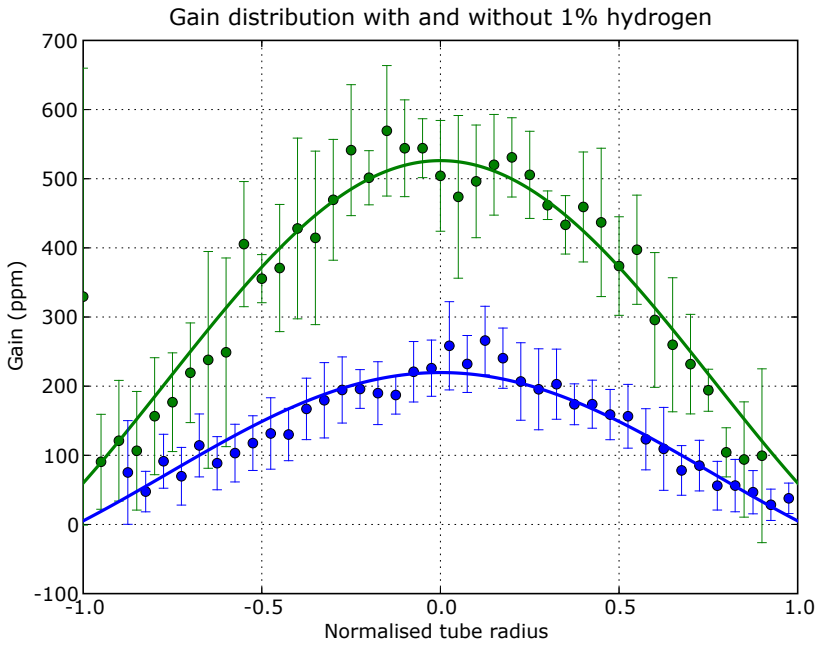

Figure 4.8

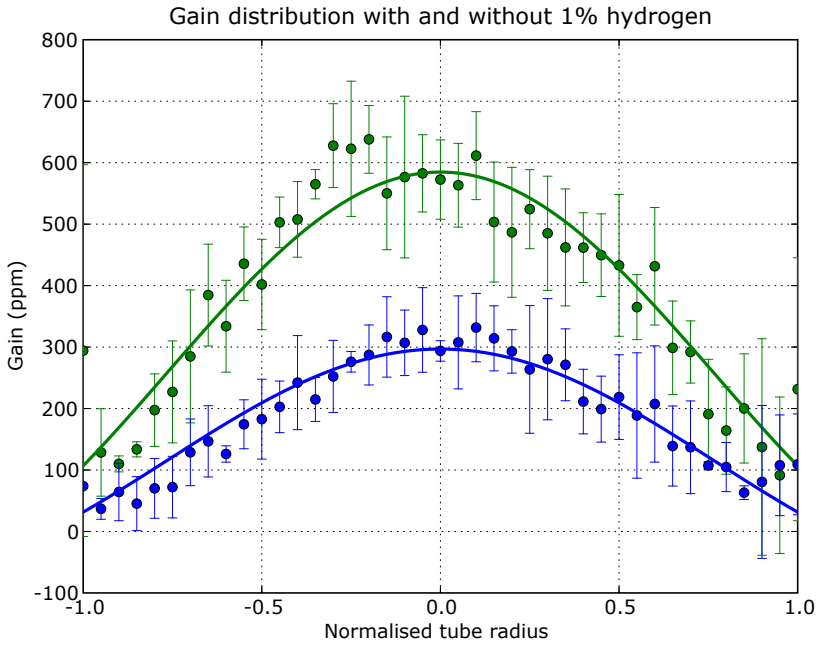

Figure 4.9

Absorption due to excited hydrogen

One simple way in which hydrogen could effect the laser gain is through absorption. In order to test this a series of gain measurements were made with a gas fill of 0.1 Torr hydrogen, 0.85 Torr helium. This is a much higher fraction of hydrogen that would ever accumulate due to outgassing. The absorption was compared to that of a comparable fill of pure helium. No variation was measured across the tube diameter for either gas fill.

Figure 4.10 shows a histogram plot of the distribution of measurements for the hydrogen-helium plasma, where figure 4.11 shows a reference measurement with a helium-only plasma. A small net absorption of 9 ppm was measured, near to the maximum resolution of the instrument as evidenced by the large error evident in the histogram plots.

We can conclude that while absorption due to hydrogen does occur it is a very small effect and certainly does not account for the reduction in gain seen in figures 4.7, 4.8 and 4.9.

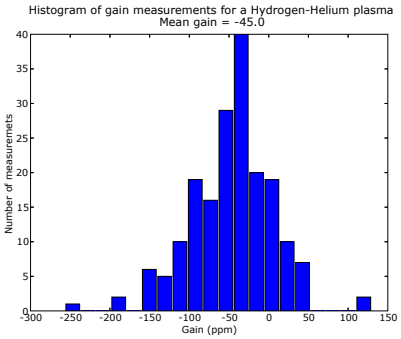

Figure 4.10: H_2 + He absorption

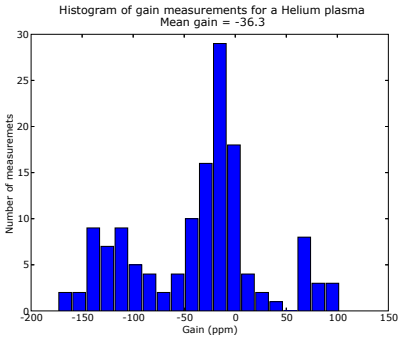

Figure 4.11: He absorption

Gain variation with hydrogen partial pressure

As we now know that hydrogen accumulation is the cause of the degradation of the laser gain over time the next obvious question to ask is: 'Are there a set of parameters we can choose for running the laser in order to minimise the effect of reduction in gain due to hydrogen buildup?'.

In order to address this various gas fills were made and hydrogen leaked into the cavity while laser gain was recorded at the centre of the gain tube over a period of about one hour (this period was dictated by the minimum hydrogen flow obtainable using the leak valve).

In order to make such a measurement the triple valves connecting the cavity to the pumping system must be opened for the duration of the experiment. Even when fully closed, leakage through the helium valve causes a pressure increase of 0.5 mbar per day so a measurable quantity of gas will accumulate over a one hour period. Because of this it was necessary to first fill the cavity with a pressure

about 7 times higher than the operating pressure. The triple valves to the cavity were then closed and the remaining pumping system and plumming pumped down all the way back to the cylinder valves before closing the pneumatic valve to the turbomolecular pump. After then opening the triple valves to allow the system to return to operating pressure the experiment can procede without fear of slowly introducing helium or neon in addition to hydrogen.

Figure 4.12 shows a typical result from this experiment. In each case as hydrogen partial pressure increased the laser gain decreases exponentially, converging to a slight absorption. As the partial pressure of hydrogen is increased further (to much higher pressures than we would ever expect from hydrogen contamination as a result of outgassing) we notice an interesting effect; we see a small recovery in gain, converging to a slight positive value.

The red fitted line on figure 4.12 is a exponential decay of the form $g \propto e^{-\lambda p}$ where λ is the decay constant, p the pressure, g the gain. The fitting occurs only over the region of decay and does not include the region of recovery to positive gain at very high hydrogen partial pressures. Such a line was fitted to the data from each experiment and the decay constants are shown in table 4.4.3.

Unfortunately the results of several experiments (especially those at high pressure, hence lower gain) had to be disregarded as the measurements were too noisy for the exponential fit to converge. This could be improved by obtaining a leak-valve which can be adjusted to a lower rate so that more accurate measurements can be made over a longer time.

From the results to date we can conclude that an increase in total pressure causes a decrease in the decay constant and thus longer laser lifetime. We do not have adequate data to make any conclusions as to the effect of mix ratio on laser lifetime. If the mechanism by which hydrogen causes a decrease in gain is simply electron energy absorption then we would expect to see a decrease in gain linearly proportional to the hydrogen concentration. We see an exponential relationship, indicating a more complex process is probably to blame.

Initial Pressure (Torr)	Helium-neon Mix Ratio	Decay constant
1.09	9:1	37.24
1.21	9:1	23.415
1.29	9:1	27.545
1.15	9:1	41.121
1.21	12:1	29.652

Table 4.5: Comparison of decay rates with increasing hydrogen for various gas mixtures.

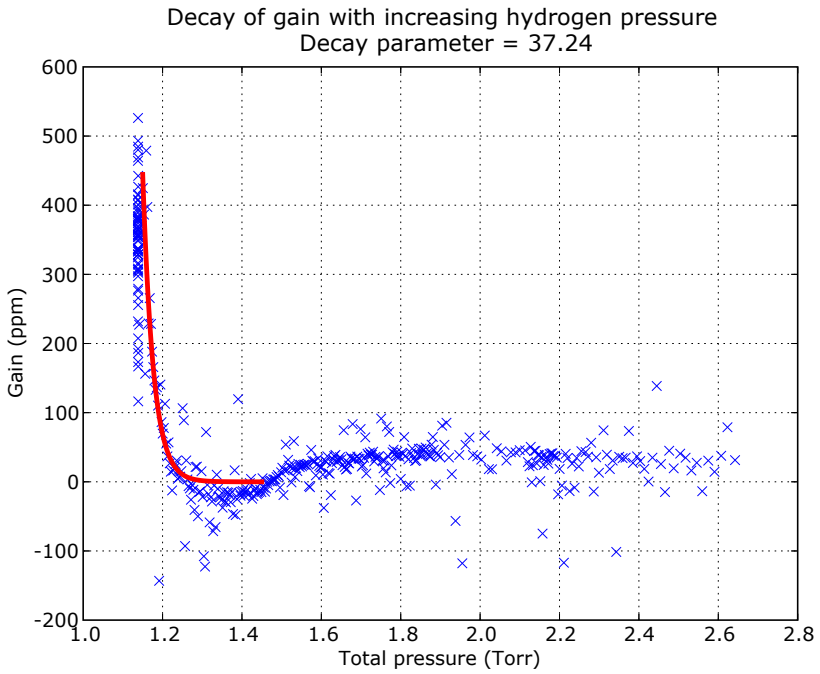

Figure 4.12: The decay of gain as hydrogen is introduced. Red fitted line is an exponential decay.

Gain profile with a hydrogen saturated gain media

In order to investigate the process which gives rise to the small positive gain at high hydrogen partial pressures a gain profile was measured. Because the gain is so small a long measurement was required. The gain profile shown in figure 4.13 was made over 6 hours and an average error of 22 ppm was achieved.

The black line is a simple linear fit. We see no evidence for any structure of the gain profile within the uncertainty. This indicates that neon-hydrogen collisions are probably responsible for the de-excitation of neon from the lower laser level to the ground state.

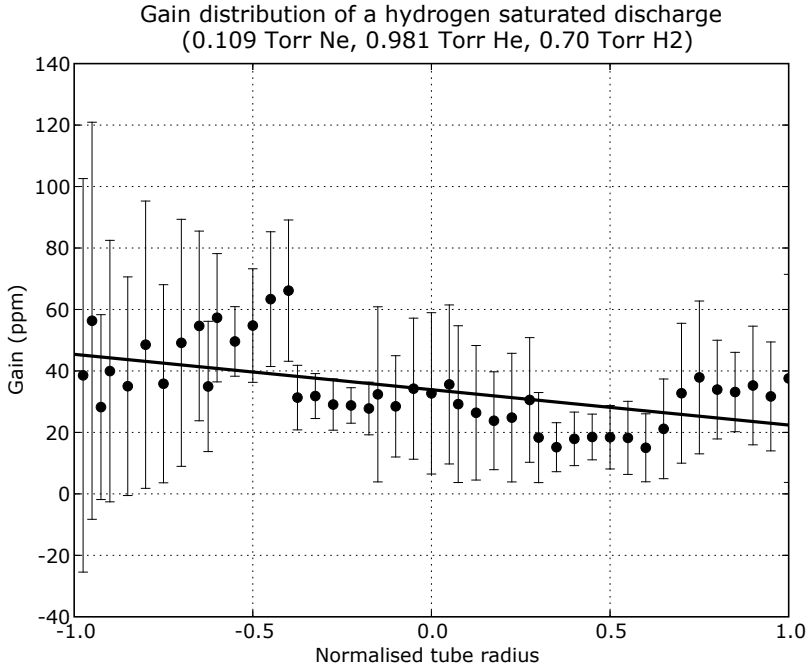

Figure 4.13: Gain profile measured with high hydrogen partial pressure such that the gain has recovered to a positive value. Note the lack of any obvious structure to the distribution.

4.5 Temperature measurements

One of the symptoms we observe of an aging gas fill is a decrease in the threshold power for which operation in multiple longitudinal modes occurs.

In light of the temperature measurements detailed in section 3.7.2 we can propose a mechanism which may be responsible:

1. The gas becomes contaminated with hydrogen, lowering the gain as evidenced in section 4.4.3.

2. Because the ring lasers use a servo control system to maintain constant laser power, RF power increases. This results in an increase in gas temperature as shown in section 3.7.2.

3. At higher temperature the gain curve becomes wider due to Doppler broadening. The peak also shifts slightly in optical frequency. Consequently the gain for the next mode increases.

4. It is possible that the gain for the next mode could become either higher or equal to the gain for the original mode, resulting in a mode jump.

Note that 'mode' above could refer to either the next longitudinal or next transverse mode. If the next transverse mode is permitted by the different effective gain for the profile of this mode then we would expect it to begin operating first as the optical frequency difference between successive transverse modes will be in general less than the FSR.

Figure 4.14 shows gain curves at increasing temperature (made in the same way as figure 2.11). It is clear that the gain decreases with increasing temperature but the gain curve is only slightly broader. Also notice how the peak of the gain curve shifts slightly towards the ^{20}Ne line. The shift between 300 K and 600 K is 32 MHz.

Figure 4.15 shows the difference in gain between the peak of the gain curve and a point 1×FSR to the right. This is expressed as a fraction of the maximum gain and plotted against temperature. The procedure was repeated for the case where no hole-burning[2] was occurring and for a slight hole burning. The ratio of the intracavity intensity to the saturation intensity was 0.0015. This was chosen to be near the maximum ratio for which the gain curve remains concave down. If the gain curve becomes concave up in the centre then split mode[3] operation will occur.

The interesting thing about figure 4.15 is that both lines have zero crossings within the range of gas temperatures we observe. A zero crossing indicates a mode jump is likely to occur. This indicates that the proposed mechanism for decreasing multimode threshold with increasing contaminant build up may be valid.

To confirm the validity of this theory it would be necessary to accurately determine the gas temperature as a function of RF power for a running ring laser such as UG2, repeat the calculation above as accurately as possible for the specific laser parameters and see if mode jumps occur at the predicted power levels.

[2]This is the process by which a running laser beam depletes the population of atoms with Doppler shifted lines at or close to its own optical frequency and consequently 'burns a hole in the gain curve.

[3]The laser is said to be split when the co-rotating and counter-rotating beams operate on different longitudinal modes.

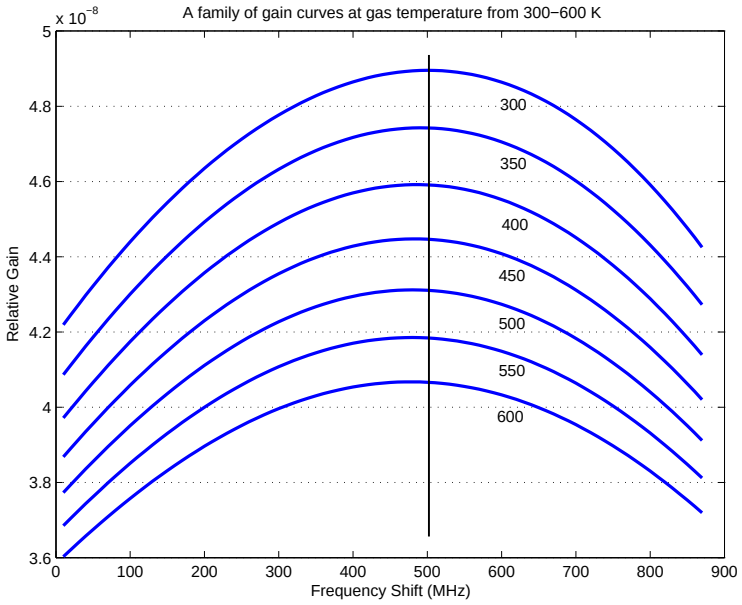

Figure 4.14: Gain curves calculated over a range of gas temperatures. On this scale the vertical line has the width of 2.5 MHz.

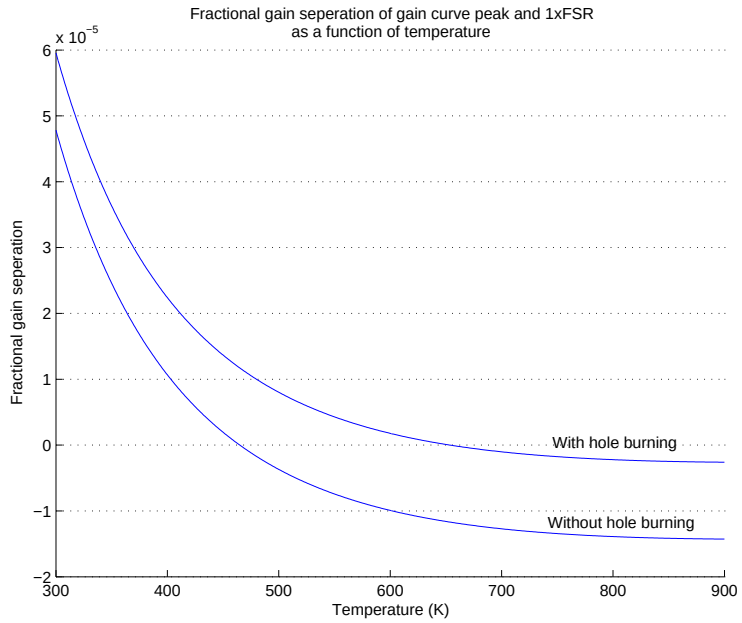

Figure 4.15: Fractional difference in gain between a running longitudinal mode and its nearest neighbour for various gas temperatures.

Chapter 5

Experiment to Detect Super Frame-Dragging

Rotational frame-dragging, also known as the Lense-Thirring effect is a consequence of general relativity applied to a rotating body. Lense and Thirring predicted that the rotation of an object would alter the space-time around it, pulling light with it as it rotates. It is in some ways reminiscent of old 'ether-dragging' models.

For earth size masses the effect is extremely small. If $\mathbf{\Omega}'$ is the observed rotation, $\mathbf{\Omega}$ the rotation rate of the body of moment of intertia I at a distance $\mathbf{R}$ from the centre of rotation is given by equation 5.1 where c is the speed of light and G the gravitational constant [36].

$$\mathbf{\Omega}' = \frac{GI}{c^2 R^3}\left[\frac{3\mathbf{R}}{R^2}\left(\mathbf{\Omega}\cdot\mathbf{R}\right) - \mathbf{\Omega}\right] \tag{5.1}$$

The effect was recently confirmed for the rotating earth as part of the Gravity Probe B experiment. As was first proposed by Dehnen in 1967 [36], a ring laser gyro could be used to measure the gravitomagnetic field resulting from earth rotation. Alternatively a ring laser gyro might be used to detect the gravitomagnetic field of a rotating laboratory mass. While obviously a smaller effect, this approach has the advantage of being able to be switched on and off.

The ring laser group has a long history of proposing such experiments [37] but because of the extreme smallness of the effect, measurement is well beyond the grasp of the current generation of ring lasers.

Recent work by Tajmar *et al.* claims that the gravitomagnetic field resulting from the rotation of Cooper pairs in superconductors [38, 39] is of the order of 10^{30} times larger than the classical result. Experimental work by the same group [23] appears to support this claim. Supercooled rotating lead and niobium disks were used and nearby linear accelerometers detected a transient as the disks were accelerated and decelerated. This effect disappeared when the temperature of

the disks was increased above the superconducting transition.

If this effect is indeed as large as claimed and can be shown to survive independent verification then the impact on gravitational physics would be tremendous.

5.1 Predicted rotational coupling

Tajmar *et al.* report the coupling B_g of rotational velocity of a superconducting mass ω to rotation as observed in the frame of an observer in the gravitomagnetic field of the superconductor relative to the 'fixed' inertial frame to be given by equation 5.2.

$$B_g = 2\omega\frac{\rho^*}{\rho} \tag{5.2}$$

Here ρ is the classical mass density of the superconducting material and ρ^* is the mass density of Cooper pairs in the superconductor.

The mechanism for generating the field is claimed to be essentially a gravitomagnetic analogue of the magnetic London moment. The London magnetic field arises as a consequence of valence electrons inside a superconductor behaving like a superfluid. When a superconductor is rotated these electrons remain stationary while the positively charged atoms move resulting in a magnetic field. The field behaves in a similar fashion to a classical dipole moment, i.e. the intensity decays as the inverse cube of the distance from the superconductor.

A ring laser measures rotation relative to an inertial frame of reference. In this experiment we can consider the space surrounding the superconductor to be dragged slightly around with the superconductor. Because we are holding the ring laser stationary in the laboratory frame[1] the observed rotation will be in the **opposite** direction to that of the rotating superconductor[2].

If we now invoke the concept of gravitomagnetic field lines (anagalous to their magnetic counterparts) then we can determine the direction of rotation as sensed by a ring laser at a location other than directly in the rotating frame of the spinning superconductor. This is depicted in figure 5.1. We see that we would expect to measure a rotation in the same direction as the superconductor in the case of a ring laser measuring rotation in the plane of the superconductors rotation.

It is interesting to note from equation 5.2 that this effect is not simply a larger Lense-Thirring field, it is fundamentally different because the magnitude of the effect does not depend on the mass of the superconductor. However from a practical point of view the inverse cube relationship means overall that the observed field will be larger for superconductors with larger volume.

[1] In a practical sense this means we need to subtract the constant rotation of the earth from the Sagnac signal.

[2] As an aside we note that this is the opposite of what we expect in the case of an electromagnetic field due to Lenz's law.

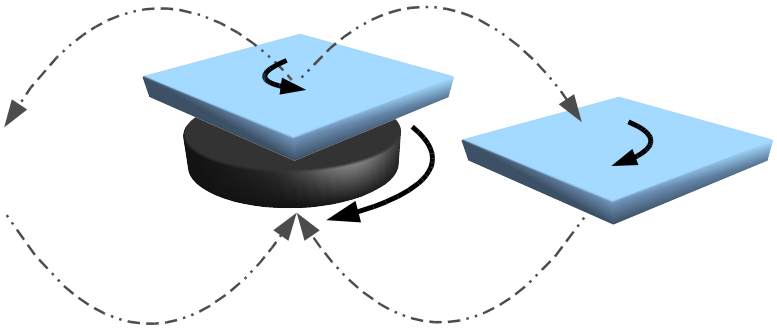

Figure 5.1: Coupling of the superconductors rotating frame to on-axis and in-plane gyroscopes (light squares). Thick arrows indicate rotation direction, dashed arrows indicate 'gravitomagnetic flux'.

One advantage that we have when using a ring laser to measure the gravitomagnetic field is that we would expect to measure a constant signal due to the rotation of the superconductor. With a linear accelerometer only a transient effect would be observable as the superconductor is being accelerated or decelerated. From a practical standpoint this makes it much easier to decouple the measurement from any vibrational or mechanical coupling that might occur as the superconductor is being accelerated.

5.2 Experimental apparatus

5.2.1 Dewar

The apparatus (figure 5.3) consists of an outer stainless steel dewar of outer diameter 150 mm. Inside this dewar we have a large diameter perspex tube. This tube is the same height as the outer dewar. The tube is made so that an inner glass dewar of internal diameter 107 mm fits reasonably tightly. A large steel spring is placed in the bottom of the perspex tube. This spring pushes the top of the inner dewar against a perspex baffle which is 290 mm from the bottom of the apparatus. An o-ring is placed between the top of the inner dewar and the baffle to ensure a good seal. A perspex lid is placed over the perspex tube at the top of the apparatus. This arrangement allows optical access to all of the apparatus.

Holes have been drilled through the centre of the lid and baffle. This allows a fiberglass rod to be inserted. A brass collar is attached to this rod above the baffle with washers placed between the brass and the perspex. A cylinder of high purity lead 38 mm in height and 91 mm in diameter is attached to the bottom of this fiberglass rod just above the bottom of the inner dewar. This arrangement allows the lead to be rotated using an electric drill outside the dewar.

In operation, the outer dewar is first filled with liquid nitrogen. It leaks in through holes drilled in the bottom of the perspex tube to surround the inner dewar. Holes drilled in the lid and baffle allow the inner dewar and the space above the baffle to initially be purged with warm helium gas. This ensures any water vapour and any liquid nitrogen (remaining from pre-chilling the lead with liquid nitrogen) is removed.

An evacuated transfer tube can then be simultaneously lowered into a nearby dewar of liquid helium and through holes in the lid and baffle to the inner dewar. The inner dewar can now be filled with liquid helium. This arrangement allows for complete isolation of the cold nitrogen and helium gas, mitigating the possibility that cold helium gas might condense cold nitrogen gas back to liquid which might then fall back into the inner dewar and condense to frozen nitrogen.

This arrangement is depicted in figures 5.2, 5.4 and 5.3.

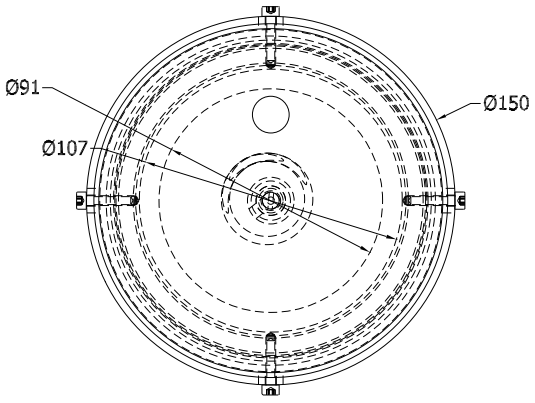

Figure 5.2: Plan of the dewar arrangement from above

5.2.2 Temperature probe

A temperature probe has been built. This consists of a 1 kΩ carbon-ceramic resistor at the end of a stainless steel tube. The tube is placed through holes in the lid and baffle of the apparatus so that the sensing resistor is above the lead. In this way we know that if the resistor is indicating liquid helium temperature then the lead must be completely immersed in liquid helium. If the helium is not boiling then the lead will certainly be at liquid helium temperature and thus superconducting.

The resistor is used as an indicator of temperature by measuring its resistance using the 4-wire method. This is depicted in the circuit shown in figure 5.5. The basic idea is to place two wires on each side of the sensing resistor. A small current flows through the resistor via one pair of wires while the second pair is used to measure the voltage drop across the resistor. If a high impedance voltmeter is used then any resistance of the wires will not effect the measurement.

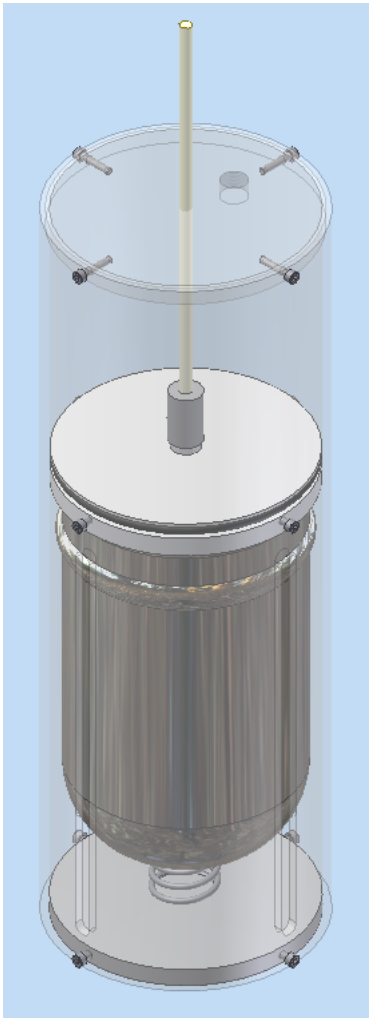

Figure 5.3: Rendering of the dewar arrangement

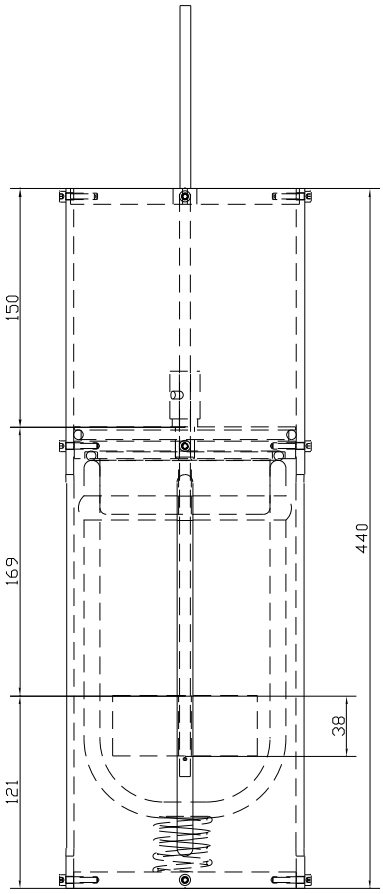

Figure 5.4: Side-on plan of the dewar arrangement

The sensing current is kept small to avoid self heating. This is done by using a 100 kΩ current limiting resistor in series with a 9 V battery. The current limiting resistor is a high precision wirewound type. Measuring the voltage across this resistor determines the current in the circuit. The resistance of the sensing resistor can then be calculated trivially using ohms law.

The relationship between temperature and resistance is given by manufacturer of temperatue sensing resistors that are intended for cryogenic applications by a high order polynomial. We did not have such data so calibrated the resistor in liquid helium and liquid nitrogen and then adjusted the parameters of a typical calibration polynomial. While this does not give good accuracy over the whole range of measurement, it was found to reliably indicate the temperature of liquid helium to within 0.5 K and as such is suitable as a detector of liquid helium.

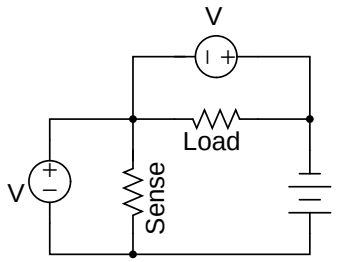

Figure 5.5: 4-wire circuit for temperature sensing.

5.2.3 Tachometer

While not used in the final experiment, a tachometer was designed and built to measure the rotational velocity of the spinning superconductor.

The tachometer consists of a disk with two pairs of 5 mm and 3 mm holes on opposite sides of the disk. A LED and photodiode pair were placed above and below the disk in such a way that light from the LED can pass through the holes. This design allows both rotational velocity to be measured (from the frequency of the light signal) and direction of rotation to be sensed from the shape of the waveform. This is depicted in figure 5.6.

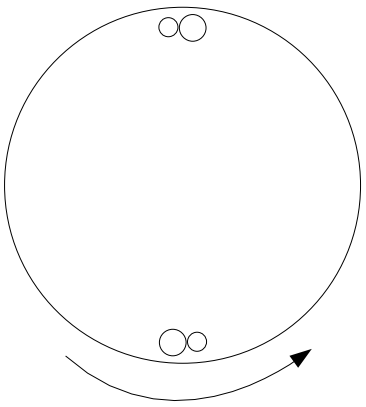

Figure 5.6: Spinning disk arrangement for bi-directional tachometer.

5.3 Predicted field calculations

Firstly we need to find the mass density of Cooper pairs ρ^*. In a superconductor, the super-currents are essentially confined to a thin surface 'skin' of the superconductor (this is similar to the skin effect in classical electromagnetism).

The *London penetration depth* is given by the standard expression shown in equation 5.3. A numerical value of the London penetration depth can be found in literature [6]. For our experiment at liquid Helium temperature (4.22 K) the penetration depth $\lambda \approx 480$ Å.

$$\lambda = \sqrt{\frac{m_s}{\mu_0 n_s q^2}} \tag{5.3}$$

In equation 5.3, m_s is the total mass of the super-current charge carriers, n_s the number of these carriers per unit volume, q the unit charge and μ_0 the usual electromagnetic permeability constant of free space, namely $4\pi \times 10^{-7}$ H/m. Given that Cooper pairs are the charge carriers we find the penetration depth to be:

$$\begin{aligned} \lambda^2 &= \frac{2m_e}{\mu_0 n_s (2e)^2} \\ &= \frac{m_e}{2\mu_0 n_s e^2} \end{aligned} \tag{5.4}$$

And thus the mass density of Cooper pairs ρ^* is:

$$\begin{aligned} \rho^* &= n_s m_s \\ &= \frac{m_e^2}{\mu_0 \lambda^2 e^2} \\ &= 0.011 \text{kgm}^{-3} \end{aligned} \tag{5.5}$$

The density of lead at room temperature is 11340 kg m^{-3}. Accounting for the volumetric expansion coefficient (87×10^{-6} K^{-1}) we find the density at liquid helium temperature to be $\rho \approx 11635$ kg m^{-3}. Thus:

$$\boxed{B_g = 1.89 \times 10^{-6}\omega} \tag{5.6}$$

for lead at 4.22 K. This is comparable to the result of Tajmar *et al.* who quote a value of $3.9 \times 10^{-6}\omega$ for niobium at 0 K.

With the coupling now known we turn our attention to calculating the effective rotation as observed by the UG2 laser. In order to do this we need to find the integral over the area of the ring laser namely $\int\int_{\text{UG2}} \frac{1}{r^3} dA$. A diagram of the area we are integrating over is shown in figure 5.7. The value of the integral of the $1/r^3$ field which we denote A was found by numerical integration to be 10.127.

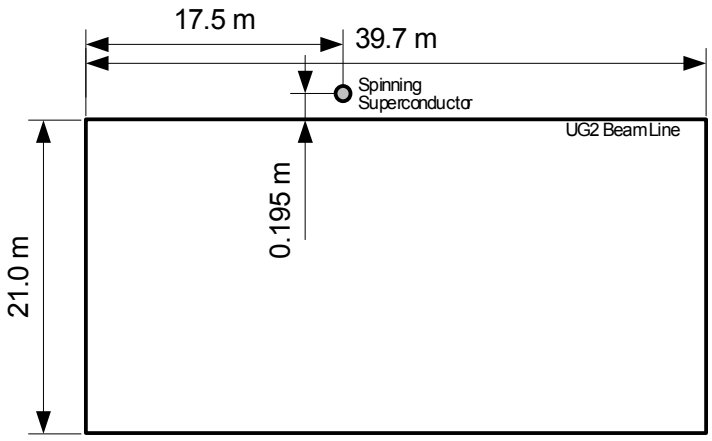

Figure 5.7: Setup of frame dragging experiment with UG2 laser.

With P the perimeter length and λ the laser wavelength we can now find the change in Sagnac frequency due to the total gravitomagnetic flux Φ_G intersecting the ring laser to be:

$$\Delta f_s = \frac{4\Phi_G}{\lambda P}$$

If we define the gravitomagnetic flux as $\Phi_G = \int\int_{\mathrm{UG2}} B_g dA$. To evaluate this integral we need to know a 'far-far field' value of of B_g (i.e. the field strength at a distance of 1 m) which we denote B'_g. This is done by analogy with a single loop solenid. We find the ratio of the magnitude of the field in equatorial plane to that at 1 m from the centre of the loop. Standard formulae are availabe for this in appendix C. Evaluating this for a current of 1 kA gives internal and external fields of magnitude 0.01387 T and 6.4617×10^{-7} T respectively. Thus we find the value $B'_g = 4.66 \times 10^{-5} \times B_g = 9.15 \times 10^{-11}\mathrm{rad}s^{-1}m^{-3}$.

Finally we can quote an expression of the observed change in Sagnac frequency from equation 5.7:

$$\Delta f_s = 4.65 \times 10^{-5}\omega \quad \mathrm{Hz} \tag{5.7}$$

5.4 Experiment and results

The experiment was completed successfully with no problems transferring the liquid helium. The temperature sensor indicated the lead was immersed in liquid helium for the duration of the experiment.

The lead was repeatedly spun both clockwise and counterclockwise a number of times, our best results coming from a run of ≈5 minutes clockwise followed by ≈5 minutes stationary followed by ≈5 minutes counterclockwise. The laser gave very good performance over this time period, achieving a Sagnac stability over the period of each measurement of 0.2 cycles relative to a GPS-locked reference generator set at 2176.785 Hz. This corresponds to a frequency resolution[3] of 0.66 mHz.

The rotational velocity of the lead was 15 revolutions / sec in the clockwise direction and 12 revolutions per second in the reverse direction. These give expected Sagnac frequencies of 4.38 mHz and 3.51 mHz respectively.

Figure 5.8 shows a plot of the results for our best set of data. Figure 5.9 shows a plot of the average Sagnac deviation from figure 5.8 plotted against rotational velocity of the superconductor. The slope of the dashed trendline on this plot is $(2.5 \pm 2) \times 10^{-6}$ cycles / radian. The expected result from theory. By comparison the expected result is 4.8×10^{-5} cycles / radian.

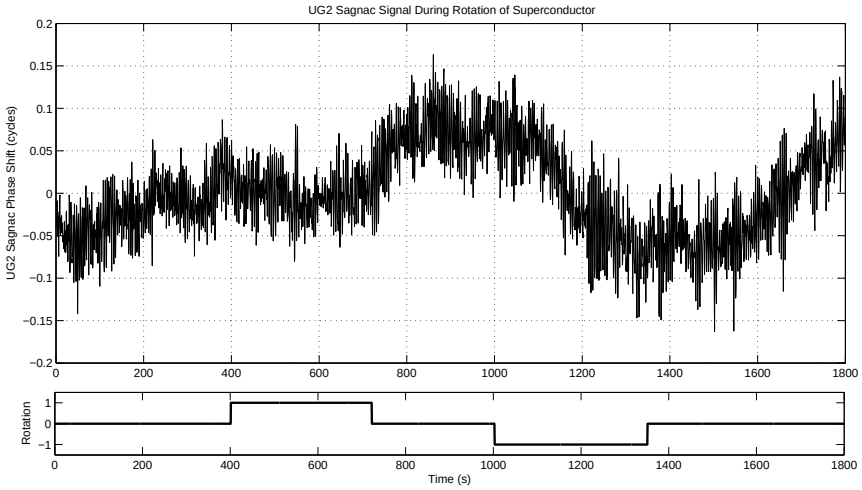

Figure 5.8: Result of the super frame dragging experiment. The top plot shows accumulated Sagnac phase, (units of cycles relative to reference signal generator which was set to 2176.785 Hz) with respect to time. The bottom plot shows rotation — 1 when rotating clockwise, 0 when stationary, -1 when rotating counterclockwise. Note the complete absence of any effect on the Sagnac phase due to the rotation.

5.5 Conclusion

Within the error of the experiment there is absolutely no indication of any change in the Sagnac frequency corresponding to the rotation of the lead superconductor. The error of the experiment is 5% of the predicted effect. We can

[3]This was achieved by subtracting the linear drift of the Sagnac frequency over the period of measurement.

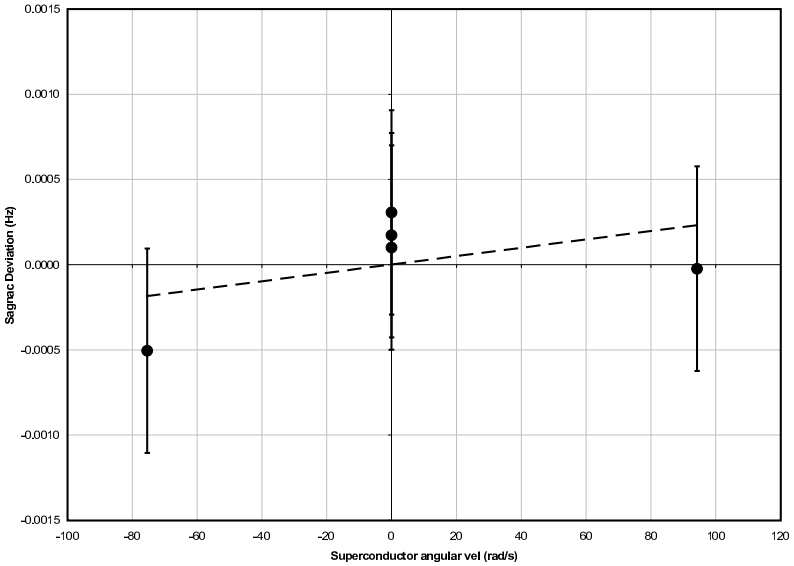

Figure 5.9: Sagnac deviation of the results shown in figure 5.8 plotted against rotational velocity of the superconductor.

thus place a lower limit on any super frame dragging effect. If the effect exists at all it is at least 20 times smaller than that reported by Tajmar *et al.*

5.6 Acknowledgements

The field calculations and numerical integration in this chapter were done by Dr. Bob Hurst. The design and construction of the dewar was primarily the work of Mr. Rob Thirkettle. Also on the experimental team were Mr. Clive Rowe and Prof. Phil Butler. The expense of liquid helium was covered by the Department of Physics and Astronomy, University of Canterbury.

Chapter 6

Data Acquisition Techniques

Throughout the history of the ring laser project LabView and National Instruments data acquisition hardware has been used almost exclusively for the control, data logging and data storage needs of the project. Over many years LabView has become well known for the ease with which simple applications can be developed. In some ways this has hidden the fact that the G language coupled with the LabView development environment form a sophisticated, high performance platform upon which large and complex applications can be developed.

When developing large applications it is essential for the future maintainability of the source code that modern software engineering methodologies are considered from the outset. It is unfortunate that the LabView interface certainly does not encourage such practices. For example there is no built-in facility for user created classes and thus using object orientated techniques during development (add-on tools such as GOOP must be used for this) despite the fact that almost all supplied subVIs operate on objects and a type casting feature is available.

The ring laser data logging software is a classic example of non-structured software development. As the project has grown additional functionality has been added on with little documented structure. As a result it is very time consuming to maintain. It is difficult to reuse existing code in other projects[1] because of intertwined functionality.

6.1 Key problems

- **Coupling of GUI and application logic**

[1]This was found to be the case recently when it was necessary to extract the functionality of the system which reads and processes tiltmeter signals.

The functionality of an application should not be constrained by its user interface. In turn the user interface should not constrain the application logic. One problem with traditional LabView development is that GUI and application logic are coupled — the programmer usually begins by designing the VI front panel and then adds application logic to bind the various controls together.

This causes a problem when one wants to modify either the panel or logic and also means that is is often impossible to reuse pieces of the application in other projects. In addition, it is from the GUI that the 'connector pane' (effectively the parameter list when a VI is being called from another VI) is defined. Often a VI will require internal results from a subVI it is calling yet it is inappropriate to create a front panel item for this specific internal result.

For large systems, it is often necessary to split the data acquisition and control system over more than one computer. For example, high speed data acquisition might best be done on a dedicated machine (to ensure uninterrupted acquisition). Non time-critical tasks such a data processing and archiving may best be done on a separate server while it may be most appropriate for user interface and control to be available on multiple general purpose PCs. These needs may change over the course of the project and if the application logic is tied to the user interface running on each machine then it is almost impossible to move tasks around the machines as needed.

- **Monolithicity**

  When data is required to be accessed from more than one VI there is little choice but to use a global variable if the traditional approach to LabView development is to be employed. This results in hard dependencies between each VI and the global data space.

  This monolithic approach means that if the representation of the global data needs to be changed at a later date then each VI must be changed.

- **Scripting**

  One task which is not well suited to the graphical programming paradigm is the scripting of long and detailed tasks, for example the long sequence of operations required to make a measurement of laser gain as required in this thesis. If implementing such a task using graphical programming it might be necessary to create a sequence structure with over 100 frames. Because of the physical space taken up by such a structure it is difficult to visualise the entire sequence. Since data is generally passed from one frame to the next, considerable rewiring will probably be necessary if the sequence is to be changed. For implementing long scripted tasks a traditional text based language is most appropriate.

- **Algorithm implementation**

  Another task which is not well suited to graphical programming is the implementation of complex algorithms. For example it may be necessary to implement a particular signal processing algorithm described in literature or written in another language. Moving from one text based language to another is easy and can be done relatively quickly. Moving from a text based language to a graphical language is more difficult and takes much more time. In addition if the algorithm contains multiply nested loops and conditionals (as is often the case) it becomes difficult to debug since all the code cannot be seen together.

6.2 Scripting and Algorithms

A number of options are available for combining the benefits of text based programming and graphical programming in LabView.

6.2.1 LabView formula node

LabView provides a formula node feature which is typically used for evaluating algebraic expressions. It is also possible to implement loops and conditionals in a C-like syntax using the formula node. Execution is generally very fast (typically comparable to the equivalent algorithm made in G) and there is no overhead due to calling external libaries.

This approach is good for implementing simple algorithms but the language is extremely limited, providing only the most basic built-in functions. There is no way to call LabView functions from inside a formula node. For example, there is no way to resize an array, this must be done using a LabView function outside the formula node.

If the algorithm is reasonably complex then the formula node is not a good choice. Since external functions cannot be called it is of no use for scripting.

6.2.2 Matlab script

Recent versions of LabView provide a feature that allows Matlab scripts to be embedded in a LabView diagram in much the same fashion as a formula node. Internally it essentially provides a interface between LabView and a Matlab server running on the same machine. This is particularly useful in cases when existing Matlab code needs to be used inside LabView or when features of Matlab provide a simple way to implement a particular algorithm — for example, if an algorithm requires many linear algebra operations.

A disadvantage of this approach is that the way in which current versions of LabView communicate with the Matlab server is specific to Microsoft Windows

and hence this feature is not available on Linux or Apple[2] platforms. In addition it requires a Matlab license. While there is some overhead associated with calling Matlab and in most cases Matlab code will run slower than equivalent LabView code (since Matlab is an interpreted language), in many applications execution speed is not particularly important.

It is not possible to call LabView functions from within a Matlab program so this approach is not useful for scripting.

6.2.3 LabPython

LabPython[3] is an open source[4] implementation of tools for executing Python scripts in LabView. It includes a script node, similar in use to the LabView formula node as well as a suite of VIs for executing and precompiling external Python scripts.

The main benefit of this approach is that it allows all of the very extensive set libaries available for the Python language (many of which are highly optimised) to be used as well as allowing existing Python programs to be used.

The main disadvantage of LabPython is that the project is currently quite stagnant, the most recent release occurring in February 2004. Currently there is only support for Python 2.2, where Python 2.5 is now the current version. While it is possible to compile LabPython for Linux and Apple platforms, this has not been achieved as yet. Documentation is currently very sparse and for this reason it took a long time to get it installed and running during testing.

Like Matlab, python programs running under LabPython cannot call LabView functions so it is not usefull for scripting.

6.2.4 LuaView

LuaView is a toolkit for scripting LabView. The toolkit embeds the Lua scripting language into LabView so that Lua scripts can run inside the LabView runtime.

Lua is a simple yet powerful scripting language. It is implemented as a small library of C function as it is specifically designed to be small and light. It is intended for embedding into existing applications. It does not include a large standard library but instead is designed to use the existing functionality of the software it is embedded into or to use external C libraries. While not a truly object orientated language it does provide meta-mechanisms for implementing classes and inheritance. The language is particularly popular in the computer gaming industry.

Unlike the other options already mentioned, LuaView allows custom LabView-implemented functions to be called from Lua. This makes it useful for scripting.

[2]This platform is currently used for data logging in the ring laser project.
[3]http://labpython.sourceforge.net/
[4]LabPython is available under the GNU Lesser General Public License (LGPL)

In addition the language is also powerful enough to be used for general purpose algorithms programming.

Example: Calling a simple Lua algorithm

Figure 6.1 shows a simple example program (read in from a string constant, usually a larger program would be read from file).

To run the algorithm we must first open a new LuaView state (LuaView states are represented by green wires) and then compile the program. To execute a function we first push the arguments (taken in this case from a front panel control) onto the LuaView stack in the order specified by the Lua function parameters. We then call the function and finally pull the results from the LuaView stack.

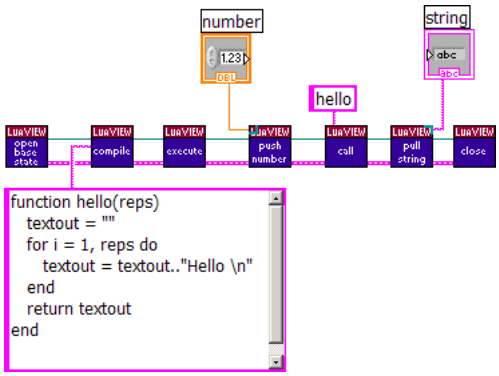

Figure 6.1: Lua example: Calling a simple Lua function from LabView.

Example: Registering a LabView side function

For scripting, we are more interested in executing LabView side functions. Figure 6.2 shows an example of a simple LabView function which can be executed from a Lua script. If it is also likely that the LabView code will need to be executed from LabView then it is advisable to make the LabView subVI in the usual way and then make a LuaView 'wrapper' VI, as shown in figure 6.2. This wrapper then essentially defines the calling and returning parameters and their order.

A template for making such VIs is available as part of LuaView. The template provides just a control and indicator which represent a LuaView reference. We then use the LuaView pull functions to pull the arguments from the LuaView stack to pass into our subVI before pushing the results back onto the LuaView stack.

Once the VI is made we must define a 'calling synopsis' in the documentation section of the VI. The calling synopsis simply consists of a list of the calling arguments followed by the parameters to return. Each entry is simply the

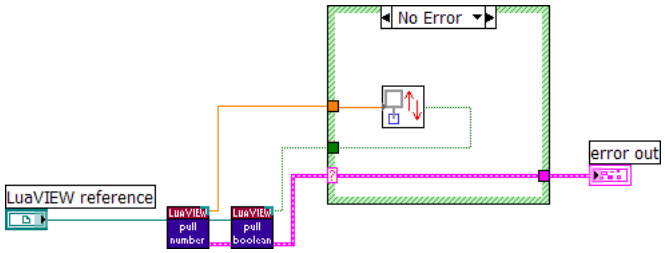

Figure 6.2: Lua example: A simple example of a LabView VI defining a LuaView side function. The shutter VI (for which this VI forms a wrapper) simply takes in a shutter number and boolean and opens or closes the shutter depending on the value of the boolean.

variable type (eg. num for number, str for string) followed by a colon then the variable name. The reasons why the function might fail can be provided after this list so that good error messages can be returned. The VI must also be named with the suffix `_lua.vi`.

While the LuaView push and pull functions are polymorphic[5] we sometimes need to pass our own data structures between Lua and LabView. An example of this is shown in figures 6.3 and 6.4. In this example we want to pass a data structure consisting of a LabView cluster containing timing information and a DAQmx task object to Lua when we execute `startShutter` and then pass it back from Lua to the LabView side function `stopShutter` at some later time.

To do this we use the LabView flatten to string function and pass this string and a type descriptor to the LuaView `Pass flat data` function. This then comes into Lua as a table[6], the elements of which we can manipulate at will. Retrieving the LabView data structure in figure 6.4 is essentially the reverse process.

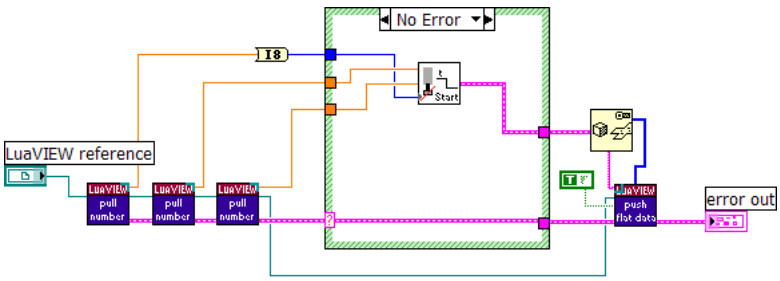

Figure 6.3: Lua example: Passing a LabView data structure to Lua in a LabView side function.

[5] A polymorphic function is one that can be used with different types of data.

[6] The table is the most basic data structure in the Lua language, in other languages a Lua table would be called a *polymorphic dictionary*. Tables in Lua are most often used in much the same way as arrays are used in C style languages.

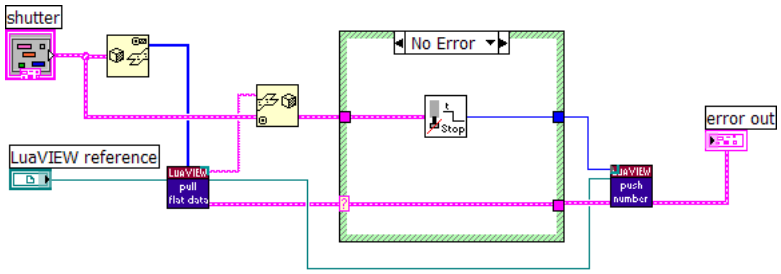

Figure 6.4: Lua example: Retrieving a LabView data structure passed from Lua to a LabView side function.

6.3 Object orientated programming and the GOOP toolkit

A solution to the problem of monolithic LabView programs is to combine related data and function code together to form an *object*. These combinations of data and function code can then be chosen to reflect either physical or mathematical objects that are present in the problem domain.

Then in the event that the representation of some particular data needs to be changed (say from an integer to a float) it is simply a matter of changing it once and providing the necessary methods to access it. If there are compatibility issues with other objects that expect the data in the old format then the original method(s) can be retained and simply made to pass the data in the appropriate format.

This technique is known as object orientated programming. In object orientated programming *classes* are essentially 'object factories', containing all the code for *methods* and data structures from which objects can be created. A true object orientated language also supports *inheritance* in which classes can have *subclasses* — more specialised versions of a class which inherit the data and methods of the parent class.

Objects are used internally in LabView[7] but creating custom classes requires a separate tool. The open source GOOP (graphical object oriented programming) templates form the most common such tool, and various utilities and wizards designed to automate the creation of classes are available. In this work we have used SciWare's GOOP developer.

[7]Here we refer to LabView 7.2 as this is the version that we have. The recently released LabView 8.20 does allow creation of classes though they work differently to GOOP classes.

6.4 Case study: Data logging an experiment in super frame dragging

6.4.1 Object identification

Object identification is a large topic in software engineering, a substantial part of many textbooks [34]. It is the most difficult part of object orientated design, there is no magic formula; the designer must rely on experience and some basic ground rules. In brief, the challenge is to take some problem domain (such as a particular data acquisition system) and decide how to break it up into classes.

In object orientated design it is important to think in terms of 'things' (which will later become classes) rather than functions or procedures. For example 'Thermocouple' might be a good class since it represents a physical object, similarly 'Matrix' might be a good class since in represents a mathematical object. Conversely, 'Thermocouple data processor' or 'Matrix multiplier' are probably bad names for classes since they represent procedures that really are part of the functionality of some more general object or family of objects. A useful technique to object identification is known as *grammatical analysis*. If a description of the system to be modeled is written in natural language then the objects and object attributes are nouns, where as operations or methods are verbs.

Figure 6.5 shows a UML class diagram for controlling an experiment in super frame dragging[8] (see chapter 5).

- The Tachometer class allows objects to be instantiated which represent a physical tachometer made as described in section 5.2. Aside from the measurement task from which the data from the tachometer channel will be read, all instance properties of this class are private. This is because they will never need to be changed once the object is constructed.

  The `Holepairs` integer defines the number of hole pairs on the tachometer disk while the `biglevels` and `smalllevels` float arrays each contain two elements that define the voltage range which indicates either a big or small hole. The method `update()` can be used to read a waveform from the supplied DAQmx task and find the current speed and then set the float variable `speed`, the current value of which can be read with the method `get speed()`.

- The `tempsensor` class defines a generic temperature sensor. It contains a DAQmx task from which the temperature sensor will get data and maintains the current temperature in float variable `temperature`.

  `Carbon RTD` is one of its subclasses. An array of floats `coefficients` defines the polynomial coefficients of the RTD and the float variables `load`

[8] Note that the system presented here is not the exact one which was used for the experiment (for example the tachometer component was not used). The purpose of presenting this system here as a case study is primarily to illustrate data acquisition programming concepts.

`resistor` and `nominal resistance` take the obvious values. All of these are set when the object is construed. The `update()` method computes and updates the current temperature.

In the future if we expand the system to include different types of temperature sensors then we can access them all from a common interface. For example we might take many temperature sensors of different types, cast them into an array of `tempsensor` objects and execute the `get temperature()` method on the array to return an array of temperatures regardless of the inner workings of the different sensor types.

Each object also has a `Destroy` method which frees any memory and stops any running tasks before removing the object. These are standard for every class and not shown in figure 6.5 for clarity.

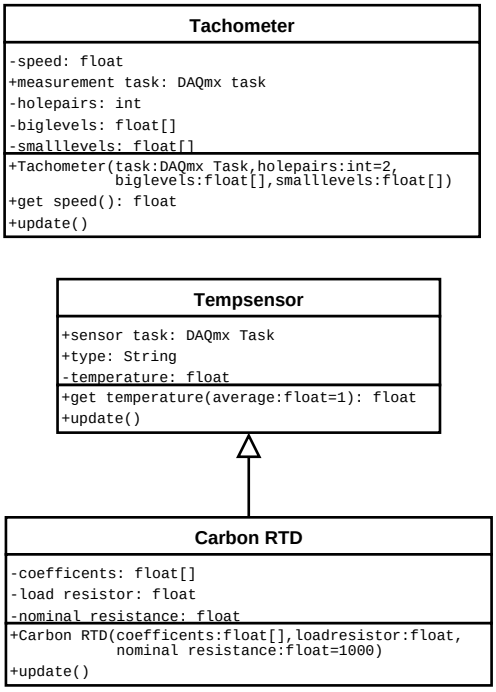

Figure 6.5: UML class diagram of the data acquisition system for the experiment in super-frame dragging.

6.4.2 Implementation

SciWare's GOOP developer it is relatively straightforward to generate classes[9]. We can then add data (instance properties) to the class, update the icons for all the methods of the class and make new methods. When we make a new method, GOOP developer automatically generates the code to read and write variables

[9]The reader interested in the specifics of creating classes with GOOP developer should refer to the many usefull tutorials included with it.

so we just need to add our code to implement the method. An example of this is shown in figure 6.6 which is the update method of the tachometer class. It reads a waveform from the DAQmx task and then uses a subVI to compute the rotational velocity.

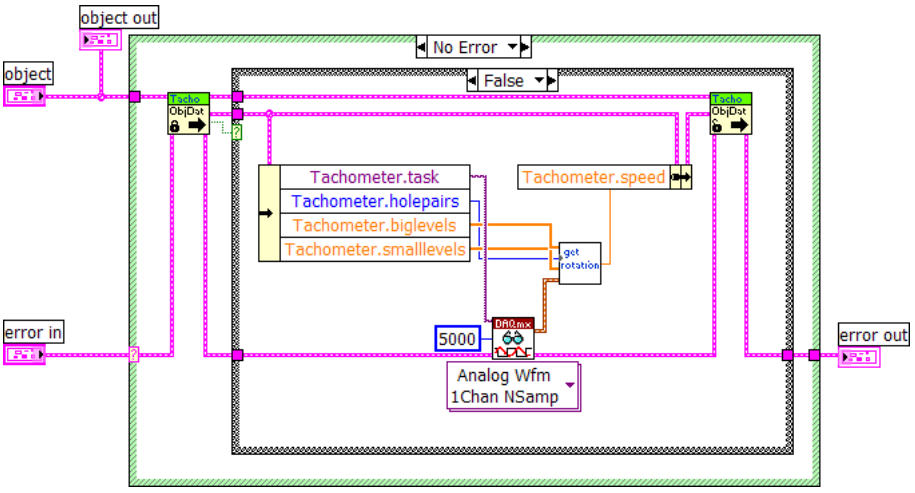

Figure 6.6: The update method of the tachometer class.

Once we have implemented all the classes it is now very easy to make the data acquisition system. This is shown in figure 6.7.

Firstly a DAQmx task object is created. We set the task to allow unread samples to be overwritten, in this way data will be acquired continually to a circular buffer from which we can read at our convenience.

We then create a Tachometer object. A reference to this object is passed to two loops, each of which operate in parallel[10]. The top loop operates at high speed, executing the `update()` method of the tachometer and saving current speed to file. The bottom loop is less time critical and simply reads the rotation speed periodically and updates a graphical user interface (GUI) with this information.

The graphical user interface is simply implemented as a subVI which contains the necessary indicators and controls on the front panel. Each indicator is wired to a hidden control which can be accessed from the connector pane and vice versa. It is good idea to set this subVI to open the front panel automatically when called. This can be done in the VI properties dialog.

Note how using this technique we have managed to completely separate the GUI and application code. We can modify or even completely remove the GUI and the application will remain unchanged. As a consequence of this we have a very natural way of maintaining separate update rates between the user interface and data acquisition and processing. This results in better performance.

[10]Unlike some other languages, parallelisation is very efficient in LabView.

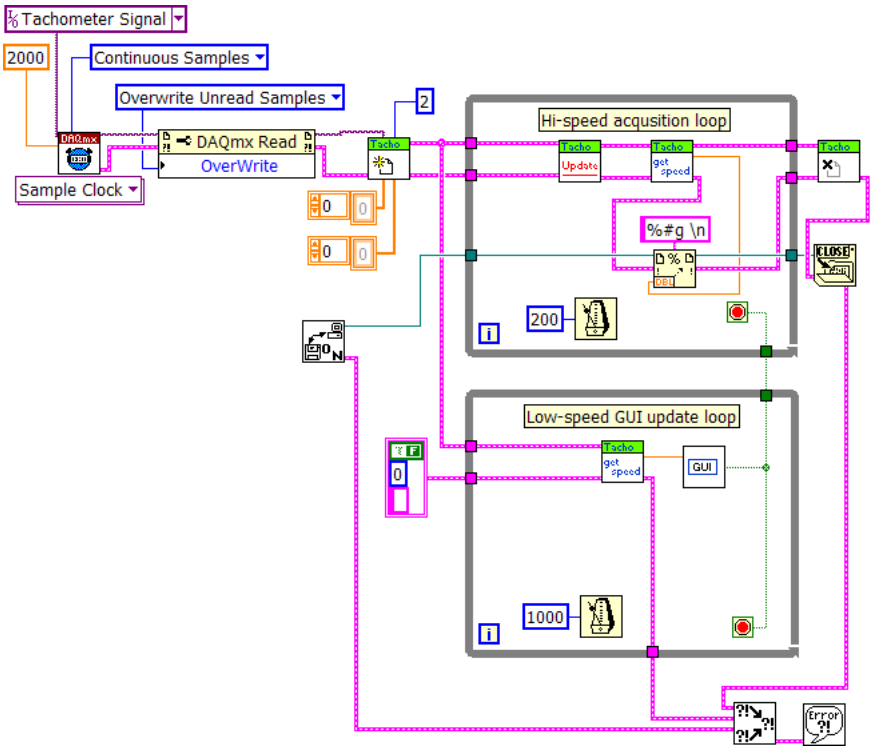

Figure 6.7: The data acquisition program for data logging the experiment in super frame dragging. For clarity only the code relating to the tachometer has been shown. The code for reading the carbon RTD is essentially the same.

6.5 Conclusion

Using modern software engineering techniques when developing data acquisition and control software can allow it to evolve gracefully as needs change over the course of a project, avoiding the considerable redesign that may be needed if the traditional top-down style of development is used. Additionally, if an object orientated design philosophy is used then several difficulties inherent to data acquisition programming can be solved in a very natural way, for example separating update rates of graphical user interfaces from the data acquisition process resulting in better performance.

Complex algorithms and long scripted tasks are often difficult to implement in the G language. For these tasks the Lua language is a usefull tool and when combined with the LuaView toolkit allows easy integration and control of existing LabView code.

Chapter 7

Conclusion

7.1 Progress

7.1.1 Theoretical

An extensive literature survey has been conducted to the point where virtually all published papers directly relevant to the research have been collected and reviewed. As a result of this an in depth understanding of the physical process which give rise to laser gain and its distribution within a general Helium-Neon plasma has been developed. It has become clear that more specific details of these processes are not well understood. These include:

1. The differences between RF and direct DC excitation
2. How recombination takes place at the tube walls to ensure overall electrical neutrality.
3. The electron temperature in the discharge and how this is related to excitation power
4. The mechanism by which hydrogen decreases laser gain.

The mathematical model of radial gain distribution presented by McLeod [25] has been reviewed. It is viewed as a good starting point for comparison with experimental data and several potential improvements to the model have been identified which involve including additional physics into the model not yet taken into account.

While the McLeod model works well to model the gain distribution at high pump rates, the fit drastically decreases at low pump rates. It is hoped that the model can be improved and this problem eliminated.

Once the gain distribution is known (either from high quality experimental data, a theoretical model or both) the transverse mode behaviour can be

determined relatively straightforwardly. Gain distribution is the main factor determining transverse mode operation.

7.1.2 Experimental apparatus

Apparatus capable of resolving the distribution of laser gain in an 8 mm tube to an accuracy of 8 parts per million and horizontal resolution of 50 μm over a 20 hour period, or alternately 20 ppm and 200 μm over a 1 hour period has been successfully constructed. This represents an improvement over any other known work of a factor 2 in both gain and position resolution of a DC discharge, or 10^2 in gain resolution and 2 in position for a RF discharge. It is possible to measure position to 1.25 μm, however since most measurements used a larger gain tube than other work, much more accurate profiles have been obtained.

A thorough error analysis of the experimental set up has been completed. Beam vibration have been measured and equations derived to relate the magnitude of these vibrations into uncertainty in light intensity measurements and hence laser gain measurements. Error inherent in photodiode amplifiers and data acquisition hardware have also been calculated. It has been found that the setup should be entirely satisfactory from this point of view. These results proved invaluable during development to identify sources of error and give confidence in the technique since it took considerable time and effort to eventually obtain satisfactory measurement resolution. Optimising each aspect of the apparatus to obtain satisfactory measurement resolution was certainly the most time consuming aspect of the work presented here.

Measuring changes in light intensity to an accuracy of around 20 parts per million is not a simple task. This is particularly the case in a difficult electromagnetic environment and where long term stability is important. Photodiode amplifiers used in earlier work have been completely re-designed and new versions constructed. When designing high quality photodiode amplifier circuits for precision measurements (such as those required for this thesis) it is necessary to optimise each aspect of the design for the conditions of the test. A generic circuit will not suffice. While using a chopper stabilised op-amp is in theory the best choice for this application, in practice high performance regular op-amps were found to be more convenient.

While a direct measurement of laser gain as measured by the ratio of DC light levels is in some sense a more pure measurement, in practice it is necessary to use a technique involving modulation of either the probe beam or discharge in order to attain acceptable signal to noise ratio.

One unique strength of this experiment is the ability to measure the actual optical power output per atom, a quantity much more amenable to theoretical modelling than a direct measurement of the RF power. Gas temperature measurement has also been achieved and both the optical power output and temperature measurements are consistant — these two independently measured quantities showing a clear linear relationship with intercept very near to 0 K gives good confidence in both methods.

Other innovations regarding the experimental hardware include a novel laser starter, accurate gain tube position controller and reliable computer controlled beam shutters.

7.2 Key results

- The basic shape of the distribution of laser gain across a cylindrical helium-neon discharge tube is a 0^{th} order Bessel function with a central dip developing at high power.
- While the McLeod model gives a reasonably good fit to experimental profiles it does not include all significant physical processes and consequently there is room for improvement particularly at the tube walls. Many results show finite gain as close to the tube walls as can be measured, where the McLeod model predicts a decrease to zero.
- It is important to maintain electrode symmetry if a consistant and symmetrical distribution of gain is to be obtained. A non symmetrical configuration can result in absorption and non symmetric radial gain distribution. This is expected to lead to lasing in high order transverse modes.
- The source of gas contamination in the UG2 laser is 98% hydrogen, 2% air. The hydrogen arises from outgassing of the stainlesssteel tubes from which the laser is constructed.
- The presence of hydrogen causes a significant decrease in laser gain. The mechanism causing this is not optical absorption by ionised hydrogen.
- As the partial fraction of hydrogen is increased above some threshold (typically 30% though this depends on laser parameters) the laser gain actually begins to recover, maintaining a constant value of around 30 parts per million and appears to be independent of hydrogen partial pressure. The distribution of this gain is uniform across the tube, indicating hydrogen collisions are depopulating the lower laser level.
- The efficiency of converting electrical energy (RF coupled into a helium-neon plasma) into optical energy is typically 0.38%.
- The gas temperature in a helium-neon discharge varies with input power from room temperature up to 600 K. This increase in temperature with plasma power (and hence impurity level, if a servo system is used to arrange constant laser power) and the resulting broadening of the gain curve is probably not the cause of decreasing multimode threshold as the gas becomes contaminated.
- The optical power output per atom is linearly dependent on the temperature and was measured to have a gradient of 3.43×10^6 K sec eV^{-1} atom^{-1} and intercept of 9 K.

7.3 Further work

Now that a suitable apparatus has been constructed and its high gain resolution demonstrated, the next obvious next step is to begin a campaign of measurement; measuring radial gain profiles for many different combinations of gas pressure, gas mix, RF power and tube diameter. Doing so will allow a library to be built up which can be used for development of an analytical model, using the work of McLeod as a starting point.

While a good technique has been found for determining optical power output per atom, these measurements have not been presented with the gain profiles presented to date. The reason for this is that presently it is necessary to have a layer of aluminium foil wrapped around the gain tube to provide RF shielding for nearby electronic equipment and removing this shielding has a visable effect on the plasma. It is not possible to see through this foil to make the ruler measurements of discharge size which are a necessary parameter in the optical power calculations. This could be remedied by an alternate shielding arrangement. Ideally the longitudinal distribution of plasma light could be measured electronically. It may be possible to measure this using a linear photodiode array (such as those used in a fax machine), camera or even a scanning arrangement using an optical fibre which would isolate any electrical equipment from the area immediate to the discharge.

Additional work remains regarding obtaining a better description of plasma impedance. This could be useful for design of impedance matching circuits and may also provide a way of estimating electron density. Measuring the VSWR along a transmission line connected to the plasma electrodes is a possible method for measuring the plasma impedance.

In order to gain an understanding of the process by which hydrogen leads to reduced gain it is necessary to repeat measurements detailed in section 4.4.3 with a slower leak rate and hence better measurement resolution. With these results and some analysis of rate equations for decay of the quantum states of the plasma consituants it is likely that the mechanism can be explained.

7.4 Acknowledgements

I would like to acknowledge the generous contributions of the following people:

- **Dr. Bob Hurst** – primary supervisor
- **Mr. Robert Thirkettle** – considerable technical help
- **Mr. Graeme MacDonald** – help with transmitter drive electronics
- **Mr. Ross Ritchie** — helping with modifications to stepper motor control circuitry
- **Mr. David MacKenzie** – proofreading and arranging mass spectrometry
- **Prof. Phil Butler** – senior supervisor
- **Mr. Alexander Velikoseltsev** – source code for gain curve calculations
- **Mr. Albert-Jan Brouwer** — help with LuaView
- **Miss. Tra Dinh** — help with geometry in section 3.2.2
- **Mr. Ewan Orr** — proofreading

Bibliography

[1] K. Altmann, C. Pflaum, and D. Seider. Three-dimensional computation of laser cavity Eigenmodes by the use of finite element analysis (FEA). *SPIE Proc., Photonics West, Symposion LASE*, pages 5333–16, 2004.

[2] D. A Andrews and T. A King. UHF excitation of helium-neon lasers: I. Selection of pumping frequency. *J. Phys. D: Appl. Phys*, 22:1308–1314, 1989.

[3] D. A Andrews and T. A King. UHF excitation of helium-neon lasers: II. Comparison with DC. *J. Phys. D: Appl. Phys*, 22:1315–1320, 1989.

[4] S Donati. *Photodetectors - Devices, Circuits and Applications*. Ptrntics Hall PTR, 2000.

[5] A. G. Fox and T. Li. Resonant modes in a maser interferometer. *Bell Sys. Tech. J.*, 40:453–458, 1961.

[6] RF Gasparovic and WL McLean. Superconducting Penetration Depth of Lead. *Physical Review B*, 2(7):2519–2526, 1970.

[7] D. E. Golden and H. W. Bandel. Absolute total electron-helium-atom scattering cross sections for low electron energies. *Phys. Rev.*, 138(1A):A14–A21, Apr 1965.

[8] EI Gordon and AD White. Similarity laws for the effects of pressure and discharge diameter on gain of HeNe lasers. *Applied Physics Letters*, 3(11):199–201, 2004.

[9] G Gouy. *Compt. Rendue. Acad. Sci. paris*, 110:1251–1253, 1890.

[10] G Gouy. *Ann. de Chim. et Phys*, 24:145–213, 1891.

[11] J Graeme. *Photodiode Amplifiers — Op Amp Solutions*. McGaw-Hill, 1995.

[12] R. Graham. Experiment to characterise the distribution of excited states in a helium-neon plasma discharge. Technical report, University of Canterbury, 2005.

[13] Melles Griot. *Optics Guide 4*. Melles Griot, 1988.

[14] Guru and Hiziroglu. *Electromagnetic Field Theory Fundamentals*. Pws Pub Co, 1999.

[15] H. Haberland, W. Konzt, and P. Oesterlin. Interaction potentials and energy transfer cross sections for collisions of metastable helium and neon. 11: He (2'S)+ Ne. *J. Phys. B: At. Mol. Phys*, 15:2969–2988, 1982.

[16] N.S. Harris. *Modern vacuum practice*. 1989.

[17] Charles E. Head and M. E. M. Head. Mean lives of some $3p$ levels of neon ii. *Phys. Rev. A*, 2(6):2244–2250, Dec 1970.

[18] G. Herziger, W. Holzapfel, and W. Seelig. Verstärkung einer He-Ne-Gasentladung für die Laserwellenlänge λ= 6328 AE. *Zeitschrift für Physik A Hadrons and Nuclei*, 189(4):385–400, 1966.

[19] E. A. Hinds, J. E. Clendenin, and R. Novick. Decay rate of the $2^2s_{\frac{1}{2}}$ state of singly ionized helium. *Phys. Rev. A*, 17(2):670–676, Feb 1978.

[20] T King. *Ring Laser Dynamics*. PhD Thesis, 1999.

[21] C. A. Kocher, J. E. Clendenin, and R. Novick. Lifetime of the $2^2s_{\frac{1}{2}}$ state of singly ionized helium. *Phys. Rev. Lett.*, 29(10):615–618, Sep 1972.

[22] Y.M. Ling and S.E. Wu. 350 mW high-power He–Ne laser and its application in photodynamic therapy. *Review of Scientific Instruments*, 76(12):126107–126107, 2005.

[23] B. Seifert K. Marhold M. Tajmar, F. Plesescu. Measurement of Gravitomagnetic and Acceleration Fields Around Rotating Superconductors. *Arxiv preprint gr-qc/0610015*, 2006.

[24] J. V Martinez. Influences of plasma-tube-surface interactions on the helium-neon laser lifetime. *Journal of Applied Physics*, 37:4477–4483, 1966.

[25] D McLeod. *Seismic Effects in Ring Lasers and Transverse Mode Selection in Helium-Neon Lasers*. PhD Thesis, 1999.

[26] R. G Montague, M. F. A Harrison, and A. C. H Smith. A measurement of the cross section for ionisation of helium be electron impact using a fast crossed beam technique. *Journal of Physics B*, 17:3295–3310, 1984.

[27] NI. Switching considerations. *National Instruments Developer Zone*, 2005.

[28] E Nolan. Demystifying auto-zero amplifiers. *Analog Dialogue*, 34-2:1–6, 2000.

[29] P Rako. *Photodiode Amplifiers - Turning Light into Electricity*. National Semiconductor, 2004.

[30] D. Schuöcker, W. Reif, and H. Lagger. Theoretical Description of Discharge Plasma and Calculation of Maximum Output Intensity of He-Ne Waveguide Lasers as a Function of Discharge Tube Radius. *Opt. Commun*, 13:6–12, 1975.

[31] Vishay Semiconductors. Bpw34 - silicon pin photodiode. Technical report, Vishay Semiconductors.

[32] A. E. Siegman. *Lasers*. University Science Books, 1986.

[33] W.T. Silfvast. *Laser Fundamentals*. Cambridge University Press, 2004.

[34] I. Sommerville. *Software Engineering*. Addison-Wesley Longman Publishing Co., Inc. Boston, MA, USA, 1989.

[35] S. P. Spoor and I. D. Latimer. An acurate determination of the radial distribution of gain at 633 nm in small bore helium-neon discharges. *J. Phys D: Appl. Phys*, 17:1607–1615, 1982.

[36] G. E. Stedman. Ring-laser tests of fundamental physics and geophysics. *Rep. Prog. Phys*, 60:615–688, 1997.

[37] G E Stedman, K U Schreiber, and H R Bilger. On the detectability of the Lense-Thirring field from rotating laboratory masses using ring laser gyroscope interferometers. *Classical and Quantum Gravity*, 20(13):2527–2540, 2003.

[38] M. Tajmar and C.J. de Matos. Coupling of Electromagnetism and Gravitation in the Weak Field Approximation. *Journal of Theoretics*, 3, 2001.

[39] M. Tajmar and C.J. de Matos. Gravitomagnetic field of a rotating superconductor and of a rotating superfluid. *Physica C*, 385 (4):551–554, 2003.

[40] Linear Technology. Ltc1050 - precision chopper stabilized operational amplifier with internal capacitors. Technical report, Linear Technology.

[41] Thorn. Power supplies and signal generators. *Physics World*, page 52, 1989.

[42] V. A. Tsarkov and M. I. Molchanov. Measurement of gain distribution in the tube on a helium-neon laser (λ=0.63 μm) under high frequency excitation. *Opt. Spektrosk*, 35:328–329, August 1972.

[43] P. Haldemann U.E Hochuli and H.A. Li. Factors influencing the relative frequency stability of he-ne laser structures. *Rev. Sci. Instrum*, 45(11):1378–1381, 1974.

[44] D Wright. *Optimisation of Ring-laser Gyroscopes*. PhD thesis, University of Canterbury, 2001.

[45] R. T Young, C. S Willett, and R. T Maupin. Effect of helium on population inversion in the helium-neon laser. *Journal of Applied Physics*, 41:2936–2942, 1970.

Appendix A

Data acquisition source code

Listing A.1: Lockmeasure.vi: Scripts the entire acquisition of a gain profile using the plasma modulation method.

```
1  register.private_dir(path)
2  outputfile = "gainprofile.txt"
3
4  -- Following function does an individual measurement
5
6  function measuregain(amplitude, Grf, Rrf)
7      -- Plasma characteristics
8      striketime = 15
9      minplasma = .20
10
11     -- Shutter characteristics
12     openingTime = 350
13     closingTime = 200
14
15     -- Measurement timing sequence.
16     backgroundMeasureTime = 80
17     calMeasureTime = 320
18     gainMeasureTime = 480
19     plasmaMeasureTime = 80
20     rfMeasureTime = 40
21
22     -- Carry out measurements
23
24     t1=gettime()
25     -- open shutters
26     -- Syntax - Shutter(number [0 or 1], true [opened] or
       false [closed]
27     Shutter(0,true)
28     Shutter(1,true)
29     wait(openingTime)
30     t2=gettime()
```

```
31
32      -- Make measurement of photodiode calibration constant
33      C = getPhotodiodesMean(calMeasureTime, false)
34      C1=C[1]
35      C2=C[2]
36      t3=gettime()
37
38      -- Strike plasma
39      DriveTrans(1)
40      wait(striketime)
41      t4=gettime()
42
43      -- Modulate and measure gain + plasma + RF using lock in
44      Gg, Rg, phasematch = PlasmaLock(amplitude,minplasma, 5.0)
45      t5=gettime()
46
47      DriveTrans(0)
48      -- Close shutter 0 (blocks probe laser)
49      Shutter(0,false)
50      wait(closingTime)
51      DriveTrans(1)
52      wait(striketime)
53
54      t6=gettime()
55
56      -- Measure signal from plasma light only
57      Gp, Rp, phasematch = PlasmaLock(amplitude,minplasma, 5.0)
58      t7=gettime()
59
60      -- Close shutter 1 (blocks plasma + laser)
61      Shutter(1,false)
62      wait(closingTime)
63      t8=gettime()
64
65      -- Get extra signal from RF inteference if this is the
        first measurement in this position
66      if (Grf==0 and Rrf==0) then
67          Grf, Rrf, phasematch = PlasmaLock(amplitude,minplasma,
              5.0)
68      end
69      t9=gettime()
70
71      -- Plasma off
72      wait(50)
73      DriveTrans(0)
74      wait(50)
75      t10=gettime()
76
77      k = C[1]/C[2]
78      gain = 1000000 * (k*(Gg-Gp))/(Rg-Rrf)
79
80      return gain, Gp-Grf, Grf, Rrf
81  end
82
```

```
83  -- Gain measurement script starts here
84
85  -- Set parameters for measurement. Positions are in mm
86  startposition = 1
87  endposition = 9
88  stepsize = 0.2
89  amplitude = 0.8
90  reps = 15
91
92  -- Write file header
93  WriteToFile("Startring gain profile measurement
    "..os.date().."\n",path..outputfile,false)
94
95  -- Make measurements
96  existing=""
97  datastring=""
98  r=0
99  for position = startposition, endposition, stepsize do
100     DriveTrans(0)
101     wait(20)
102     ServoStepper(position)
103     RF1=0
104     RF2=0
105     for r = 1, reps do
106         gain, plasma, RF1, RF2 =
            measuregain(amplitude,RF1,RF2)
107         datastring = ""..position.."  "..gain.."
            "..plasma.."\n"
108         print (datastring)
109         WriteToFile(datastring,path..outputfile,true)
110     end
111 end
```

Listing A.2: Simplemeasure.vi: Scripts the entire acquisition of a gain profile using the direct ratio method method.

```
1   register.private_dir(path)
2
3   function doMeasurement(measurevoltage)
4       -- Plasma characteristics
5       strikevoltage = 0
6       offvoltage = 2
7       striketime = 13
8
9       -- Shutter characteristics
10      openingTime = 350
11      closingTime = 200
12
13      -- Measurement timing sequence.
14      backgroundMeasureTime = 80
15      calMeasureTime = 320
16      gainMeasureTime = 480
17      plasmaMeasureTime = 80
18      rfMeasureTime = 40
```

```
19
20      logdata = false
21
22      -- Carry out measurements
23      print "Starting measurement of laser gain ..."
24
25      A = getPhotodiodesMean(backgroundMeasureTime, logdata)
26
27      -- open shutters
28      -- Syntax - Shutter(number [0 or 1], true [opened] or
        false [closed]
29      Shutter(0,true)
30      Shutter(1,true)
31      wait(openingTime)
32
33      D = getPhotodiodesMean(calMeasureTime, logdata)
34
35      -- Phase H
36      driveplasma(strikevoltage)
37      wait(striketime)
38      driveplasma(measurevoltage)
39      wait(striketime)
40      H = getPhotodiodesMean(gainMeasureTime, logdata)
41
42      -- Phase F
43      Shutter(0,false)
44      wait(closingTime)
45      F = getPhotodiodesMean(plasmaMeasureTime, logdata)
46
47      -- Phase E
48      Shutter(1,false)
49      wait(closingTime)
50
51      E = getPhotodiodesMean(rfMeasureTime, logdata)
52      driveplasma(offvoltage)
53
54      print ("A1="..A[1].." A2="..A[2])
55      print ("D1="..D[1].." D2="..D[2])
56      print ("H1="..H[1].." H2="..H[2])
57      print ("F1="..F[1].." F2="..F[2])
58      print ("E1="..E[1].." E2="..E[2])
59      -- Compute laser gain and plasma power
60
61      b_1 = A[1]
62      b_2 = A[2]
63      print ("b1="..b_1.." b2="..b_2)
64
65      r_1 = E[1] - b_1
66      r_2 = E[2] - b_2
67      print ("r1="..r_1.." r2="..r_2)
68
69      l_1D = D[1] - b_1
70      print ("l_1D="..l_1D.." l_2D="..(D[2]-b_2))
71      k = 1/((D[2] - b_2) / l_1D)
```

```
72      print ("k="..k)
73
74      p_2 = (F[2] - r_2 - b_2)
75
76      g_ppm = ((((  (H[2] - b_2 - r_2 - p_2) * k ) / (H[1] - b_1
        - r_1) ) - 1) * 1000000)
77
78      print ("reference = "..(H[1] - b_1 - r_1))
79      print ("detector = "..k*(H[2] - b_2 - r_2 - p_2).."
        (raw="..H[2].."  )" )
80
81      print ("Gain = "..g_ppm.." ppm : Plasma = "..p_2.." V")
82
83      if logdata then
84          getGlobalWaveformRecord()
85      end
86
87      return g_ppm, p_2
88  end
89
90  startposition = 0
91  endposition = 12
92  step = 0.1
93  averages=4
94  p={}
95  g={}
96  i=0
97  gs=0
98  gm=0
99  for position=startposition,endposition,step do
100     ServoStepper(position)
101     for gm=1,averages do
102         gain, plasma = doMeasurement(1.1)
103         gs=gain+gs
104     end
105     gs = gs/averages
106     p[i] = position
107     g[i]=gs
108     i=i+1
109 end
110 print ("Finished")
111 for x=0,(i-1) do
112     print (""..p[x].." ,"..g[x])
113 end
```

The following figures show the most important VIs. In each case an image of the VIs icon is placed in the top right corner of the diagram for reference.

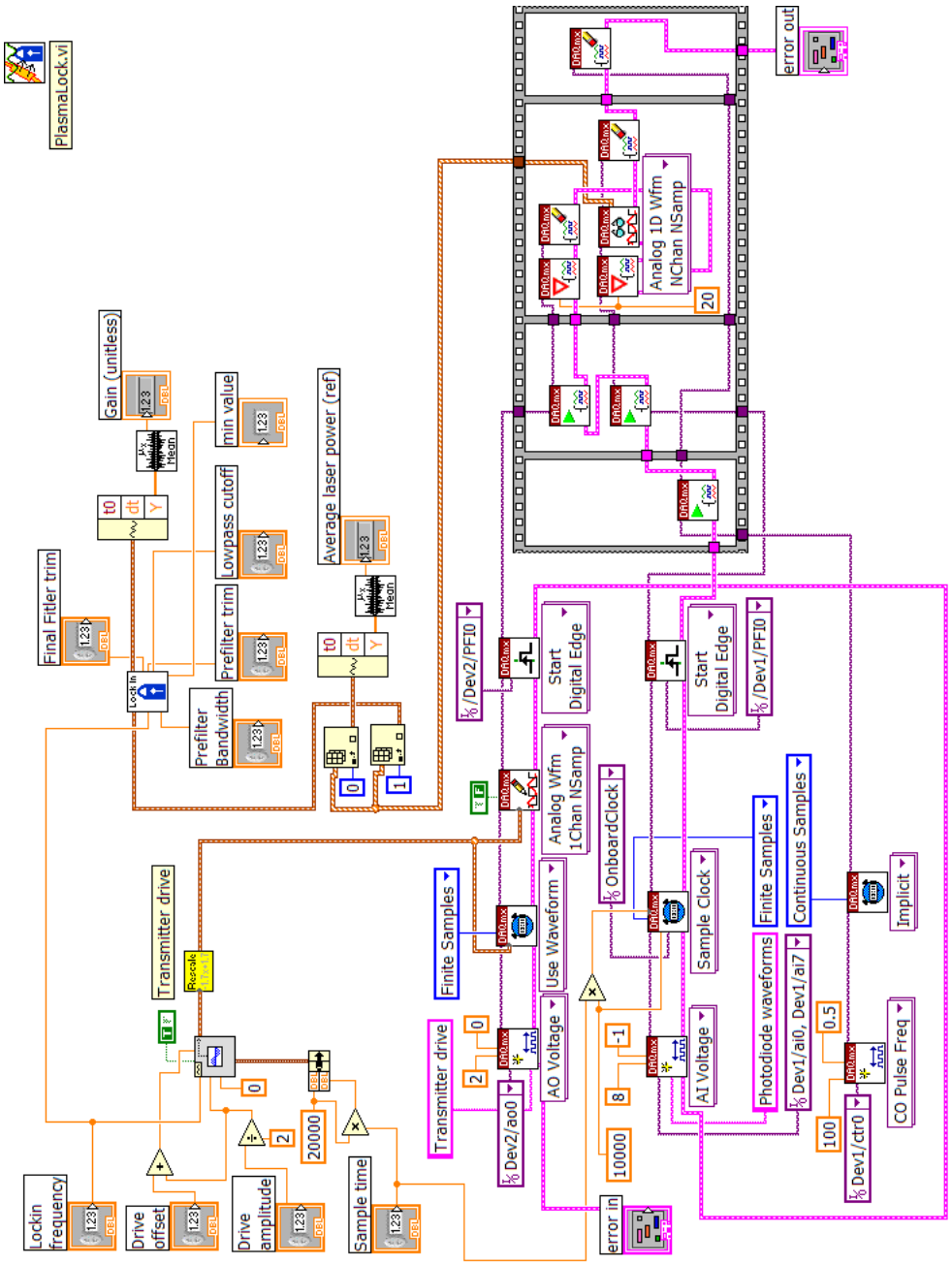

Figure A.1: This VI starts controls the plasma and records the waveforms which are then passed to the lock-in amplifier.

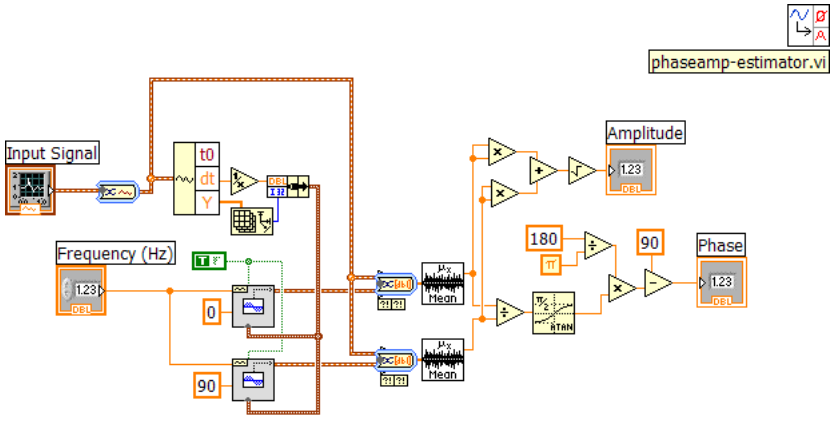

Figure A.2: This VI takes a waveform and computes the phase and amplitude.

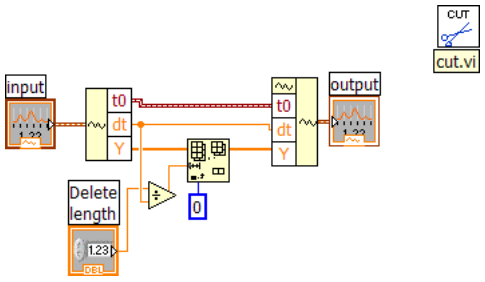

Figure A.3: This VI simply removed an unneeded beginning section of a waveform.

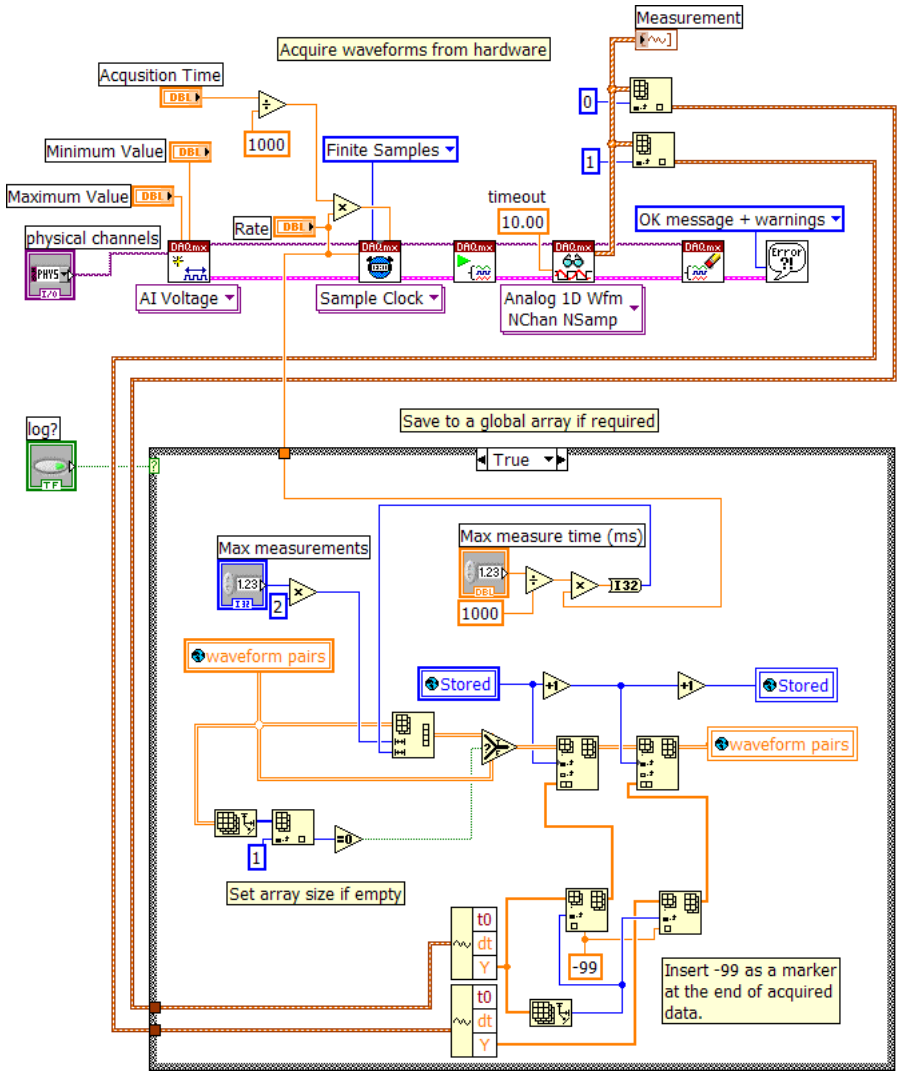

Figure A.4: This VI simply acquires waveforms from both photodiodes. The complicated code at the bottom of the diagram is for saving the acquired data to a global array. This is usefull only for debugging.

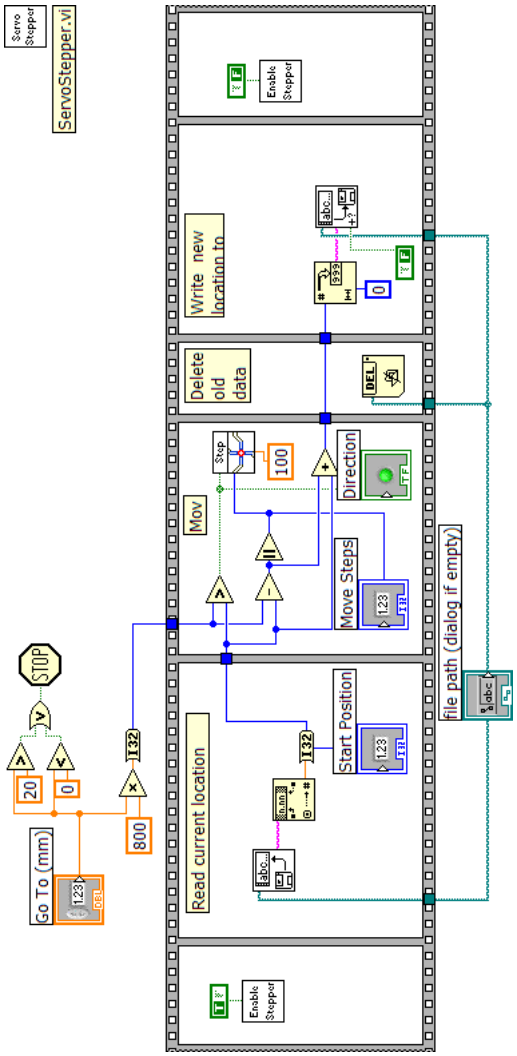

Figure A.5: This VI simply controls the stepper motor. The current position of the stepper motor is recorded to a file so the program always knows where it is. It also provides a safeguard to ensure that the stepper motor does not move the gain tube outside the safe range which may cause damage to the micrometers or stepper motor.

Appendix B

Data analysis source code

The program in listing B.1 was used to plot all the gain profiles presented in this thesis.

Listing B.1: plotprofile.py: Plots gain profile and fits a trendline using the least squares method.

```
1  from Numeric import *
2  from math import *
3  from stats import *
4  from pylab import *
5  from string import *
6
7  import string
8  import scipy
9  from scipy import optimize
10
11 # This function is typically changed by the user.
12 # An example is shown below
13 def main():
14
15    plotprofile ('edgeprofile.txt',10.0,'nofit data','Black')
16    plotprofile ('edgeprofile.txt',10.0,'expsqrt','Blue')
17    plotprofile ('edgeprofile.txt',10.0,'exp','Red')
18
19    title('Gain distribution near tube wall \n 1.21 Torr, 12:1
      He:Ne mix')
20
21    xlabel('Tube position (mm)')
22    ylabel('Gain (ppm)')
23    xlim(-0.01,1.0)
24
25    meanplasma('hiresprofile.txt',8.0,5.0)
26
27    grid(True)
28    show()
29
30 # This function allows fitting of a file (filename) to a given
```

```
31 # fitting function. It also plots the profile, but does not
32 # show it. (User must use show() afterwards)
33 # The sigma parameter is the maximum standard deviation to
34 # include when removing outliers
35 # Colour is the name of the colour
36 # Fitting is a string and can be one of either mcleod,
37 # mcleod2, mcleod-offset,
38 # bessel, cubic, bigpoly, exp, expeqrt or linear or nofit if
39 # only the data need to be plotted.
40 def plotprofile(filename, sigma, fitting, colour):
41   polyorder = 3
42   minfit = 0.00
43   maxfit = 1.0
44
45   fitting = fitting+' '
46
47   tubedia = 8.0
48   tubecent = 5.0
49
50   pos, gain, gain_stdev = getprofile (filename, sigma)
51   pos = array(normalisepos(pos, tubedia, tubecent))
52
53   print "Average error bar
     "+str(sum(gain_stdev)/len(gain_stdev))
54
55   gain=array(gain)
56   gain_stdev=array(gain_stdev)
57
58   def residuals(p, y, x):
59     return y-peval(x,p)
60   def peval(x, p):
61     if (find(fitting,'mcleod ') != -1):
62       rho = 2.405 * x
63       return p[5]*((p[0]/(p[1] + abs(p[2]) /
         scipy.special.j0(rho))) - (p[3]/(p[4]+abs(p[2]) /
         scipy.special.j0(rho)))) * scipy.special.j0(rho)
64
65     if  (find(fitting,'mcleod2 ') != -1):
66       rho = 2.405 * x
67       return p[5] + 5.1*10**(-6)*((p[0]/(p[1] +
         abs(p[2])/scipy.special.j0(rho))) -
         (p[3]/(p[4]+abs(p[2]) / scipy.special.j0(rho)))) *
         scipy.special.j0(rho)
68
69     if (find(fitting,'mcleod-offset ') != -1):
70       rho = 2.405 * x
71       return p[6] + p[5]*((p[0]/(p[1]+abs(p[2]) /
         scipy.special.j0(rho))) - (p[3]/(p[4]+abs(p[2]) /
         scipy.special.j0(rho)))) * scipy.special.j0 (rho)
72
73     if (find(fitting,'bessel ') != -1):
74       rho = (pi/2)*x
75       return p[0]*scipy.special.j0(2.405*x) + p[1]
76
```

```
77      if (find(fitting,'cubic ') != -1):
78        return p[0] + [1]*x + p[2]*x**2 + p[3]*x**3
79
80      if (find(fitting,'bigpoly ') != -1):
81        polynomial = 0
82        for cf in range(polyorder):
83          polynomial = polynomial + p[cf]*(x**cf)
84        return polynomial
85
86      if (find(fitting,'exp ') != -1):
87        return p[0]*exp(-1*x*p[1])
88
89      if (find(fitting,'expsqrt ') != -1):
90        return p[0]*exp(-1*x*p[1]) * sqrt(x)
91
92      if (find(fitting,'linear ') != -1 or find (fitting,'nofit
        ') != -1):
93        return p[0]*x + p[1]
94
95    # Initial parameter guesses
96    if (find(fitting,'mcleod ') != -1):
97      p0 = [-100,10,10,10,10,10]
98
99    elif (find(fitting,'mcleod2 ') != -1):
100     p0 = [10,10,10,10,10,10]
101
102   elif (find(fitting,'mcleod-offset ') != -1):
103     p0 = [-100,10,10,10,10,10,20]
104
105   elif (find(fitting,'bessel ') != -1):
106     p0 = [100,5]
107
108   elif (find(fitting,'cubic ') != -1):
109     p0 = [10,10,10,10]
110
111   elif (find(fitting,'bigpoly ') != -1):
112     p0=[]
113     for cf in range(polyorder): p0.append(10)
114
115   elif (find(fitting,'exp ') != -1) :
116     p0 = [1,1]
117
118   elif (find(fitting,'expsqrt ') != -1):
119     p0=[1,1,2]
120
121   elif (find(fitting,'linear ') != -1 or
      find(fitting,'nofit') != -1):
122     p0 = [1,1]
123
124   else :
125     print "ERROR: " + fitting + " is not a valid fitting
        function."
126     return
127
```

```
128   plsq = optimize.leastsq(residuals, p0, args=(gain,
      pos),maxfev=5000)
129
130   print "\n"
131   print colour + " plot is a "+fitting+" function"
132   print "Parameters = "+str(plsq[0])
133
134   meanerror = 0.0
135   for i, g in enumerate(gain):
136     meanerror = meanerror + abs(peval(pos[i],plsq[0]) - g)
137   print "Mean error = "+str(meanerror / len(gain))
138
139   points=1000
140
141   trendlineX=linspace(minfit,maxfit,points)
142   trendlineY=peval(trendlineX,plsq[0])
143
144   print "Fitting = "+fitting
145
146   if find(fitting,'data') != -1:
147     errorbar(pos, gain, yerr=gain_stdev, xerr=None,
      fmt=ccode(colour)+'x', ecolor=None, capsize=3,
      barsabove=False)
148
149   if not find(fitting,'nofit') != -1:
150     plot(trendlineX,trendlineY,ccode(colour) +
      '-',linewidth=2.0)
151
152   return
153
154 def normalisepos(pos, tubedia, center):
155   normalised = []
156   for i in pos:
157     normalised.append( 2*(i-center)/tubedia )
158   return normalised
159
160 def ccode(colour):
161   colour = string.lower(colour)
162   if colour == 'blue': colour = 'b'
163   elif colour == 'green': colour = 'g'
164   elif colour == 'red': colour = 'r'
165   elif colour == 'cyan': colour = 'c'
166   elif colour == 'magenta': colour = 'm'
167   elif colour == 'yellow': colour = 'y'
168   elif colour == 'black': colour = 'k'
169   elif colour == 'white': colour = 'w'
170   else : colour = 'k'
171   return colour
172
173 # Gets mean plasma light in middle 10% of discharge
174 def meanplasma(filename, tubedia, tubecent):
175
176   pos=[]
177   plasma=[]
```

```
178
179     f = open(filename, 'r')
180     for line in f.read().split('\n'):
181       if len(line)==0 or not line[0][0].isdigit() :  continue
182       column = line.split(' ');
183       pos.append(float(column[0]))
184       plasma.append(float(column[2]))
185     f.close()
186
187     pos = normalisepos(pos, tubedia, tubecent)
188
189     plasmamean=0
190     count = 0
191     for x, p in zip(pos, plasma):
192       if  x > -0.1 and x < 0.1:
193         plasmamean = plasmamean + p
194         count = count + 1
195     plasmamean = plasmamean / count
196     print "plasma mean = "+str(plasmamean)
197
198     return plasmamean
199
200 #loads the profile in 'filename' and groups the measurements
201 #by position. Outputs the position, average gain, gain
202 #uncertanty and plasma light
203 def getprofile(filename, sigma):
204     f = open(filename, 'r')
205     pos=[]
206     gain=[]
207     gain_stdev=[]
208     pos_seg=[]
209     gain_seg=[]
210     previous = -1.0
211     for line in f.read().split('\n'):
212       colnum = 0
213       for column in line.split(' '):
214         if len(column)==0 or not column[0].isdigit() : break
215         n = float(column)
216         colnum = colnum + 1
217         if previous == -1.0: previous = n
218         if colnum == 1:
219           if n != previous:
220             pos.append(previous)
221             previous = n
222             gain_seg=remove_outliers(gain_seg, sigma)
223             gain.append(float(sum(gain_seg)) / len(gain_seg))
224             gain_stdev.append(stdev(gain_seg)/len(gain_seg)**0.5)
225             pos_seg=[]
226             gain_seg=[]
227           pos_seg.append(n)
228         if colnum == 2:
229           gain_seg.append(n)
230     pos.append(previous)
231     gain.append(float(sum(gain_seg)) / len(gain_seg))
```

```
232     gain_stdev.append(stdev(gain_seg))
233
234     f.close()
235
236     return pos,gain,gain_stdev
237
238 # The maximum and minimum permisable gains here may need to be
      changed
239 def remove_outliers(gain_seg, sigma):
240
241     maximum_gain = 500000 #7500.0
242     minimum_gain = -500000 #-2000.0
243
244     # Remove measurements if out of bounds
245     standard_deviation = stdev(gain_seg)
246     elements = len(gain_seg)
247     mean = float(sum(gain_seg)) / elements
248
249     good_elements=[]
250
251     for check in gain_seg:
252         if check > minimum_gain and check < maximum_gain and
          abs(check-mean) < (standard_deviation*sigma):
253             good_elements.append(check)
254
255     return good_elements
256
257 main()
```

Listing B.2: matchlines.py: Matches observed spectral lines up with a database of known lines and outputs a list of candidate lines with relative intensities for each observed line.

```
1  # This program takes in a file containing all the peaks of a
   spectrum
2  # and a file containing known spectral line data and matches
   them up
3  # generating a list of candidates for each line.
4
5  def main():
6
7      isotope, line_wav, line_rel_intensity,transition =
       getlines("spectrallines.txt")
8      obs_wav, obs_int = getpeaks("ug2peaks.txt")
9
10     for w in range(len(obs_wav)):
11         print "\n\nObserved line "+str(obs_wav[w])+" nm with
           intensity "+str(obs_int[w])
12         for l in range(len(line_wav)):
13             if obs_wav[w]>(line_wav[l]-0.33) and obs_wav[w]<
               (line_wav[l]+0.33):
14                 print "Found candidate "+ str(line_wav[l])+" nm, "+
                   str(line_rel_intensity[l]) + " rel intet, " +
                   isotope[l] + " transition " + str(transition[l])
```

```
15
16 def getpeaks(filename):
17   # Use matlab program to extract peaks to a text file
     'filename'
18
19   f = open(filename,"r")
20
21   wavelength=[]
22   intensity=[]
23   col_number=0
24   for line in f.read().split('\n'):
25     if line.strip() == "": break
26     wavelength.append(float(line[0:6]))
27     intensity.append(float(line[7:len(line)]))
28   f.close()
29   return wavelength, intensity
30
31 def getlines(filename):
32
33   f = open(filename,"r")
34
35   isotope=[]
36   wavelength=[]
37   rel_intensity=[]
38   transition=[]
39
40   for line in f.read().split('\n'):
41     col_number=0
42     for column in line.split('|'):
43       column = column.strip()
44       col_number=col_number+1
45       if col_number == 1:
46         if column == "" : break
47         isotope.append (column)
48       if col_number == 2:
49         wavelength.append (float(column))
50       if col_number == 3:
51         if column == "" : column = "0"
52         while not column.isdigit():
53           column=column [0:len(column)-1]
54         rel_intensity.append (int(column))
55       if col_number == 6:
56         transition.append(column)
57   f.close()
58
59   return isotope, wavelength, rel_intensity, transition
60
61 main()
```

Listing B.3: ledpower.py: Python program to calculate photodiode voltage due to LED

```
1 import DataInt
2 from math import *
```

```
3
4  led_output = 27.0 #27.0 #lumens
5  LED_distance = 1765.0 #mm
6  LED_temperature = 38.0 #C
7  room_temperature = 20.0 #C
8  darkcurrent = pow(20,-9) #A
9  pd_responsivity = 0.63 #0.66
10 lens_transmission = 0.9678 # %
11 led_beamangle = 140 #140 #degrees
12 lens_radius = 12.0 #mm
13
14 cie = DataInt.Interpolate("CIE-function.txt")
15 led_funct = DataInt.Interpolate("led1.nspectra")
16 led_angulardist = DataInt.Interpolate("batwing.txt")
17 led_tempResponse = DataInt.Interpolate("RED-LED-out-Temp.txt")
18 pd_tempResponse = DataInt.Interpolate("pd-res_temp.txt")
19 pd_sensitivity = DataInt.Interpolate("pd-curve_vishay.txt")
20
21 def angulardist_integral(x):
22   return led_angulardist.value(x*(180/pi))*sin(x)
23
24 pd_responsivity = pd_responsivity *
   pd_tempResponse.value(room_temperature)
25 theta = (180/pi) * atan(lens_radius/LED_distance)
26 total_solidangle = 2*pi*DataInt.simpsonInt(
   angulardist_integral, 0.0, 70.0*(pi/180), 1.0*(pi/180))
27 candela_total = led_angulardist.value(theta/2) * ((led_output
   * led_tempResponse.value(LED_temperature) *
   lens_transmission) /total_solidangle)
28 lumens_intercepted = candela_total * (pi*pow(lens_radius,2) /
   pow(LED_distance,2))
29
30 def cie_led(x):
31   return cie.value(x)*led_funct.value(x)
32
33 cie_led_integral = DataInt.simpsonInt(cie_led, 580, 680, 1)
34 peak_power = lumens_intercepted / (683.002 * cie_led_integral)
35
36 def led_pd(x):
37   return led_funct.value(x)*pd_sensitivity.value(x)
38
39 def led_pd_total(x):
40   if led_pd(x) > 0:
41     return 1
42   else:
43     return 0
44
45 effective_power = peak_power * (DataInt.simpsonInt(led_pd,
   300, 1200, 3) / DataInt.simpsonInt(led_pd_total,300,1200,3))
46 voltage = 100000 * ((effective_power * pd_responsivity) -
   darkcurrent)
47
48 print "Total solid angle="+str(total_solidangle)+ " sr"
49 print "Candela total="+str(candela_total)+" cd"
```

```
print "Lumens on photodiode="+str(lumens_intercepted)+" lm"
print "Peak power on photodiode="+str(peak_power)+" W"
print "Effective power="+str(effective_power)+" W"
print "Voltage = "+str(voltage*1000)+" mV"
```

Listing B.4: DataInt.py: A general utility program to integrate irregularly spaced data. Required by the program shown in listing B.3. While similar integration routines are available in scientific python, the integrator was implemented here for ease of modification.

```
import Numeric
from pylab import load #uses pylab's load function. Pylab must be installed.

class Interpolate:

  def __init__(self, datafile):
    # Constructor requires a data file from which to get the
    # data for interpolation
    # Data file should have two columns, the first being the
    # independent variable
    # and the next being the dependent valiable. Additional
    # columns will be ignored.

    # Load data in
    indata = load(datafile)

    # Sort the data down using the first column
    # (independent variable)
    newdata = Numeric.zeros(indata.shape,Numeric.Float)
    ags = (Numeric.argsort(indata,0))[:,0]
    elements = (ags.shape)[0]

    for i in range(elements):
      getidx = ags[i]
      newdata[i,0]=indata[getidx,0]
      newdata[i,1]=indata[getidx,1]

    # Save to instance property of this class
    self.data = newdata[:,:]


  def value(self, xlook):
    # Looks up the independent variable x and returns the
    # resulting dependent quantity
    # from the supplied data. If the exact value has not been
    # supplied then interpolate
    # from the nearest known values. It x is < smallest value
    # or > bigest value then return 0.

    x,y=self.data[:,0],self.data[:,1]
    elements = (x.shape)[0]
    if xlook < min(x) or xlook > max(x) :
      return 0
```

```
44
45      for i in range(elements):
46        if x[i] == xlook:
47          return y[i]
48        if x[i] > xlook: #interpolate
49          slope = (y[i] - y[i-1]) / (x[i] - x[i-1])
50          return y[i-1] + slope*(xlook-x[i-1])
51
52      return 0
53  # --- end of Interpolate class
54  # --- Function to compute integral using simpson rule
55  def simpsonInt(func, lo, hi, stepsize):
56    n=(hi-lo)/stepsize
57    dx = stepsize / 2.0 #Use half widths for Simpson rule
58    area=0.0
59    x_lo = lo
60    x_md = lo + dx
61    x_hi = lo + 2.0 * dx
62    i=0
63    for i in range(int(n)) :
64      left_side = func(x_lo)
65      middle = func(x_md)
66      right_side = func(x_hi)
67      area = area + dx*(left_side + 4.0 * middle +
        right_side)/3.0
68      x_lo = lo + 2.0 * i * dx;
69      x_md = x_lo + dx;
70      x_hi = x_lo + 2.0 * dx;
71    return area;
```

Listing B.5: gaintube-integrator.py: Essentially uses ray-tracing from many point sources to find the fraction of light incident on a photodiode a given distance away.

```
1   #Length of discharge in central part and ends of tube.
2   #Discharge assumed symetrical
3   def recievedpower(central_plasma=100.0, ends_plasma=50.0):
4
5     step=0.05 #mm
6
7     #properties of the tube
8     central_diameter=7.5
9     central_length=100 #mm
10    ends_diameter=10.0
11
12    total=0
13    i=0
14    # central tube
15    for x in arange(-1*(central_plasma/2), central_plasma/2,
      step):
16      for y in
        arange(-1*(central_diameter/2),central_diameter/2,step):
17        f = pointsource(x,y)
18        if (f>0): i=i+1
```

```
19          total=total+f
20      # near end
21      for x in
        arange(0.5*central_length,0.5*central_length+ends_plasma,step):
22          for y in arange(-1*(ends_diameter/2), ends_diameter / 2,
            step):
23              f = pointsource(x,y)
24              if (f>0): i=i+1
25              total=total+f
26      # far end
27      for x in arange(-0.5*central_length-ends_plasma,
        central_length/2, step):
28          for y in arange(-1*(ends_diameter/2),
            ends_diameter/2,step):
29              f = pointsource(x,y)
30              if (f>0): i=i+1
31              total=total+f
32
33      return total/i
```

Appendix C

Miscellaneous equations

C.1 Magnetic field due to a current loop

The total field strength at a radial position x and axial position y from a current loop of radius r carrying current I is the sum of B_r and B_g. $K(k)$ is the complete elliptic integral of the first kind and $E(k)$ is the complete elliptic integral of the second kind. These integrals are easily evaluated using Maple.

$$B_r = B_0 \left(\frac{\gamma}{\pi\sqrt{Q}} \right) E(k) \frac{1+\alpha^2+\beta^2}{Q-4\alpha} - K(k) \tag{C.1}$$

$$B_x = B_0 \left(\frac{1}{\pi\sqrt{Q}} \right) E(k) \frac{1-\alpha^2-\beta^2}{Q-4\alpha} - K(k) \tag{C.2}$$

Here:

$$\begin{aligned} \alpha &= \frac{r}{a} \\ \beta &= \frac{x}{a} \\ \gamma &= \frac{x}{r} \end{aligned}$$

$$B_0 = \frac{I\mu_0}{2\sin^{-1} k}$$

$$Q = |(1+\alpha)^2 + \beta^2|$$

$$k = \sqrt{\frac{4\alpha}{Q}}$$

Appendix D

Licencing

All source code contained in this thesis is free software and is available under the terms of the MIT license.

D.1 MIT license